Intense Magnetic Fields Generation in Laser Produced Plasma Using Inverse Faraday Effect

by

Fatema Tuz Johra Liza

A thesis submitted in partial fulfillment of the requirements for the degree of

Masters of Science

in

Photonics and Plasmas

Department of Electrical and Computer Engineering
University of Alberta

Abstract

Laser plasma interactions with high intensity laser pulses can produce extremely high magnetic fields in the MG range. In particular, the application of circularly polarized or orbital angular mode (OAM) laser beams can be used to generate such large fields using the Inverse Faraday Effect (IFE). Inverse Faraday Effect is the phenomenon where a magnetic field is induced in the dielectric medium due to the rotation of the electromagnetic fields. These induced high magnetic fields in the MG range can play an important role in the generation and guiding of electrons in laser plasma interaction process. Hot electron generation due to the interaction of intense laser pulses with underdense plasma can generates additional axial and azimuthal currents also leading to generation of strong magnetic fields.

Plasma interaction has been studied using Large Scale PIC (LSP) simulations to predict the scaling laws for the hot electron generation

and hence the expected magnetic field for circularly polarized light. Simulations have been carried out for different densities ($n_e \approx 0.0002$ n_c to $n_e \approx 0.02$ n_c) and intensities in the threshold relativistic intensity range of 10^{17} to 10^{19} Wcm^{-2} . Simulation results show that the induced magnetic fields vary with both electron density and laser intensity and the hot electron generation depends on laser intensity too. Multiple scaling laws proposed by different authors are compared with the simulation results. A Scaling law that takes the spiralling hot electron current into account is the one that appears to agree best with the simulation results.

In order to measure these expected intense fields Zeeman splitting of emission lines is investigated as a means to measure the induced axial magnetic fields. A Preliminary set of measurements have carried to verify the measurements of emission lines from the focusing into static gas targets at modest intensities of the order of 10^{17} Wcm-^{2}. CO_2 is used as the background gas and emission lines of CII 657.8nm and CII

658.3nm were measured for the linearly and circularly polarized laser beams. With the available laser power, 1GW, the Induced magnetic fields are fairly small and it was not possible to measure the splitting. However, scaling to higher irradiation powers should allow measurable magnetic fields to be observed.

Table of Contents

List of Tables

List of Figure

List of Abbreviations

List of commonly used abbreviations

CPA	Chirped-pulse Amplification
FE	Faraday Effect
IFE	Inverse Faraday Effect
MG	Mega Gauss
CCD	Charge-Coupled Device
ICCD	Intensified Charge Coupled Device
fs	femtosecond (10^{-15} of a second)
ps	picosecond (10^{-12} of a second)
GW	Giga-watt (10^{9} watt)
PW	Peta-watt (10^{15} watt)
TW	Tera-watt (10^{12} watt)
KeV	Kilo- electronvolt (10^{3} eV)
MeV	Mega-electronvolt (10^{6} eV)
FI	Fast Ignition
FWHM	Full Width at Half Maximum
ICF	Inertial Confinement Fusion
OAM	Orbital Angular Momentum

LG	Laguerre Gaussia
PIC	Particle in Cell
LSP	Large scale PIC
SNR	signal to noise ratio
MCP	micro channel plate
NA	Numerical Aperture

Chapter 1

Introduction

Lasers have numerous applications in today's world. People are using them in different fields like science, biomedical instruments, commercial industries, information technology, communication, entertainment, research and so on. From the time the laser has been invented by Maiman [1], tremendous improvements have been made. The peak power of laser pulse has grown from watts to Petawatts (10^{15} watt), pulse duration has shrunk from microseconds (10^{-6}sec) to femtoseconds (10^{-15}sec), and energy has grown from milijoules (10^{-3} J) to megajoules (10^{6} J). Intensities that can be achieved have increased from 10^{10} to 10^{22} w/cm^{2}. Since the invention of Chirped Pulse Amplification (CPA), high power laser pulse durations have come down from picoseconds to less than 5 femtoseconds. These high Intensity, ultrashort pulses are used for many new applications and have led to new fields of study. At present, some laboratories around the world are using this CPA technique to generate laser pulses with peak power of petawatts and duration of multi-femtoseconds.

Fig 1.1 shows the evolution of peak pulse intensities versus time and various new application areas at increasingly high intensity [2].

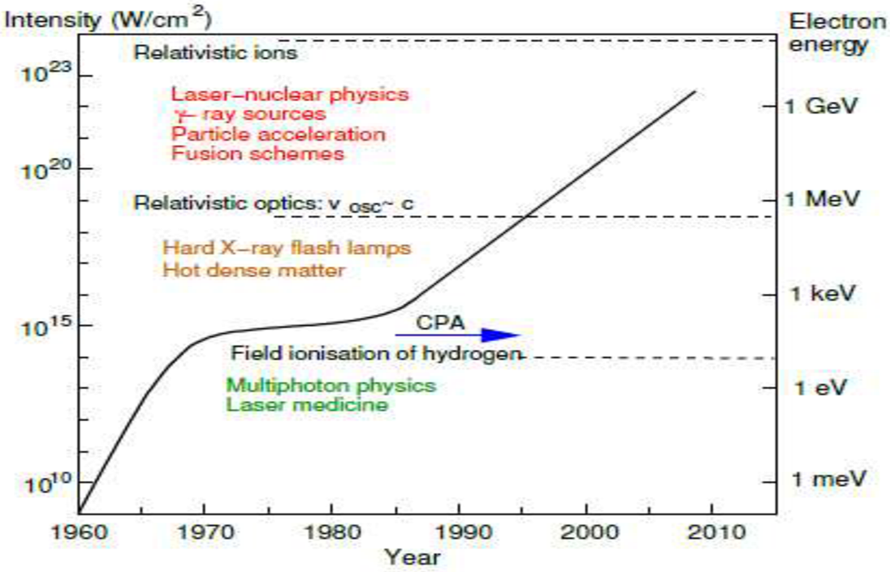

Fig 1.1: Progress in peak intensity since the invention of the laser in 1960 [2]

When these ultra-short laser pulses are focused onto solid or gaseous targets at threshold relativistic intensities (≥ 10^{18} W/cm^2), the laser field strength is sufficient to accelerate electrons to relativistic velocities every half cycle and creates relativistic plasmas. These laser-plasma interactions are of interest to researchers and scientists from many different fields of expertise because of various different applications such as fusion energy using the concept of fast ignition (FI) [3], laser wakefield acceleration (LWFA) [4], generation of coherent XUV radiation [5], self-induced large magnetic field generation [6][7] and many more. In the past several decades, such high intensity laser and plasma interactions have found applications in the physical sciences, astrophysics, quantum physics, engineering and so on.

Among these, self-induced magnetic field generation (in the MG range) is the main studied topic in this thesis. High intensity short laser pulses interacting with underdense plasma induces axial and solenoidal magnetic fields. Underdense and overdense plasmas are defined based on the critical plasma density is given by

$$n_c = \frac{\omega_0^2 m_e\ \epsilon_0}{e^2} \cong \frac{1.1\times10^{21}}{\lambda_{um}^2} \quad [cm^{-3}] \tag{1.1}$$

here, $\omega_0$is the laser angular frequency in vacuum, m_e is the electron mass, $\epsilon_0$is the permittivity of free space, e is the electron charge and λ_{um} is the laser wavelength in vacuum (units in um). If the plasma density is greater than critical density then the plasma is overdense. If the plasma density is less than critical density then the plasma is underdense.

1.1 Self-Induced Magnetic Field Generation

One of the important features of laser plasma interactions is magnetic field generation. Self-induced magnetic field in laser produced plasma is a topic of theoretical and experimental interests because of their application in the design of Inertial Confinement Fusion (ICF) targets.

Large magnetic fields (in the Megagauss range) can be produced by laser plasma interactions. Many theoretical studies have been carried out describing a variety of generation mechanisms [6]-[11].

1.1.1 $\nabla n \times \nabla T$ Toroidal Magnetic Field Generation Mechanism

One of the most studied mechanisms for inducing self-generated magnetic field is the $\nabla n \times \nabla T$ mechanism [7] where the energy for these spontaneous magnetic fields comes from the thermal energy of plasma. When a high irradiance laser pulse is focused on a solid target, it can produce dense, energetic plasma where electron temperature and density gradients are not parallel.

From Maxwell equation

$$\nabla \times E = -\frac{1}{c}\frac{\partial B}{\partial t} \tag{1.2}$$

Neglecting the inertia of the electrons, from the electron momentum equation:

$$0 = -\nabla P_e - e n_e E \tag{1.3}$$

where P_e is the pressure, n_e is the electron density, e is the charge of electron.

From the ideal gas equation

$$P_e = n_e k_B T_e \tag{1.4}$$

From (1.2), (1.3) and (1.4)

$$\frac{\partial B}{dt} = \frac{c k_B}{e n_e} \nabla T_e \times \nabla n_e \tag{1.5}$$

Where , $\nabla T_e \times \nabla n_e \neq 0$.

For a laser produced plasma in a right handed cylindrical (r, φ, z) coordinate system, ∇T is in the r direction (toward the axis) and ∇n is in the z direction (toward the target). So B is in the $-\varphi$ direction (azimuthal direction).

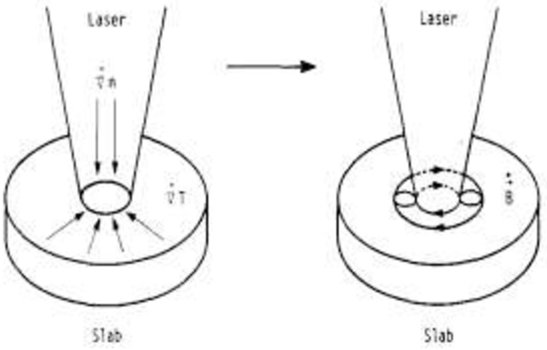

Fig 1.2: Typical geometry for Toroidal $\nabla n \times \nabla T$ magnetic fields near edge of laser spot. [12]

1.1.2 $\nabla n \times \nabla I$ Mechanism

Another mechanism for inducing self-generated magnetic field is by temporal variations in the Ponderomotive force (Ponderomotive force is a non-linear force that a charged particle experiences in an inhomogeneous oscillating electromagnetic field) [8][13]. Extremely intense self-generated magnetic fields are observed to form in overdense plasma in a PIC Simulation. Actually the gradient in laser intensity causes the electrons to be pushed away to the edge from the focal spot and this drift is eventually halted by charge separation and will create electron density depletion. From this acceleration a group of electrons will acquire a velocity and a net Ponderomotive current will be induced.

$$J=en_e v_p \sim n_e\ \nabla I \qquad (1.6)$$

here ∇I is the Laser Intensity gradient.

Then applying Ampere’s law, $\nabla^2 B \sim \nabla \times J \sim \nabla n_e\ \times \nabla I$ (1.7)

An azimuthal magnetic field will be induced by a radial intensity profile on a density gradient.

1.1.3 Faraday Effect (FE) and Inverse Faraday Effect (IFE)

1.1.3.1 Faraday Effect:

The Faraday Effect or Faraday rotation is a magneto-optical phenomenon, which was discovered by Michael Faraday [14]. When a plane-polarized light beam passes through a dielectric or a plasma medium in the direction of an external magnetic field, the plane of polarization rotates. The Faraday Effect takes place because left and right circularly polarized light propagates at slightly different speeds due to the difference in the index of refraction of the waves. Linearly polarized light can be written as the sum of left and right circularly polarized light. The angle of rotation of the beam is proportional to the magnetic field. For a plasma medium [15]:

$$\theta(\mathrm{deg}) = 3.02(\frac{\lambda}{um})^2\ \int_0^l (\frac{dz}{um}) \left(\frac{n_e}{10^{21} cm^{-3}}\right) (\frac{B}{MGauss})(1-\frac{n_e}{n_c})^{-1/2} \qquad (1.8)$$

where, $n_e$is the constant electron density, B is the magnetic field, l is the path length in the plasma, λ is the wavelength, n_c is the critical plasma density and z is the propagation direction.

The Faraday Effect has been used [16] to measure the magnetic field in laser plasma interactions. For that, one needs to know the electron density of the plasma.

1.1.3.2 Inverse Faraday Effect (IFE):

As the name suggests, the Inverse Faraday Effect is the opposite of the Faraday Effect. Inverse Faraday Effect is the phenomenon where a magnetic field is induced in the dielectric medium due to the rotation of the electromagnetic field. When a circularly polarized light beam propagates through a nonlinear medium, it will induce an axial magnetic field along the direction of propagation, due to the transfer of angular momentum from the wave to charge carriers in the medium.

My research is related to the Inverse Faraday Effect and using Zeeman splitting to measure that self-induced magnetic field in plasma medium.

1.2 Outline of the Thesis

Chapter 2 provides the detailed theory of laser plasma interactions, background theory of Inverse Faraday Effect and hot electron generations. Regarding hot electron generations, an overview of laser plasma absorption mechanisms is also given.

Chapter 3 is all about simulation studies of induced magnetic field due to Inverse Faraday Effect. Simulations have been carried out to understand the IFE mechanism and to predict a scaling law for the amount of Magnetic fields induced due the IFE.

Chapter 4 explores the Zeeman splitting technique to measure the induced magnetic field. The background theory of Zeeman splitting effect and an overview of the experimental setup are given. Preliminary experimental results are discussed.

Chapter 5 contains a discussion of results and the future work which can be done based on the current work.

Chapter 2

Physics of Laser Plasma Interactions and Self Induced Axial Magnetic Field due to Inverse Faraday Effect

2.1 Introduction

This chapter reviews some background physics related to the thesis topics. This include laser interaction with gas targets, including electromagnetic wave propagation in plasmas and different processes which occur in laser produced plasmas such as laser defocusing, laser absorption, filamentation, wave breaking and so on.

2.2 Femtosecond Laser

A femtosecond laser is a laser with less than 1 ps pulse duration. One of the most common gain media for short laser pulses is the Ti-sapphire crystal. The spectral emission of a Ti-sapphire crystal is very broad with a maximum at about 800nm. Ti-sapphire crystals can produce spontaneous mode locking without using a saturable absorber [17]. The dramatic increase in the power of the femtosecond laser pulses became possible with the invention of Chirped Pulse Amplification (CPA) techniques in the mid-1980's [18]. In a chirped pulse the frequency of the electromagnetic wave varies with time.

In the CPA technique, the output femtosecond laser pulse from the oscillator is first stretched in time (chirped in frequency), then amplified and finally recompressed, as shown in Fig 2.1.

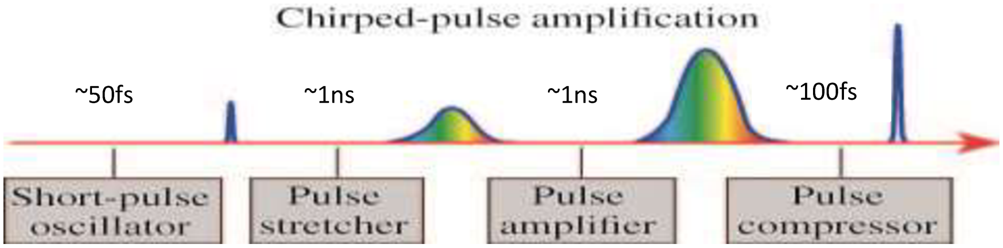

Fig 2.1: Principle of chirped pulse amplification

2.3 Electromagnetic wave propagation in Plasma

The linear dispersion relationship in uniform plasma is

$$\omega_0{}^2 = \omega_{pe}^2 + k^2c^2 \tag{2.1}$$

where k is the wave number, c is the speed of light in vacuum, ω_0 is the laser frequency and $\omega_{pe}$is the plasma frequency.

$$\omega_{pe} = (\frac{4\pi n_e e^2}{m_e})^{1/2} \tag{2.2}$$

here, $n_e$is the electron density, $m_e$is the mass of electron and e is the electron charge.

Consider a planar electromagnetic wave traveling in the z direction with electric field variation

$$\mathrm{E}\ (\mathrm{z},\ \mathrm{t}) = E_0 \exp[i(kz - \omega_0 t)] \tag{2.3}$$

Different absorption mechanisms occur in different plasma regimes and different intensity regimes. In under-dense plasma at lower intensities laser absorption is primarily due to inverse Bremsstrahlung. For overdense plasmas resonance absorption occurs at the critical surface. Absorbed laser energy is then transported to the solid target surface via thermal conduction. Some hot electrons are generated from the critical density surface and propagate further into the target, preheating the target before thermal conduction heating can penetrate into the target for femtosecond pulses.

If the ablating plasma is isothermal, the plasma density has an exponential profile given by:

$$n_e = n_0 \exp(-\frac{z}{L}) \tag{2.4}$$

where, $n_e$is the plasma density, n_0 is the solid density and L is the plasma scale length given by L=$C_s t$, where t is the time and C_s is the ion acoustic velocity [19]

$$C_s = \sqrt{k(Z_i T_e + T_i)/m_i} \tag{2.5}$$

where Z_i is the ionization state, k is the Boltzmann's constant, T_e is the electron temperature, T_i is the ion temperature and m_i is the mass of ion.

Beyond Critical density n_c, the wave vector k given by eqn 2.1 becomes imaginary and the wave attenuates exponentially within a skin depth. Skin depth is given by:

$$\delta = \frac{c}{\sqrt{\omega_{pe}^2 + \omega_0^2}} \tag{2.6}$$

Before reaching the critical surface, the laser beam must propagate through the region of under dense plasma. The laser beam can transfer some of it's energy to the plasma. It might also undergo self-focusing, filamentation or other phenomenon if the underdense plasma is long enough.

2.3.1 Inverse Bremsstrahlung (Collisional Absorption)

Inverse Bremsstrahlung is one of the most important mechanisms in laser plasma coupling. It occurs for low intensities ($I<10^{17}$ w/cm^2) in underdense plasma. The radiation emitted by an electron due to the collision with another particle is called Bremsstrahlung emission. As the name suggests, Inverse Bremsstrahlung is the opposite. Inverse Bremsstrahlung is the process where an electron absorbs a photon while colliding with an ion or electron and it causes electron acceleration in the field of ion.

If we consider infinite and homogenous underdense plasma and ions that are infinitely heavy and no static magnetic or electric fields, the electron acceleration $\frac{dv}{dt}$ due to the electric field E can be calculated by:

$$\frac{dv}{dt} = -\frac{eE}{m_e} - \nu_{ei}\mathrm{v} \qquad (2.7)$$

where, e is the electron charge, m_e is the electron mass, v is the electron velocity and ν_{ei} is the electron –ion collision frequency is given by:

$$\nu_{ei} = \frac{4}{3}\frac{(2\pi)^{1/2}Z_i^2e^4n_i ln\Lambda}{(k_BT_e)^{3/2}m_e^{1/2}} \approx 2.907 \times 10^{-6}\ \frac{Z_i^2n_i ln\Lambda}{(T_e(eV))^{3/2}}[\mathrm{s}^{-1}] \qquad (2.8)$$

where, n_i is the ion density and $ln\Lambda$ is the Coulomb logarithm for electron-ion collisions. The Coulomb logarithm is defined by

$$\Lambda = \frac{\lambda_D}{l_{min}} \qquad (2.9)$$

where λ_D is the Debye length and l_{min} is the de Broglie wavelength or classical distance of 90^0 deflection (whichever is larger) [15].

The Debye length is given by

$$\lambda_D = \left(\frac{\varepsilon_0 k_BT_e}{n_ee^2}\right)^{1/2} \qquad (2.10)$$

And the de Broglie wavelength is given by

$$l_{deBroglie} = \sqrt{\frac{h^2}{2\pi m_ek_BT_e}} \qquad (2.11)$$

where h is Planck’s constant. And the classical distance of 90^0 deflection is given by

$$l_{90^0} = \frac{Ze^2}{k_B T_e} \tag{2.12}$$

here, n_e is the electron density, T_e is the electron temperature, Z is the ion charge, and k_B is the Boltzman constant.

When the electron oscillates in laser electric field and absorbs energy from the laser field, the spatial damping rate of the laser energy by inverse bremsstrahlung is given by [15]

$$k_{ib} = \frac{\nu_{ei}(n_c)}{c}\left(\frac{n_e}{n_c}\right)^2 (1 - \frac{n_e}{n_c})^{-1/2} \tag{2.13}$$

where ν_{ei} is the collision frequency at the critical density.

It is clear that inverse bremsstrahlung absorption increases near the critical density, $n_e/n_c \approx 1$. As the laser pulse propagates in a plasma, the intensity changes. The change in laser intensity, I, through the plasma in the propagation direction z, can be given by:

$$\frac{dI}{dz} = -k_{ib} I \tag{2.14}$$

For a finite length of plasma L, the absorption A_{abs} can be written as:

$$A_{abs} = \frac{I_{in} - I_{out}}{I_{in}} = 1 - \exp(-\int_0^L k_{ib} dz) \tag{2.15}$$

where I_{in} is the incoming laser intensity, I_{out} is the outgoing laser intensity. For weak absorption, $k_{ib}L \ll 1$, then $A_{abs} = k_{ib}L$, on the other hand, for strong absorption, $A_{abs} \longrightarrow 1$.

For an exponential density profile given by

$$n_e = n_c \exp(\frac{z}{L_n}) \tag{2.16}$$

where L_n is the density gradient length.

The absorption is given by [19]:

$$A_{abs} = 1 - \exp\{ -\frac{8}{3}\frac{\nu_{ei}(n_c)L}{c} \}$$

At higher laser intensities (> 10^{16} Wcm−2) with higher electron temperature (2 keV), since the collision frequency, ν_{ei} proportional to $T_e{}^{-3/2}$, inverse bremsstrahlung becomes less efficient and other absorption processes become relatively more important [20].

2.3.2 Collisionless Absorption

For intensities above 10^{15} Wcm^{-2} or so, the temperature rises sufficiently fast that collisions become ineffective during the laser plasma interactions. A temperature of 1keV corresponds to a thermal velocity $v_{te} \approx 0.063$ c. So collisional absorption starts to turn off for irradiances $I\lambda^2 \geq 10^{15} W cm^{-2} um^2$ and Inverse Bremsstrahlung absorption becomes weak [21] [22]. Collisionless absorption processes start to occur in this regime. Energy transfer from the laser pulse to hot electrons involves a number of collisionless mechanisms near the critical density such as resonance absorption, vacuum heating and J× B heating. Resonance absorption was studied extensively in the 1970s and 1980’s to obtain a better understanding about the origin of fast electrons generated in nanosecond laser-plasma interactions [23][24].

2.3.2.1 Resonance absorption

Resonance absorption occurs when p-polarized laser is obliquely incident at an angle of incidence θ into a density profile with plasma expanding normally to the target surface [25]. P- Polarized light incident on a steeply rising plasma density at a different angle than zero from normal incidence has a singularity in the magnitude of the oscillating electric field at the critical density in the plasma. In this case, an electric field component is parallel with the density gradient $(E \cdot \nabla n \neq 0)$. This electric field tunnels through the plasma and drives an electron plasma wave resonantly at the critical density. The damping of this electron wave is possible by collision or collisionless processes. That is why resonance absorption can occur even when the electron-ion collision frequency is very small. For s-polarized light, the electric field is always perpendicular to the density gradient$(E \cdot \nabla n = 0)$. There will be no such electron plasma wave.

For a linear density gradient, the absorbed power for resonance absorption is given by [19] [26]

$$P_{abs} \cong \frac{\pi}{2} \varepsilon_0 c L^2 E_d^2 \tag{2.18}$$

where ε_0 is the free space permittivity, L is the plasma scale length, c is the speed of light and E_d is component of laser electric field which oscillates the electrons through the density gradients and can expressed by:

$$E_d = \frac{E_0}{\sqrt{\frac{2\pi\omega L}{c}}}\,\alpha(\eta) \tag{2.19}$$

here, $E_0$is the peak amplitude in vacuum of the incident laser electric field,

$$\alpha(\eta) \cong 2.3\eta\,\exp(-2\eta^3/3) \tag{2.20}$$

$$\text{And }\ \eta \cong (\frac{\omega L}{c})^{1/3} sin\theta \tag{2.21}$$

The angle of incidence for peak resonance absorption is given by:

$$\theta_{max} \simeq\ \sin^{-1}\left[0.8\left(\frac{c}{\omega L}\right)^{\frac{1}{3}}\right] \tag{2.22}$$

Resonance absorption can be higher than inverse bremsstrahlung absorption in cases such as high plasma temperature due to high laser intensity, longer laser wavelength, lower values of n_c, and short plasma scale length. Using P polarized light and the optimum incident angle, one can get up to 50% resonance absorption.

2.3.2.2 Vacuum Heating (Brunel Type Absorption)

In the case of a very steep electron density gradient**,** Resonance absorption stops working. The peak oscillation amplitude of the electron plasma wave near critical density is larger than the plasma scale length($\frac{v_{os}}{\omega_{pe}} \gg L$). Let's consider a case, where the plasma scale length approaches zero, e.g. a sharp plasma – vacuum interface. In this case, electrons at solid density will be directly exposed to the laser field and in half of the laser cycle, thermal electrons may be dragged out into the vacuum well beyond the thermal Debye sheath, $\lambda_D = v_{te}/\omega_{pe.}$ When the fields reverses direction, electrons will be accelerated back into the plasma. As the plasma is overdense, the electric field will penetrate only to a skin depth ~c/ω_{pe} shorter than the electron range. As the electrons travel back into overdense plasma, they will escape the field and their energy will be absorbed due to collisions.

This important mechanism was first proposed by Brunnel [27]. Using a model based on the 'capacitor approximation' where the magnetic field of the wave is ignored, i.e. the $\boldsymbol{v} \times \boldsymbol{B}$ term is neglected and assumes that the electric field E$_0$ has some component E$_d$ normal to the target surface which drags electrons back and forth across their equilibrium positions (Fig 2.2).

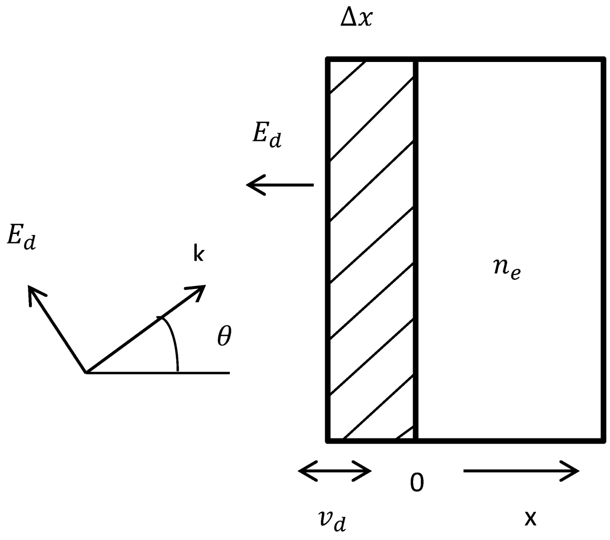

Fig 2.2: Capacitor model of the Brunel heating mechanism

With incident angle θ, the driving electric field is given by:

$$E_d = 2E_0\ sin\theta \tag{2.23}$$

Assuming the oscillating electrons are all lost to the solid, this model predicts the laser absorption rate:

$$\eta_a \equiv \frac{P_a}{P_L} = \frac{4}{\pi} a_0 \frac{(\sin\theta)^3}{\cos\theta} \tag{2.24}$$

where, $a_0 = v_{os}/c$

From (2.22), it is clear that we will get more absorption at large angles of incidence and higher laser intensities, $I\lambda^2 \propto a_0^2$. The expression predicts over 100% absorption, if the parameters are large enough. If we take into account the reduced driver field amplitude due to imperfect reflectivity, driving electric field becomes

$$E_d = \left[1 + (1 - \eta_a)^{\frac{1}{2}}\right] E_L sin\theta \tag{2.25}$$

Now, the return velocity of the electrons may become relativistic at intensities over 10^{18} Wcm^{-2}. Taking the both corrections on account, the fractional absorption rate expression becomes:

$$\eta_B = \frac{1}{\pi a_0} f\ [\,(1 + \ f^2 a_0^2 sin^2\theta)^{\frac{1}{2}} - 1]\,\frac{\sin\theta}{\cos\theta} \tag{2.26}$$

where f= 1+(1-η_a)$^{1/2}$ is the field amplification factor.

However the capacitor model does not take into account the influence from the magnetic field. The additional magnetic field can deflect the fast electrons and inhibit them from returning to the high density plasma resulting in a much smaller absorption coefficient than that predicted by the capacitor model for relativistic intensities. This problem was pointed out by Gibbon and Bell [28], who simulated the vacuum heating using a $1\frac{1}{2}$D particle-in-cell code. The simulation showed that the vacuum heating dominates over resonant absorption for plasma scale length L/λ < 0.1, and is most efficient when v_{os}/c≈3.1$(\mathrm{L}\times\ \lambda)^2$. In addition, the simulation also suggested that the absorption tends to peak at 45^0. Finally, it was found that at an incident angle of 45^0, and for L× λ=0 .04, the absorption rate saturates at around 10%-15% for high laser intensity ($I\lambda^2 > 10^{17}\ Wcm^{-2}\,um^2$).

2.3.2.3 $\boldsymbol{J}\times\boldsymbol{B}$ Heating

This mechanism is similar to the vacuum heating except the main driving term is the high frequency $\boldsymbol{v}\times\boldsymbol{B}$ component of the Lorentz force, which oscillates at twice the laser frequency.

Let us consider a linearly polarized wave $E = E_0(x)\sin\omega t$

It will generate a longitudinal ponderomotive force term:

$$f_x = -\frac{m}{4}\,\frac{\partial v_{os}^2(x)}{\partial x}(1-\cos 2\omega t) \tag{2.27}$$

Here, 1st term is the usual DC ponderomotive force. This force will try to push the electron density profile inwards. The 2nd term which is a high frequency component leads to heating in the same manner as the electric field does for the resonant absorption. This $J \times B$ heating works for any polarization except circular polarization. This is more efficient at normal incidence and becomes significant at relativistic quiver velocities. The absorption rate for $J \times B$ heating is around 10-15% for $I\lambda^2 = 10^{18}\,Wcm^{-2}\,um^2$ and drops significantly at intensities below this irradiance.

2.4 Self- focusing

Self-focusing occurs in the relativistic regime due to nonlinear change of refractive index of the plasma in the region where a high intensity electromagnetic wave has a transverse intensity distribution. Self-focusing appears both due to the relativistic increase in the electron mass and due to the production of a lower central plasma density distribution by the ponderomotive force. The first mechanism is instantaneous while the second requires a finite time for the electrons to be displaced.

The resultant refractive index of the plasma medium increases on axis with the peak of the electric field intensity, and acts as a focusing lens for the laser beam. The peak intensity of the self-focused beam keeps increasing as the wave travels through the plasma until defocusing effects interrupt this process.

The critical power for relativistic self-focusing is [29]:

$$P_{cr} = \frac{m_e c^5 \omega^2}{e^2 \omega_{pe}^2} \backsimeq 17\left(\frac{\omega}{\omega_{pe}}\right)^2 \text{ GW} \tag{2.28}$$

For P>P_{cr} , relativistic self-focusing overcomes diffraction spreading and in the cubic nonlinearity approximation, the beam will be focused into a field singularity over a finite distance given by:

$$Z_{s-f} = Z_R\left(\frac{P}{P_{cr}} - 1\right)^{-1/2} \tag{2.29}$$

where, $Z_R = \frac{\pi \omega_0^2}{\lambda}$, is the Rayleigh length. If P≫ P_{cr}, the laser beam can split into several filaments, each of them will undergo for self-focusing.

2.5 Ionization Defocussing and Maximum Intensity in Underdense Plasma

Because tunnel ionization leads to ionization at high intensities and the refractive index of a plasma decreases with electron density when a high intensity laser pulse propagates into an underdense plasma the Gaussian beam profile produces a defocusing refractive index profile when propagating through an underdense plasma. This may decrease the peak intensity that can be achieved when focusing a beam into an underdense gas target. This phenomenon has been studied by Fill et al. [30] and Fedosejevs et al. [31]. The model developed by Fill [30] will be outlined here and an analysis will be carried out in chapter 4 for the experimental cases considered in this thesis. At high intensities tunnel ionization [31] occurs when the electric field of the focused laser beam is strong enough to overcome the Coulomb barrier of confining a given electron in an atom or ion. A simple expression is found for the intensity threshold required for tunnel ionization to occur depending on the ionization potential, U_q, and resultant charge, q, of the ion given by:

$$I_{th} = 4 \times 10^9 q^{-2} U_q^4 \quad [\mathrm{Wcm}^{-2}] \qquad (2.30)$$

In order to derive an analytic expression for the minimum spot size due to ionization defocusing, power law fits are applied to the actual ionization potentials for given atoms in the form of:

$$U(q) = U_0 q^a \qquad (2.31)$$

The required values for U_0 and α are obtained by least square fits to the L-shell ionization potentials of atoms of interest. These values have been obtained using least square fits to the ionization potentials and plotted in Fig 2.3.

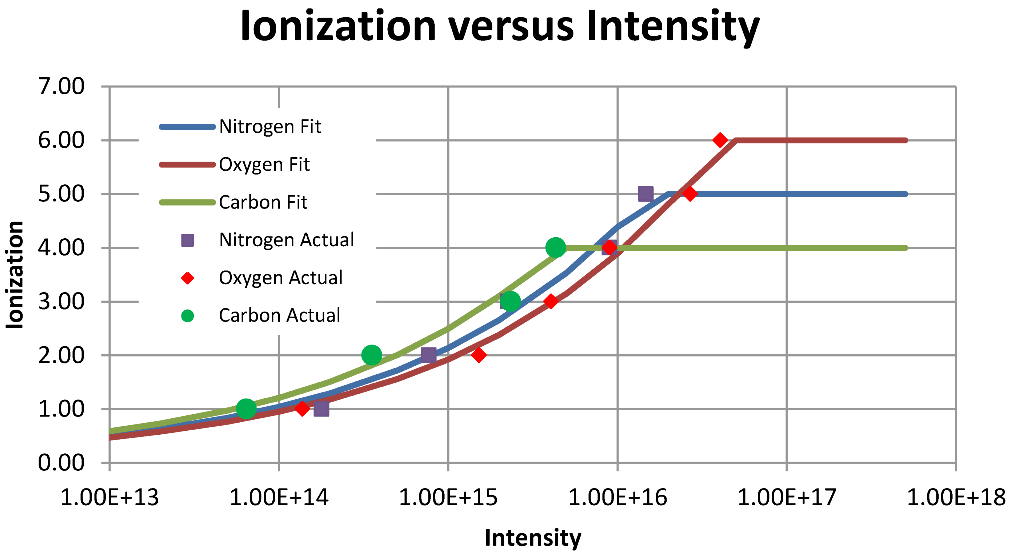

Fig 2.3: Plots of the fitted analytic ionization expressions and the actual threshold ionization intensities. The ionization potentials are taken from the NIST database and the values of (U_0, a) for the atoms are (12.22, 1.30), (13.14, 1.32) and (10.85, 1.30) for N, O and C respectively.

Using this dependence of ionization on intensity the beam propagation and focusing can be calculated by using Gaussian beam propagation in a graded index medium with a parabolic refractive index given by the resultant ionization on axis. By taking the lowest order parabolic fit to this graded refractive index profile on axis, Fill et al. obtain expressions for the minimum spot size, $r_{i,min}$ (defined as the 1/e intensity radius), as a function of input beam half angle, C, gas density, n, critical electron density, n_c, and power, P, given by:

$$r_{i,min} = [q_0\,(n/n_c)/C^2]^{2a-1}\,(P/\pi)^{1/2} \qquad (2.32)$$

The peak intensity obtained is then given by:

$$I_{i,max} = P/(\pi\ r_{i,min}^{2}) \qquad (2.33)$$

However, this peak intensity spot must always be larger than or equal to the diffraction limited minimum beam radius for the incident gaussian beam which is given by:

$$r_{D,min} = l/\ 2\pi C \qquad (2.34)$$

As a simple estimate one can take a simple convolution of the ionization limited spot size and diffraction limited spot size given by:

$$r_{0,min} = (\ r_{i,min}^{2} + r_{D,min}^{2}\ )^{1/2} \qquad (2.35)$$

The maximum intensity can be calculated using

$$I_{0,max} = P/(\pi\ r_{0,min}^{2}) \qquad (2.36)$$

These results can then be used to calculate what intensity can be achieved when focussing into a given gas density and what ionization states would be expected.

2.6 Hot Electron Generation

All the absorption mechanisms that are mentioned in section 2.3 will superheat some fraction of electrons in the plasma medium. Lets denote this hot electron temperature as T_h that will be much greater than the bulk plasma temperature T_e. These hot electrons play an important role for short pulse laser plasma interactions. These hot electrons are another source for self-induced magnetic field generation. In order to calculate the hot electron temperature, there are multiple models proposed by different groups to scale the temperature with laser Intensity for interaction with solid targets.

The scaling law proposed by Beg [32] from their experimental measurements is given by:

$$T_h\,(\mathrm{KeV}) = 215(I_{18}\,\lambda_{um}^2)^{1/3} \tag{2.37}$$

where I_{18} is the laser intensity in units of 10^{18} W/cm^2 and λ_{um} is the vacuum wavelength in units of μm. This law applies up to intensities of 10^{19} W/cm^2.

The scaling law proposed by Wilks [33] based on ponderomotive heating is as given by:

$$T_h\,(\mathrm{KeV}) = (\gamma_t - 1)m_e c^2 \tag{2.38}$$

where $\gamma_t = (1 + \frac{I_{18}\lambda_{um}{}^{2}}{1.37})^{1/2}$.

Recently Haines et al. [34] published a fully relativistic analytical model based on energy and momentum conservation laws for laser interaction with over-dense plasma. Their scaling is much lower than Wilks ponderomotive scaling, and is given by:

$$T_h\ (\text{KeV}) = [(1 + 1.21\sqrt{I_{18}\lambda_{um}^{2}})^{1/2} - 1)]m_e c^2 \qquad (2.39)$$

If we assume $\lambda = 1um$ and given, $m_e c^2 = 511keV$, we get following plot, Fig 2.3, of T_h versus laser intensity from the above scaling laws:

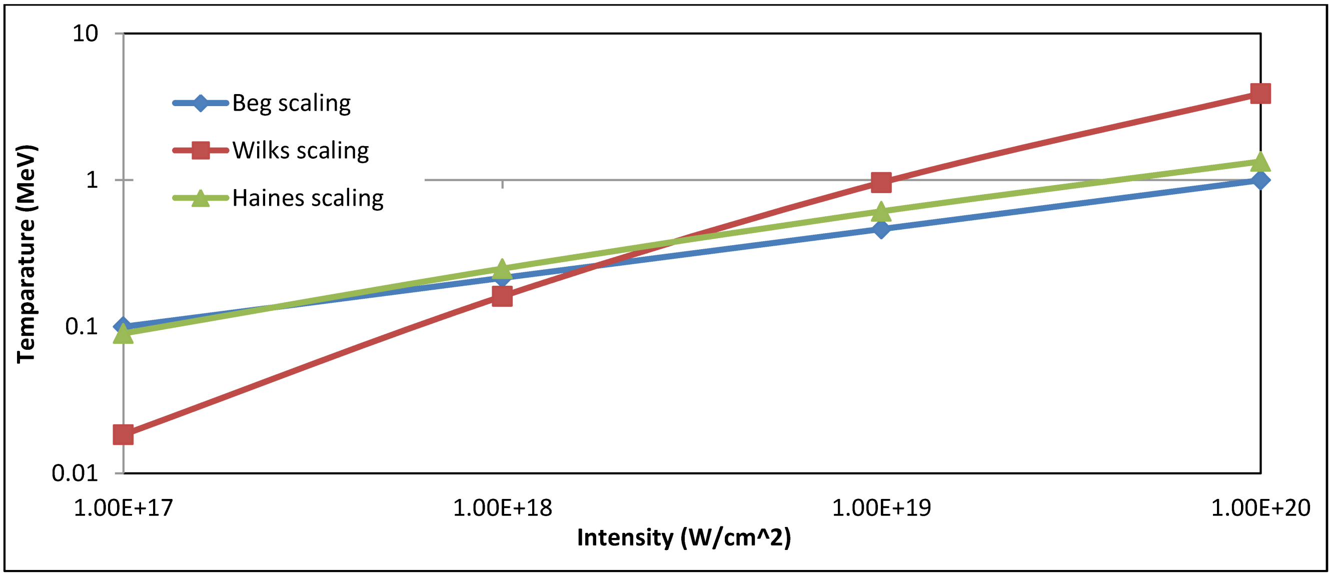

Fig 2.4: Hot electron temperature vs laser intensity using Beg's, Wilk's and Haines scaling using eqn 2.23, 2.24 and 2.25 respectively for 1 µm wavelength in log scale

2.7 Magnetic Field Generation for Inverse Faraday Effect

As mentioned before (1.1.3.2), the Inverse Faraday Effect is a phenomenon where if a circularly polarized light propagates through a nonlinear medium, it will induce an axial magnetic field along the direction of propagation, due to the transfer of angular momentum from the light to charge carriers in the medium.

When the laser pulse is circularly polarized then electrons describe a circular motion. The net effect of this is a circular current on the edge of plasma, which generates the magnetic field.

Following reference [15], the motion of the electrons due to the laser electric field is given by:

$$\frac{\partial v}{\partial t} = -\frac{e}{m_e} E \tag{2.40}$$

where v is the electron velocity, E is the electric field of the laser. Let us consider ions are immobile and the laser is circularly polarized in the x and y directions and it is propagating in the z direction:

$$E = E_0 \left(\frac{\hat{x} + i\hat{y}}{\sqrt{2}}\right) \exp[-i(wt - kz)] \tag{2.41}$$

where $\hat{x}$ and $\hat{y}$ are the unit vectors in the x and y directions respectively.

From (2.40) and (2.41):

$$v = v_0 \left(\frac{-i\hat{x}+\hat{y}}{\sqrt{2}}\right) \exp[-i(wt - kz)] \qquad (2.42)$$

$$where, \qquad v_0 = \frac{eE_0}{m_e w} \qquad (2.43)$$

Electrons need to satisfy the continuity equation:

$$\frac{\partial n_e}{\partial t} = -\nabla.(n_e v) \qquad (2.44)$$

For a uniform background electron density, n_0 we can write:

$$n_e = n_0 + n_1 \qquad (2.45)$$

Here n_0 does not depend on time, $n_1 \approx \exp(-iwt)$ and we assume $n_0 \gg n_1$. Carrying out a 1st order analysis we can assume, $\nabla \cdot v = 0$. Then continuity eqn 2.35 yields :

$$iwn_1 = v \cdot (\nabla n_0) \qquad (2.46)$$

The electric current can be found from eqn 2.42 and 2.46:

$$J = -e < n_1 v > = < \frac{ie}{w}(v.\nabla n_0)v > \; = \frac{e^3 E_0^2}{2m_e w^3} \nabla n_0 \times \hat{z} \qquad (2.47)$$

here the wave number vector, k of the electromagnetic field is parallel to $\hat{z}$. From this equation, it is clear that the electric current, **J** has a contribution from the density gradient in the x-y plane and it points in the toroidal direction. This current will produce an axial magnetic field in the z direction.

According to Maxwell equation:

$$\nabla \times B = \frac{4\pi}{c} J \qquad (2.48)$$

From 2.47 and 2.48, one can get:

$$B = B_c \left(\frac{w_{pe}^2}{2w^2}\right)\left(\frac{eE_0}{m_e wc}\right)^2 \qquad (2.49)$$

where $B_c = \frac{m_e wc}{e} = \frac{1.07 \times 10^8}{\lambda(um)} G$ is the Compton Magnetic fields.

The laser intensity is related to the electric field by:

$$I_0 = c\,\frac{E_0^2}{8\pi} \qquad (2.50)$$

where I_0 is the laser peak intensity (in W/cm^2). Then we can write the eqn (2.49):

$$B_z = 6.0 \times 10^4 \left(\frac{n_e}{n_c}\right)(\lambda_{um} I_{14}) \quad [\mathrm{G}] \qquad (2.51)$$

where n_c is the critical electron density, I_{14} is the laser intensity in units of 10^{14} W/cm^2 and λ_{um} is the vacuum wavelength in units of *um.*

Using ponderomotive forces [35] Lehner suggested that induced magnetic field is not linear with the laser intensities, but square root of laser intensity I_0. He developed the expression for axial magnetic field for non-relativistic domain as given by:

$$B_z = B_c \left(\frac{w_{pe}}{w}\right)\left(\frac{eE_0}{m_e w c}\right) \approx 6.5 \times 10^5 \left(\frac{n_e}{n_c}\right)^{\frac{1}{2}} (I_{14})^{\frac{1}{2}} \quad [\mathrm{G}] \qquad (2.52)$$

The above equation works up to intensities 10^{14} W/cm^2. However at higher intensities hot electron generation from nonlinear laser-plasma interactions lead to additional magnetic field generation mechanism.

In an early publication, Sheng [6] has shown how the Inverse Faraday Effect would occur in an under dense plasma in a self-consistent way for relativistic intensities. He considered 2 sources of magnetic field: 1. The Circular motion of single electron in the wave which is equivalent to a magnetic dipole and 2. The Inhomogeneity of both the electron density and the Intensity of laser beam.

Considering a cylindrical geometry and no external magnetic field, the approximate expression for the induced axial magnetic field in a uniform plasma is:

$$\mathrm{B_{uni}} = \frac{1}{2}\, B_c\, \left(\frac{w_p^2}{w^2}\right) \left(\frac{3|a^2|}{2\gamma^2} - \frac{1}{2}\ln\gamma^2\right) \qquad (2.53)$$

In this result, the normalized field amplitude factor of the laser field is a= $0.84\sqrt{I_{18}\,\lambda_{um}^2}$ and $\gamma = \sqrt{}(1 + |a^2|)$, is the average transverse Lorentz factor. Considering laser frequency, $w = 1.79 \times 10^{15} s^{-1}$, $wavelength\ \lambda = 1.054\ \mu m$, and plasma density $n_e = 3.5 \times 10^{19} cm^{-3}$. A plot of the Induced Magnetic field (B_{uni}) versus Intensity is shown in fig 2.4 :

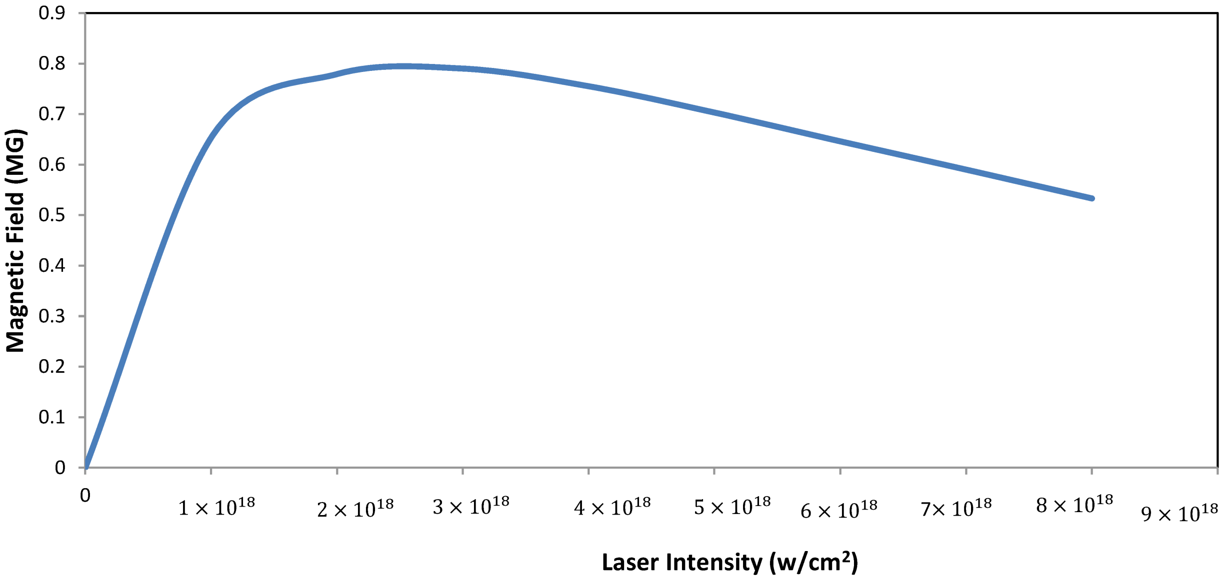

Fig 2.5: magnetic field versus intensity in uniform plasma (eqn 2.53)

Now, considering inhomogeneity of both the electron density and the Intensity of laser beam, the approximate expression for the induced magnetic field in uniform plasma is given by [6]:

$$B = \frac{1}{2} B_c \left(\frac{w_p^2}{w^2}\right) \left(1 + \frac{L_a^2}{L_a^2 + L_n^2}\right) \times \exp\left[-\left(\frac{r^2}{L_a^2} + \frac{r^2}{L_n^2}\right)\right] \qquad (2.54)$$

where L_a and L_n describe the inhomogeneity scale lengths of the laser and plasma profiles.

Horovitz [36] considered the laser absorption fraction for linear and circular polarization and also proposed a technique to measure the induced axial magnetic field. He measured the angle of Faraday rotation (eqn1.8) and from that he calculated the induced magnetic field for the Inverse Faraday Effect in kG range for intensity range of 9 $\times 10^{13}$ W/cm^2 to 2.4 $\times 10^{14}$ W/cm^2. Assuming a linear density profile, he obtained 16kG using an intensity of 6.4 $\times 10^{12}$ W/cm^2.

Axial Magnetic field generation due to Inverse Faraday rotation has been studied recently for high intensities. Najmudin [37] has been shown that the strength of magnetic field induced using higher intensity is much larger than expected from cold plasma. This can be explained by examining 3D Particle-in-Cell simulation. The Simulation shows the higher magnetic field generates due to the hot electrons that spiral around the axis of the channel created by laser. An expression for the induced axial magnetic field, taking into account the hot electrons can be given by:

$$B_{\mathrm{hot}} = \pi a B_C \frac{w_p^2}{w_0^2} \frac{n_h}{n_e} \tag{2.55}$$

Considering a hot electron fraction of $\frac{n_h}{n_e} = 0.2$ and density of $3.5 \times 10^{19}\ cm^{-3}$ a magnetic field of B_{hot}=5.34 MG is predicted at an intensity of $1 \times 10^{19}\ Wcm^{-2}$.

A further study of magnetic field generation at relativistic and ultrarelativistic intensities has been reported by Naseri et al. [38] where the effects of density cavitation and density channel wall gradients also contributed to the magnetic field generation. They have investigated the regime of parameters that corresponding to a relativistic self-focusing and laser pulse channelling. They have shown their result of 3D PIC simulations for 3 different cases: 1. a single channel self-focusing without full evacuation of electrons, 2. a ring like mode propagation of laser light and 3. a fully evacuated laser plasma channel. For single channel self-focusing without full evacuation of electrons, using an initial laser intensity of $1\times 10^{20} W/cm^{-2}$, and the background plasma density of $0.36 n_c$, they obtained a maximum induced magnetic field of 35MG. For a significantly higher intensity of $1\times 10^{22} W/cm^{-2}$, with the same density, they obtained a maximum induced magnetic field of 40MG. Then, for a fully evacuated laser plasma channel, with an initial intensity $1.7\times 10^{20} W/cm^{-2}$ and for an initial plasma density of $0.02 n_c$, they got significantly lower magnetic fields of around 2MG, as the effective electron density is much smaller. Our current study is focused on lower intensities where such density channelling is not expected to be a large factor.

2.7.1 Angular momentum consideration

It is well established that during the laser plasma interaction, angular momentum of the absorbed photons is transferred to the electrons of plasma. Angular momentum has a spin part associated with polarization [39] and an orbital part associated with spatial distribution of the propagating Electric and Magnetic fields [40].

Allen [40] Orbital Angular Momentum (OAM) of a photon beam using Laguerre Gaussian (LG) modes. Laguerre Gaussian (LG) Laser beams have a well-defined OAM equal to $l\hbar$, per photon, with l is the azimuthal mode index. He derived an expression for the axial component of total Angular momentum density per unit power,

$$M_z = \frac{l}{wc}|I|^2 + \frac{\sigma_z r}{2wc}\frac{\partial |I|^2}{\partial r} \tag{2.56}$$

where, $\sigma_z = \pm 1$ for left handed and right handed circularly polarized light and $\sigma_z = 0$ for linearly polarized light.

This equation is only valid for the paraxial approximation. For linearly polarized light ($\sigma_z = 0$), total angular momentum per second is:

$$L = \frac{P}{w} l \tag{2.57}$$

Haines [41] proposed another approach to calculate angular momentum. The local density of angular momentum is related to spin density as diamagnetic velocity is related to the density of magnetic moments. The mean axial component of angular momentum for circularly polarized light is given by:

$$M_z = \frac{\sigma_z}{wc}\frac{r}{2}\frac{\partial I}{\partial r} \tag{2.58}$$

During the laser – plasma interactions, angular momentum of the absorbed photons is transferred to the electrons, so electrons experience a torque. This will induced a very large azimuthal current and the axial magnetic field generated can be estimated as [12]:

$$B_z = -\frac{2}{wcLer_0^2}\int \frac{\alpha_{ab} I_0}{n_e} dt \tag{2.59}$$

where, α_{ab} is the absorption co-efficient which is the fraction of the laser intensity absorbed per unit length, L is the interaction length, and

r_0 is the beam radius. It is assumed that B_z is uniform. So, here, the induced magnetic field is associated with a scaling law n_e^{-1}.

Haines only considered the spin angular momentum as total angular momentum. Mendonca [12] has considered both Spin and OAM. The axial angular momentum due to the photon density is given by:

$$M_z = \frac{l}{wc} I + \frac{\sigma_z r}{2wc} \left(\frac{\partial I}{\partial r}\right) \tag{2.60}$$

From angular momentum conservation equation:

$$r E_{\emptyset} \sim -\frac{1}{e n_e} \frac{d M_z}{dt} \tag{2.61}$$

Using (2.50) and (2.51), one can get:

$$E_{\emptyset} = -\frac{1}{e n_e} \frac{l}{rwc} \frac{\partial I}{\partial t} - \frac{1}{e n_e} \frac{\sigma_z}{2wc} \frac{\partial^2 I}{\partial r \partial t} \tag{2.62}$$

From Faradays law:

$$\frac{1}{\mathrm{r}} \frac{\partial}{\partial r} r E_{\emptyset} = -\frac{\partial B}{\partial t} \tag{2.63}$$

Combining (2.62) and (2.63), we get:

$$\frac{\partial B_z}{\partial t} = \frac{1}{r}\frac{1}{en_e}\frac{\partial}{\partial r}\frac{\partial}{\partial t\partial}\left(\frac{lI}{wc} + \frac{\sigma_z r}{2wc}\frac{\partial I}{\partial r}\right) \tag{2.64}$$

Taking the Integral over time on both sides, the axial residual component of magnetic field after the pulse passes is given by:

$$\mathrm{B_z} = -\frac{f_{abs}}{ren_e wc}\left\{ l\,\frac{\partial I}{\partial r} + \frac{\sigma_z}{2}\,\frac{\partial}{\partial r}\left(r\,\frac{\partial I}{\partial r}\right)\right\} \tag{2.65}$$

where f_{abs} is the absorption co-efficient of the laser intensity over a certain axial distance L and can be expressed in terms of inverse bremsstrahlung as $f_{abs} = 1 - \exp(-k_{ib}L)$,where k_{ib} is the damping rate of the laser energy by inverse Bremsstrahlung.

Here, $I(t) - I(0) = -\,f_{abs}I$.

The intensity profile of the Laguerre Gaussian modes:

$$\mathrm{I(r)} = I_0\,\frac{(-1)^{2p}\,P!}{(l+P)!}\,\left(\frac{r}{r_0}\right)^{2l}\exp\left(-\,\frac{r^2}{r_0^2}\right)\left[L_p^l\left(\frac{r^2}{r_0^2}\right)\right]^2 \tag{2.66}$$

Let assume $l = 0, p = 0$, so $L_p^l = 1$. From (2.65),

$$I(r) = I_0\exp\left(-\frac{r^2}{r_0^2}\right) \tag{2.67}$$

Putting derivative on both sides w.r.t radius, we get:

$$\frac{\partial I}{\partial r} = I_0 \exp(-\frac{r^2}{r_0^2})\ (-\frac{2r}{r_0^2}) \tag{2.68}$$

Doing the 2nd derivative on both sides again w.r.t. r, we get

$$\frac{\partial^2 I}{\partial^2 r} = I_0 \exp(-\frac{r^2}{r_0^2})\ \ [\left(-\frac{2r}{r_0^2}+\frac{4r^2}{r^4}\right) \tag{2.69}$$

Using equation (2.68) and (2.69) and put those values to (2.65), we get:

$$B_z = -\frac{f_{abs}}{en_e wc}\,\frac{2\sigma_z}{r_0^2} I_0 \left(1-\frac{r^2}{r_0^2}\right)\exp(-\frac{r^2}{r_0^2}) \tag{2.70}$$

2.7.2 Inverse Faraday Effect (IFE) with Linearly Polarized Laser Light

The Inverse Faraday Effect has typically been associated with a circularly polarized beam. But from equation 2.65, it can be seen that for linearly polarized beam $\sigma_z = 0$, the axial magnetic field can exist due to the orbital angular momentum density involving higher order terms in the laser Intensity.

Normally, Photon beams have planar wave fronts with uniform phase. But helical wave fronts may exist, when wave vectors spiral around the beam axis, constituting the existence of OAM modes. LG modes can be used to represent helical wave fronts and each OAM LG mode is associated with well-defined state of beam OAM. Here, the intensity profile of the LG modes in the focal plane is given by [42]:

$$\mathrm{I(r)} = I_0 \frac{(-1)^{2p}\, P!}{(l+P)!} \left(\frac{r}{r_0}\right)^{2l} \exp\left(-\frac{r^2}{r_0^2}\right) \left[L_p^l\left(\frac{r^2}{r_0^2}\right)\right]^2 cos^2(l\emptyset) \qquad (2.71)$$

here, I_0 is the maximum axial intensity of the laser beam, r_0 is the beam radius, p is the radial mode number, $L_p^l\left(\frac{r^2}{r_0^2}\right)$ is the associated Laguerre polynomials and $\emptyset$ is the azimuthal angle. It can be seen that angular momentum density increases for varying l. The angular momentum for $l = 1$ and $p = 0$ can be expressed [44] :

$$M_z = \frac{I_0}{wc}\left(\frac{r}{r_0}\right)^2 \left\{1 + \sigma_z\left(1 - \left(\frac{r}{r_0}\right)^2\right)\right\} \exp\left(-\left(\frac{r}{r_0}\right)^2\right) cos^2(\emptyset) \qquad (2.72)$$

From this equation, it’s clear that Inverse Faraday Effect can even take place for linearly polarized laser beam. Mendonca has observed that the strength of the magnetic field decreases with increasing azimuthal angles and strength of the magnetic field is highest at $\emptyset = 0$.

Fig 2.6 shows the intensity distribution for linearly polarized LG mode and spatial magnetic field profiles for z=0 and $\sigma_z = 0$.

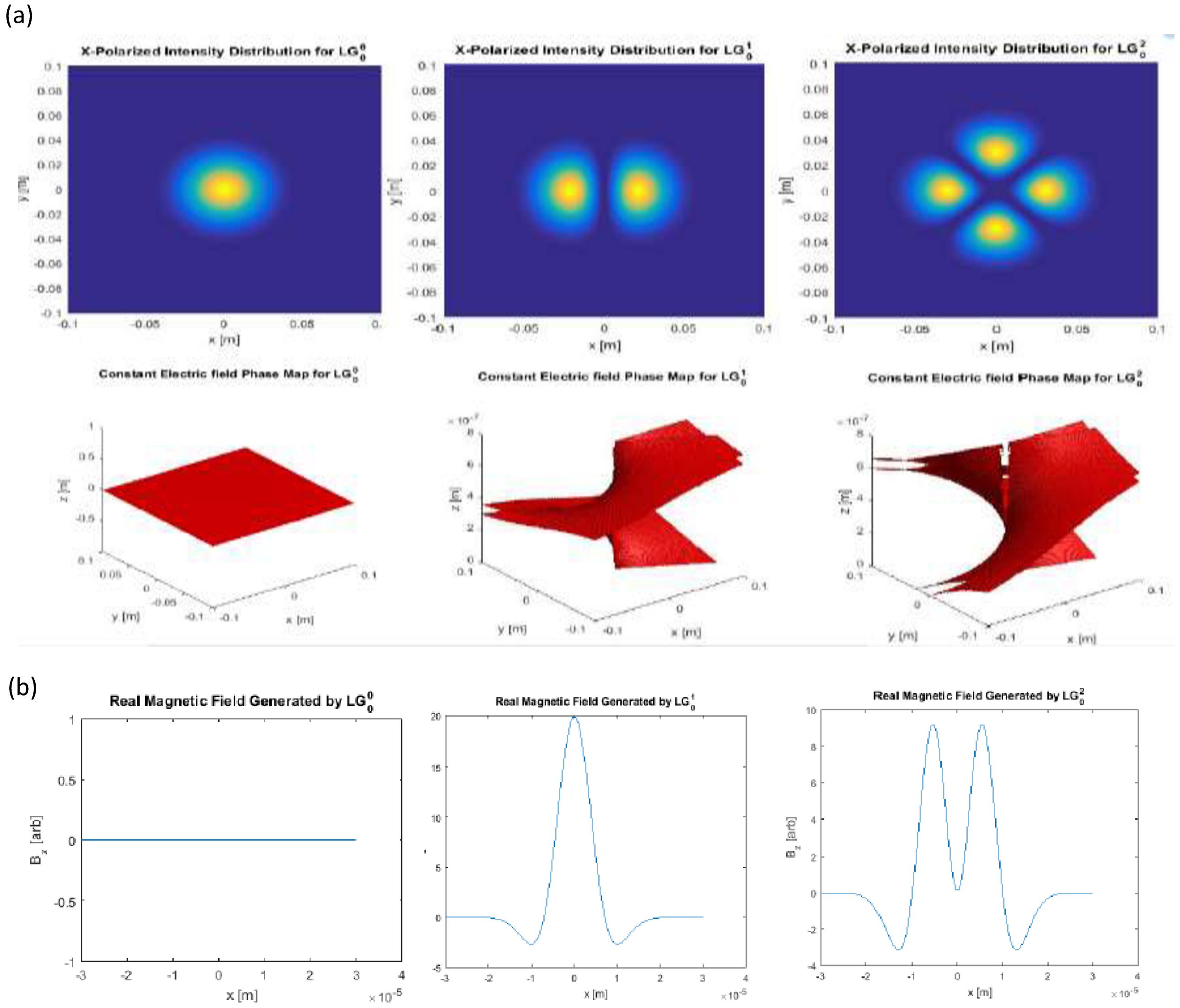

Fig 2.6: (a) Intensity distribution for linearly polarized LG modes L=0, 1, 2 and corresponding phase wave fronts in red (b) spatial magnetic field profiles in the beam cross section for z=0 and $\sigma_z = 0$.

Chapter 3

Simulation work: Magnetic Field Generation using the Inverse Faraday Effect

3.1 Introduction

Computer Simulation is a powerful method to investigate new ideas and get many details on the exact behaviour in the physical sciences. It helps to design and predict new experiments also. Using computer simulation, one can construct a numerical model of the system or theory which one wants to investigate and allows one to study the behaviour from some initial situation of interest in accordance with the laws of physics.

In this chapter Particle in Cell (PIC) code simulation is used to observe the Magnetic field generation due to the Inverse Faraday Effect. The simulation domain is divided into different sections: one section for launching either linearly or circularly polarized laser light, a second section for allowing the interaction of the laser and plasma and a final section to allow the laser beam to exit.

3.2 Introduction of PIC (Particle in Cell) Simulation:

Particle methods simulate a plasma system by following a large number of particle trajectories [43][44]. For the simulation, one may consider each particle as representing many particles due to the limitations of computer as most advanced computer cannot simulate the motions of more than a few billion particles.

Particle models for plasmas can follow a number of approaches like in one, two or three dimension, electrostatic, magnetostatic, or electromagnetic models and so on.

PIC codes investigate the trajectories of many particles interacting self-consistently via electromagnetic fields. It describes fields in terms of particle sources.

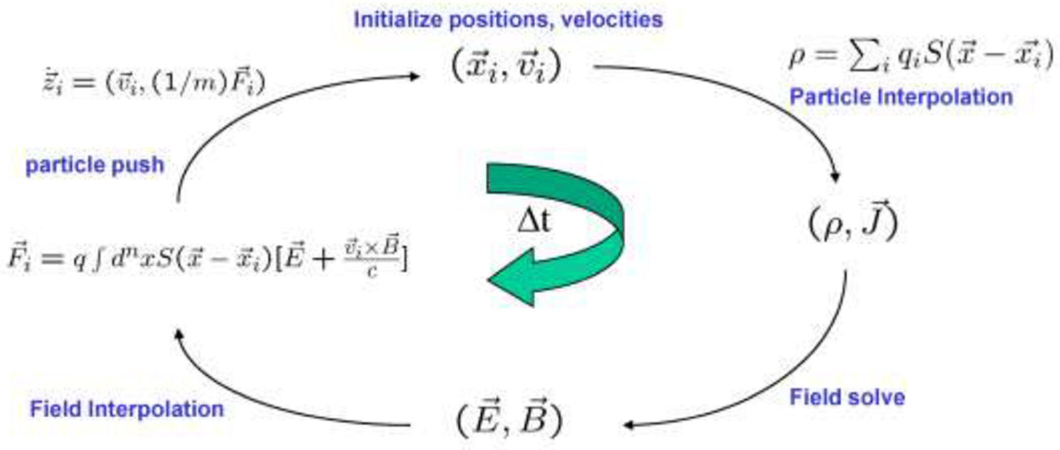

Fig 3.1: PIC computational cycle

As shown in fig 3.1, the PIC algorithm consists of four phases [43]:

1. Calculate Charge and Current Densities: From the positions, and velocities of the particles, assign charge, velocity, and current density to the grid points. This gives the total charge and current density.

2. Field Solve Phase: Using the charge and current density from phase 1, solve Maxwell's equations on the mesh to determine the electric (E) and magnetic fields (B).
3. Field Interpolation Phase: For each particle, use the values of electric and magnetic field at the grid points to interpolate the force on that particle at the particle's actual position.
4. Particle Push Phase: Update the position of each particle under the influence of the force.

One important consideration for particle models is particle collisions. In many phenomena, collisional effects are very weak. This is called collisionless plasma. Collisionless Plasmas require $\frac{\nu}{\omega_p} \approx \frac{1}{n\lambda_D^3} \ll 1$ (3-D)

Where ν is the electron collision frequency, $\omega_p = (\frac{4\pi n e^2}{m_e})^{1/2}$ is the plasma frequency. In the present cases considered the plasma is very hot and thus the collision frequency is very low. Therefore collisions are ignored for simulations presented here.

3.3 Introduction to LSP (Large Scale PIC) Simulation:

LSP is a 3-D electromagnetic particle in Cell (PIC) code for large scale plasma simulations [45]. It can also be used for 1-D or 2-D geometries. The code is designed to operate on serial or parallel platforms. All coordinate systems can be used: Cartesian, Cylindrical and Spherical. On parallel processors, domain decomposition with message passing is used to divide the load among the processors. The standard message passing interface (MPI) is used for inter process communication. LSP code is written in C using an object oriented style. The code calculates the interaction between charged particles (ions and electrons) and external and self-generated electric and magnetic fields. The code started with SBIR funding in 1995. Commercial use of LSP started from 2002. The LSP code runs on both: Windows and LINUX. The graphical pre-processor GLSP allows LSP input files to be generated graphically. LSP also has a graphical post processor P4 for viewing results. P4 is written in IDL and needs an IDL runtime license.

3.4 Simulation Set-up

First we launch linearly and circularly polarized light to check that the laser is defined correctly the way it should be. In this case we use the same parameters for both cases with equal electric field amplitudes in the y and z directions except with different phase shifts. It's a 3D PIC calculation with Cartesian grid size (x,y,z)=(100,50,50) in microns.

Table 3.1: Parameter used for launching linear and circularly polarized laser pulses

Wavelength	800nm
Spot size (FWHM)	2 μm (centered at y=25 μm, z=25 μm)
Pulse width (FWHM)	120fs
Propagation direction	X
Polarization direction (circular)	y-z
Grid Size (in x direction)	100 micron
Peak Electric field amplitude (E_y, E_z)	1.45×10^{7} kV/cm
Peak Intensity	$5.59\times 10^{17}\, W/cm^{2}$

For Linear polarization, there was no phase shift between E_y and E_Z components as expected as shown in Fig 3.2 which shows a horizontal lineout of the part of E_y and E_z fields at the same position of the laser beam at same time step.

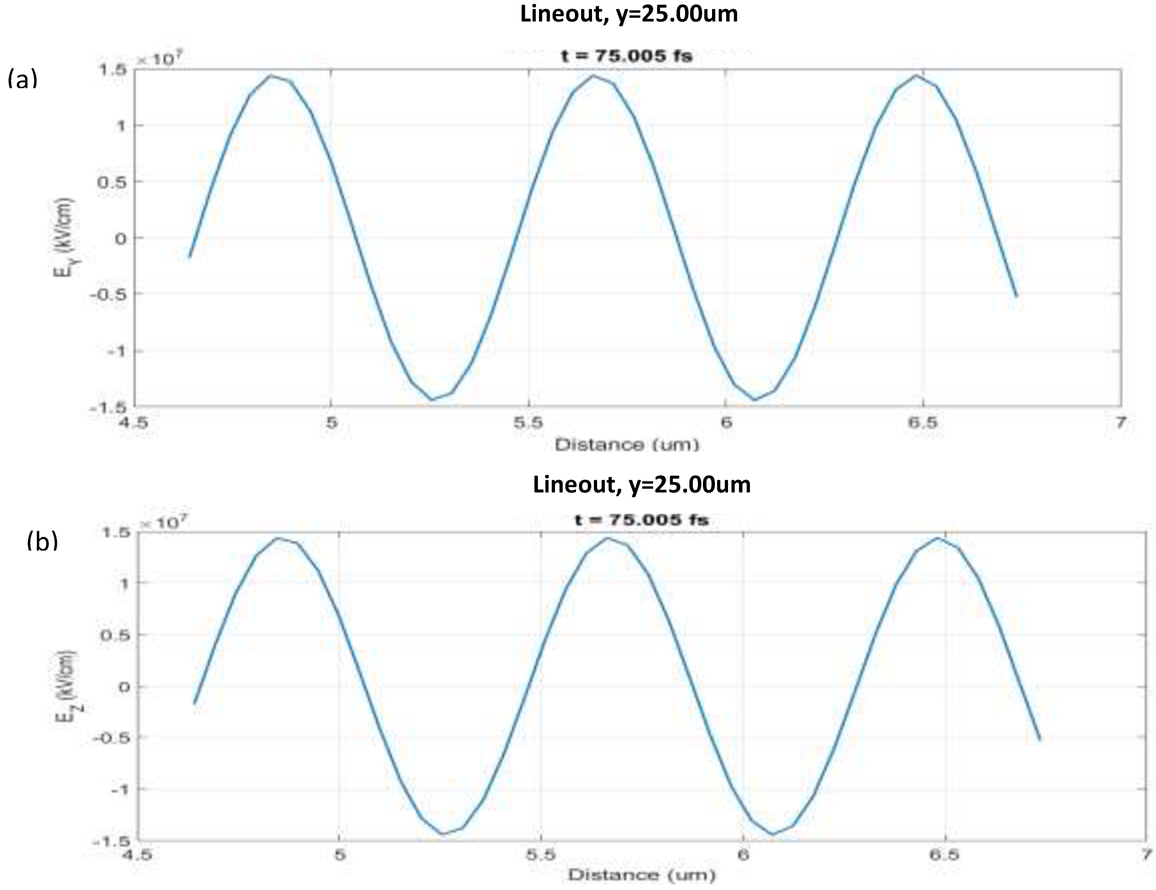

Fig 3.2: a line out drawn horizontally from x=4.5 μm to x=7 and at y=25 μm and z=25 μm showing 0 phase difference in between the Ey (a) and Ez (b) components of electric field for linearly polarized light at same time step, t=75fs with Intensity I=$5.59 \times 10^{17}\ Wcm^{-2}$

For right circular polarization, there was +90 phase shift between E_y and E_Z components as expected shown in Fig 3.3.

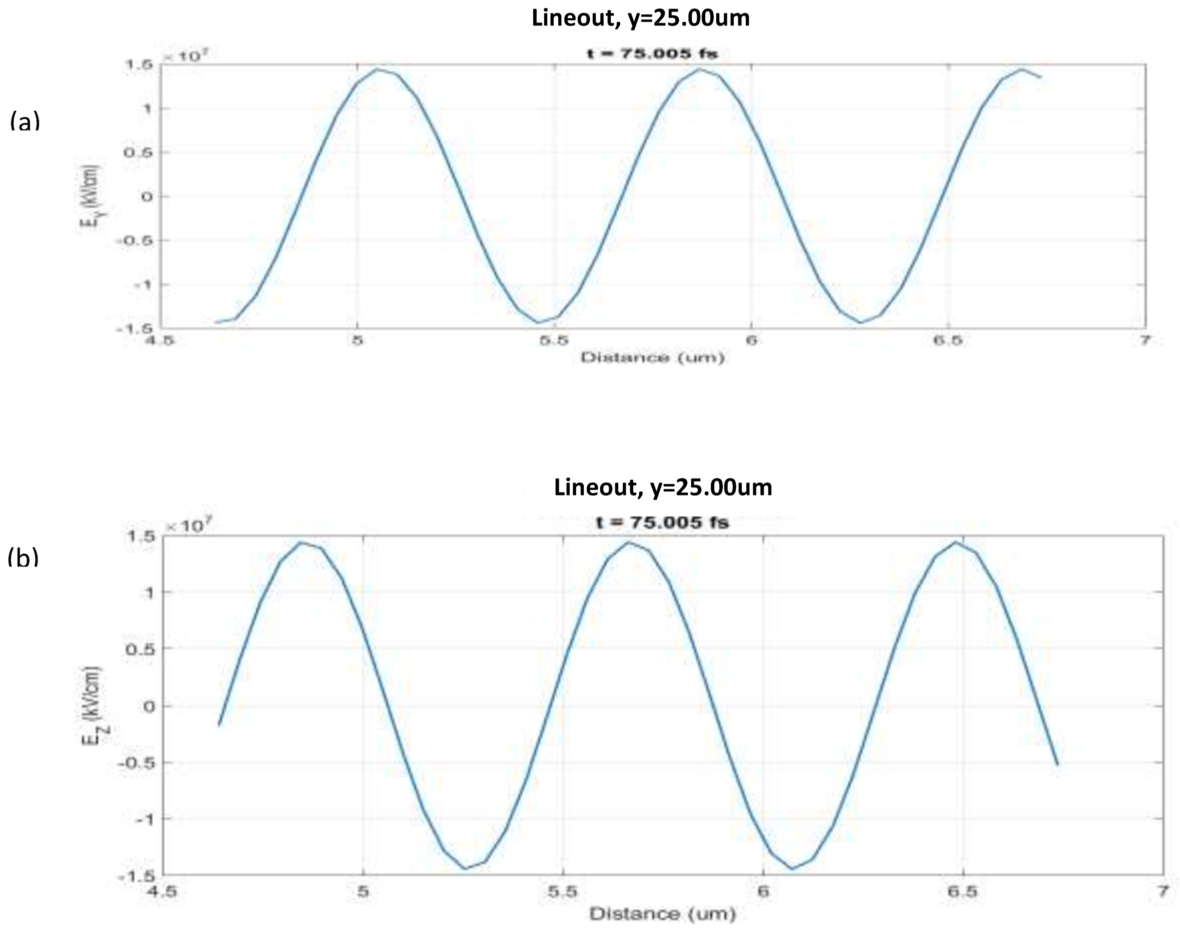

Fig 3.3: a line out drawn horizontally from x=4.5 μm to x=7 μm and at y=25 μm and z=25 μm at the same time showing +90 phase difference in between the Ey (a) and Ez (b) components of electric field for right circularly polarized light at same time step, t=75fs with Intensity I=$5.59 \times 10^{17}\ Wcm^{-2}$.

For left circular polarization, there was -90 phase shift between E_y and E_Z components as expected shown in Fig 3.4

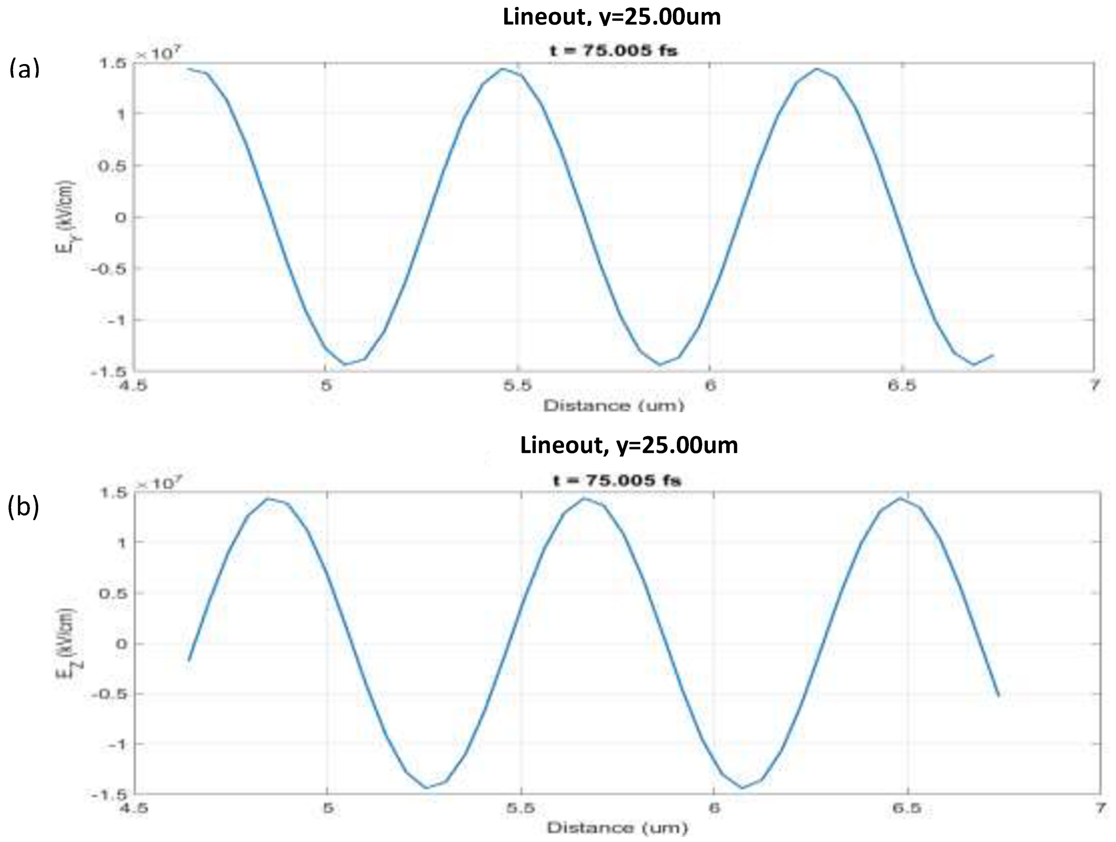

Fig 3.4: a line out drawn horizontally from x=4.5 μm to x=7 μm and at y=2 μm and z=25 μm at the same time showing -90 phase difference in between the Ey (a) and Ez (b) components of electric field for left circularly polarized light at a given time, t=75fs with Intensity I=$5.59 \times 10^{17}\ Wcm^{-2}$

3.4.1 Axial Magnetic Field Variation with Laser Intensity

Because of the Inverse Faraday Effect, a circularly polarized laser pulse passing through a non-linear medium induces an axial magnetic field by transferring angular momentum from the wave to electrons in the plasma. This induced magnetic field varies with the laser intensity. Part of the axial magnetic field is generated by the hot electrons produced by the laser plasma interactions. In addition, when a very intense laser pulse channels through plasma, then the plasma is no longer uniform.

The laser pulse expels the cold electron out of the way and induces a density gradient in the channel that can act as another source of axial magnetic field.

To study the scaling of magnetic fields with the Laser intensity, simulations have been carried out with various laser intensities. Electron temperature scaling has been monitored too. The parameters used in the simulations are given in table 3.2

Table 3.2: Parameters used for different simulation runs for various laser intensities with 50micron slab

Wavelength	1 micron
Spot size (FWHM)	10 micron (centered at y=25 µm, z=25 µm)
Pulse width (FWHM)	120 fs
Electron density	$3.5 \times 10^{19}\ cm^{-3}$
Propagation direction	X
Polarization direction (linear)	Y
Plasma slab size	50 micron (from x=20 µm to x=70 µm)
Number of Particles per cell	100
Cell size (x,y,z)	$0.05\ \mu m, 2\ \mu m,$ 2 µm
Total grid size (X×Y×Z)	100 µm × 50 µm ×50 µm
Time step	1 fs

Fig 3.5(a) shows simulation setup with the plasma slab starting from 20 µm to 70 µm with the electron density 3.5 $\times 10^{19}\ cm^{-3}$ at time, t=25 fs

and Fig 3.5(b) shows the y-component of the electric field (E_y) of the linearly polarized laser beam. Here the intensity, I=$3.15 \times 10^{19}\, Wcm^{-2}$

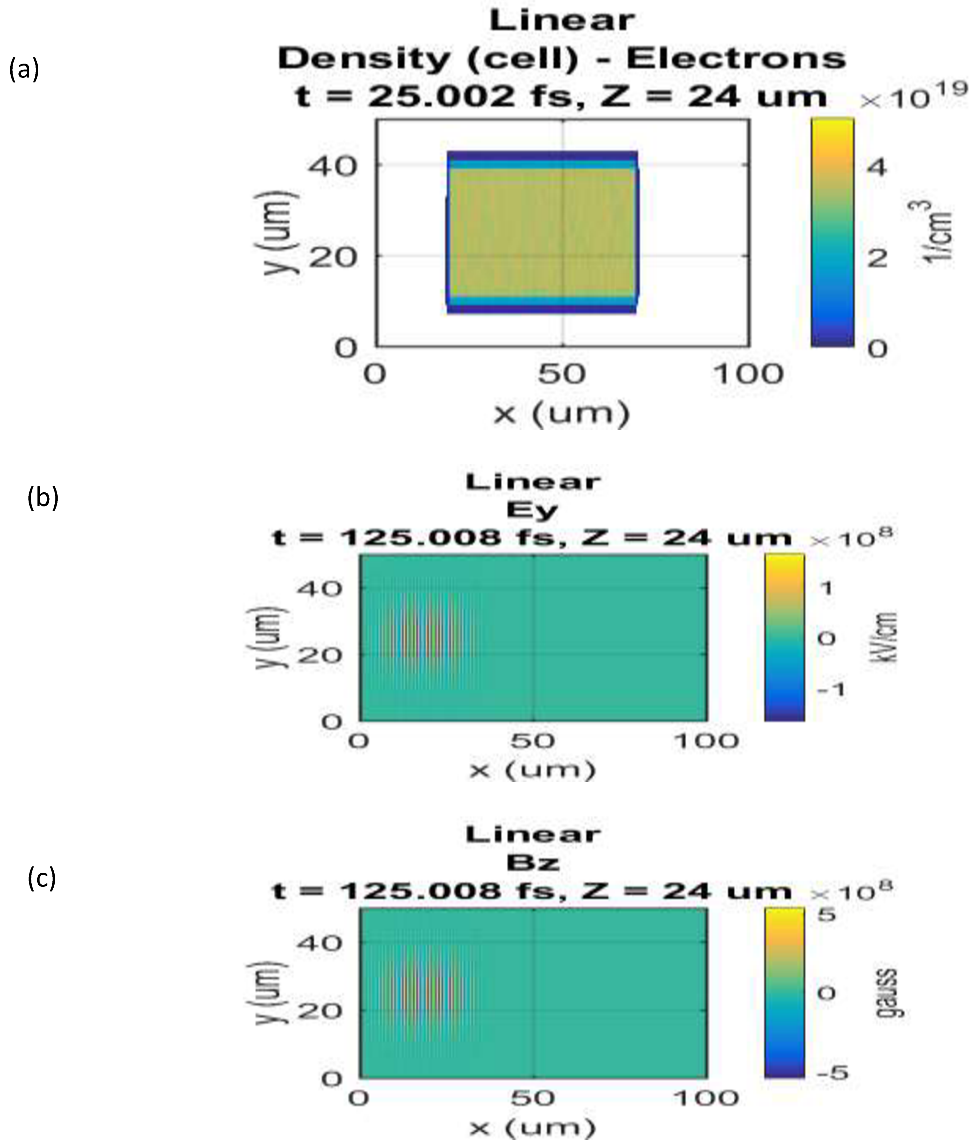

Fig 3.5: (a) Plasma slab with electron density for a plasma slab at $n_e = 3.5 \times 10^{19}\ cm^{-3}$ in a 3D grid (image shows as 2D slice at z=24 μm) at t=25 fs (b) Electric field in the y direction and (c) magnetic fields in the z direction of laser beam at time, t=125 fs in 3D grid at z=24 μm.

At an intensity, I=$3.15 \times 10^{19}\, Wcm^{-2}$, the Electric field, $E = \sqrt{\frac{2I}{c\varepsilon_0}}$ =1.5435 $\times 10^{8} kV/cm$ in vacuum. The peak Magnetic field is, B= E/c

=5.1450$\times 10^8\, G$. Fig 3.5(c) shows the magnetic field in the z direction with expected value.

Fig 3.6 shows the axial magnetic fields in x direction for different times. From them, we can see, there is no build-up of an axial magnetic field within the laser pulse.

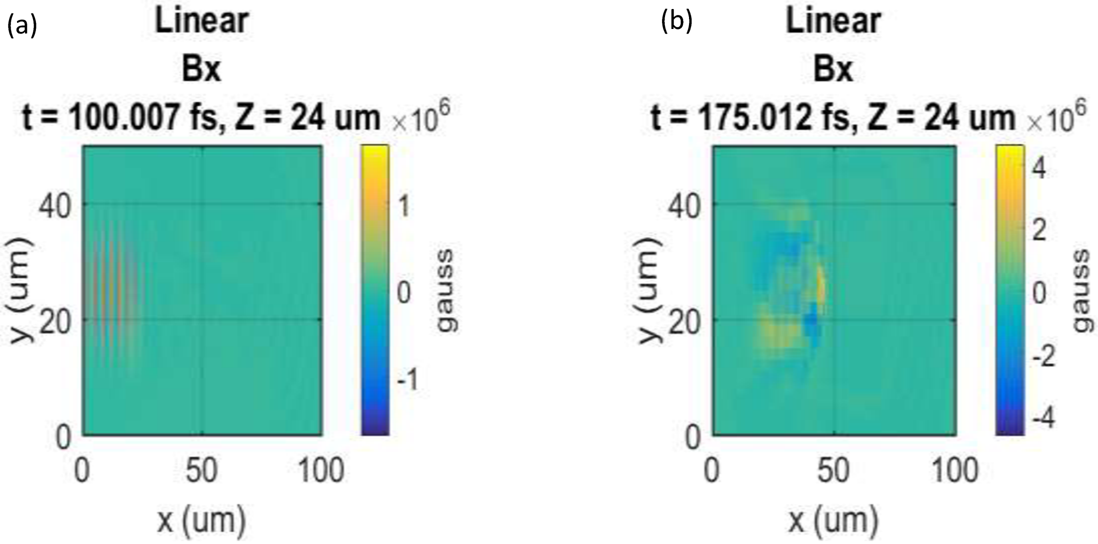

Fig 3.6: Magnetic fields in x direction (B_z) for (a) time t=100 fs (b) time, t=150 fs for an intensity of $3.15 \times 10^{19}\, Wcm^{-2}$. Images show the cross section of x-y plane at z=24 micron.

To compare with the circularly polarized light, we run the simulation for right hand (RH) and left hand (LH) circularly polarized light (CPL) with same parameters (table 3.2) except with circular polarization (y-z) with an intensity of $6.3 \times 10^{19}\, Wcm^{-2}$.

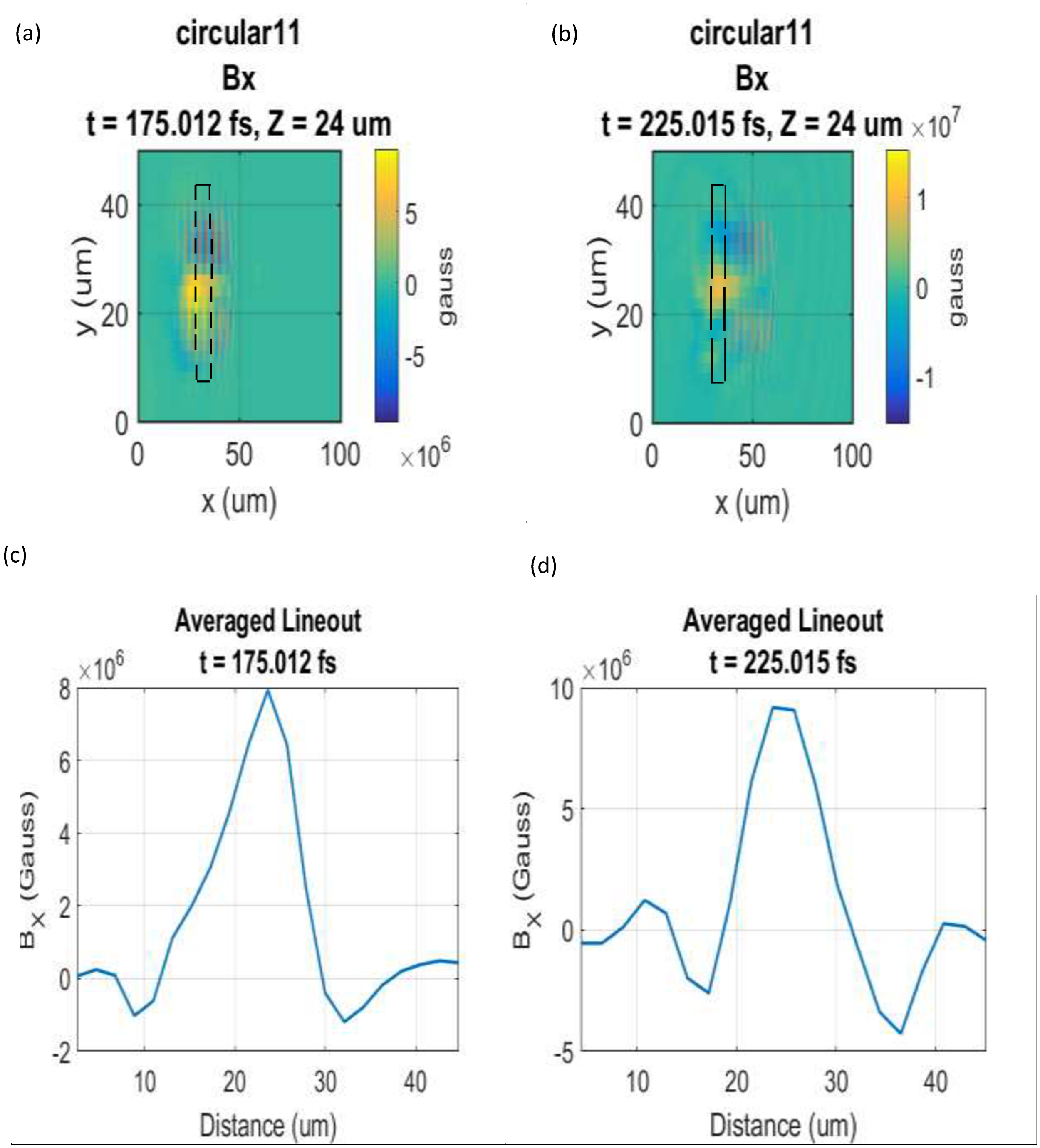

Fig 3.7: Induced axial magnetic fields due to Inverse Faraday Effect for right circularly polarized light at times (a) t=175 fs, (b) t=225 fs, and their vertical average line out drawn in y directions as shown with the dashed box in the contour plot at times (c) t=175 fs, (d) t=225 fs for an intensity of $6.3 \times 10^{19}\, W cm^{-2}$.

For left circularly polarized light (-90 phase shift between Ey and Ez), the induced axial magnetic field has the opposite polarity as shown in Fig 3.8.

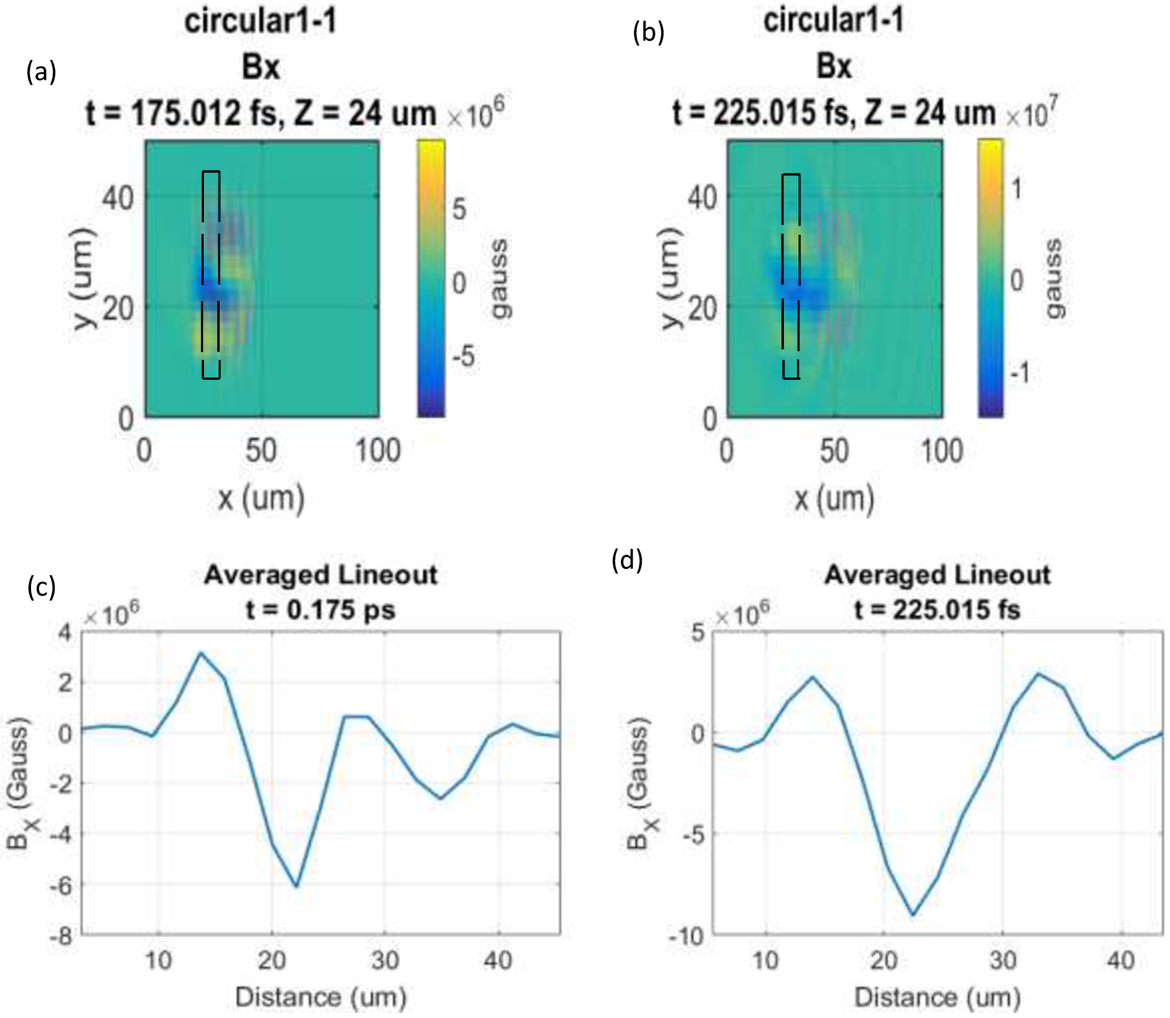

Fig: 3.8 : Induced axial magnetic fields for left circularly polarized light at times (a) t=175 fs and (b) t=225 fs and their vertical average line out drawn in y directions as shown with the dashed box in the contour plot at times (c) t=175 fs, (d) t=225 fs for an intensity of $6.3 \times 10^{19}\, W cm^{-2}$.

Fig 3.9 shows the temperature of the hot electrons at that time for right circularly polarized light and left circularly polarized light when the full slab has been heated.

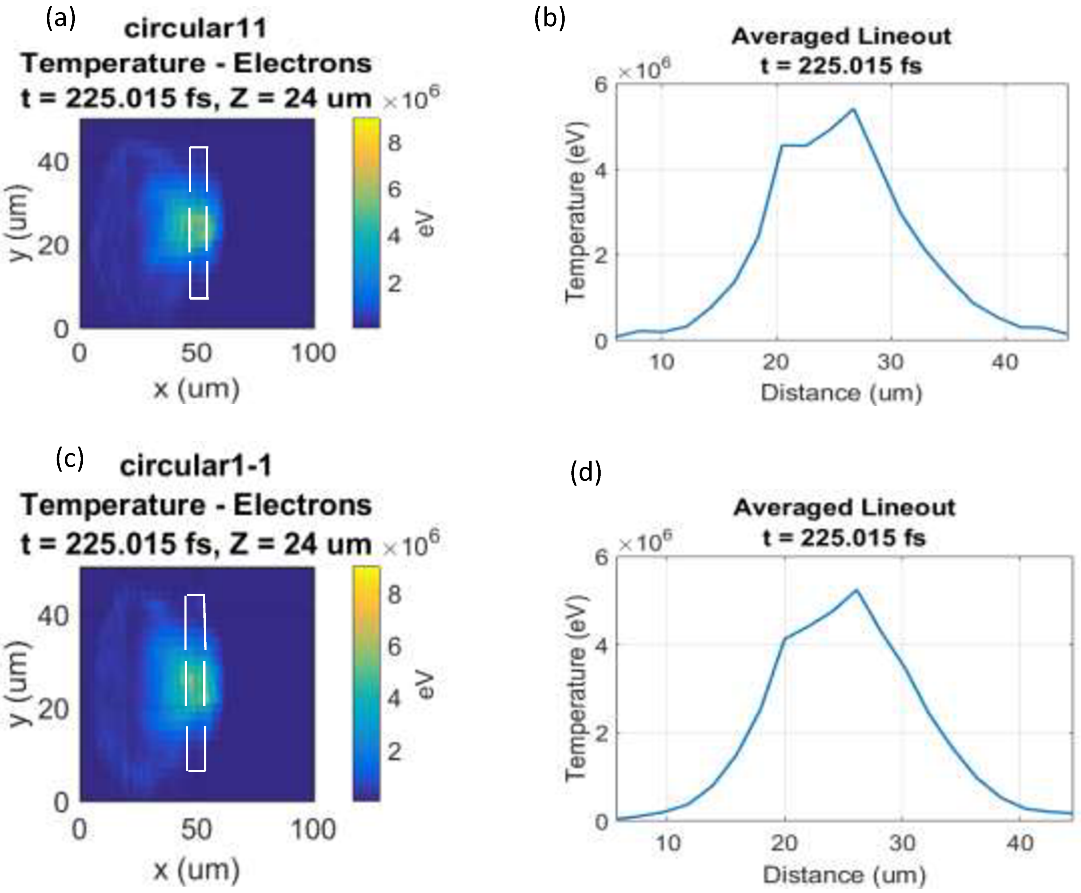

Fig 3.9: Electron temperature contour plot for (a) right circularly polarized light and (b) its average vertical line out; (c) left circularly polarized light and (d) its average vertical line out in y directions as shown with the dashed box in the contour plot for an intensity of $6.3 \times 10^{19}\, Wcm^{-2}$.

From fig 3.9, we can see that the peak electron temperature was around 5 MeV.

To understand the scaling law with Intensity, simulations have carried out with lower intensities at $6.3 \times 10^{18}\, Wcm^{-2}$ and $6.3 \times 10^{17}\, Wcm^{-2}$.

For intensity I=$6.3 \times 10^{18}\, Wcm^{-2}$, the Electric field is $Ey = Ez =$4.87 $\times\ 10^{7}\ \frac{kV}{cm}$ and Magnetic field is Bz=By =1.6223$\times\ 10^{8}\ G$ respectively.

Fig 3.10 shows the axial magnetic fields for right circularly polarized light at different time steps for an intensity I= $6.3 \times 10^{18}\, Wcm^{-2}$.

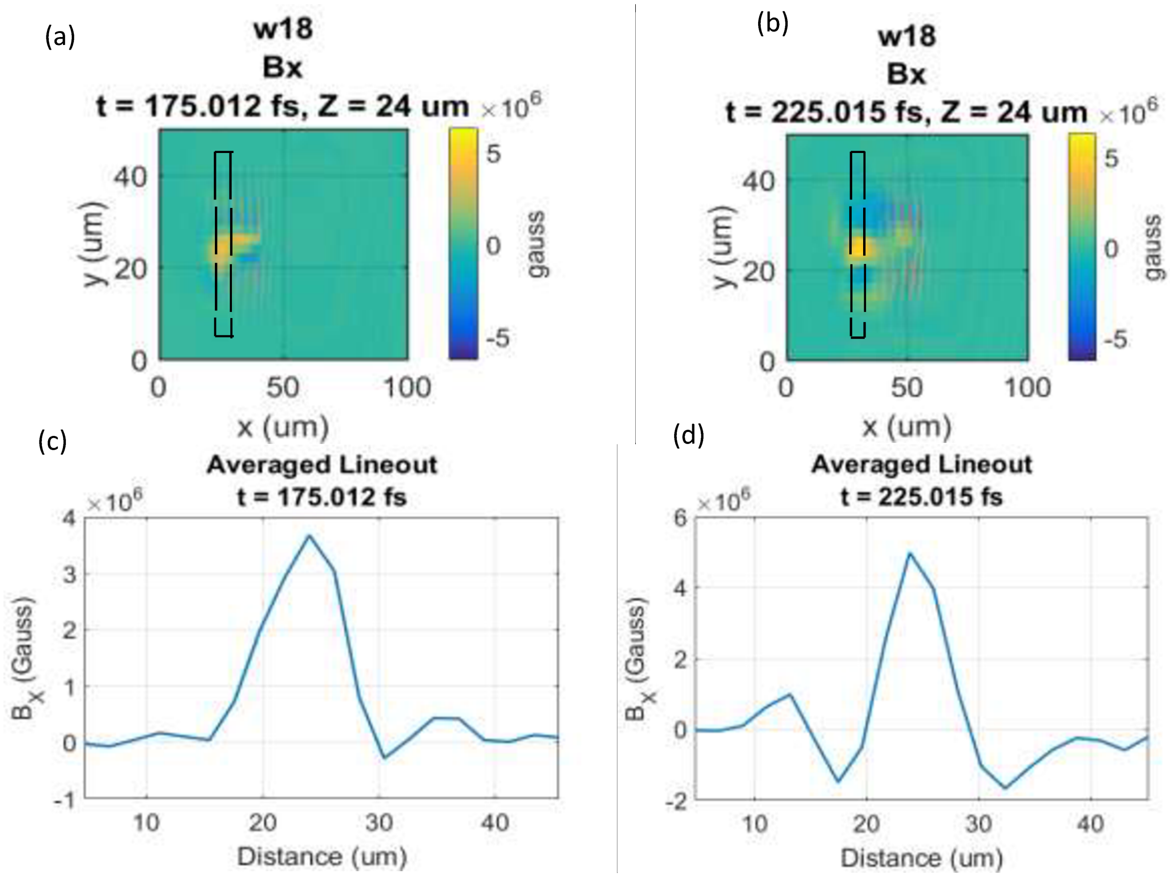

Fig 3.10: Induced axial magnetic fields for right circularly polarized light at times (a) t=175 fs and (b) t=225 fs, and their vertical average line out in y directions as shown with the dashed box in the contour plot at times (c) t=175 fs, and (d) t=225 fs, for Intensity I=$6.3 \times 10^{18}\, Wcm^{-2}$.

Fig 3.11 shows the temperature of the electrons at that time for right circularly polarized light when the induced axial magnetic fields are in highest value.

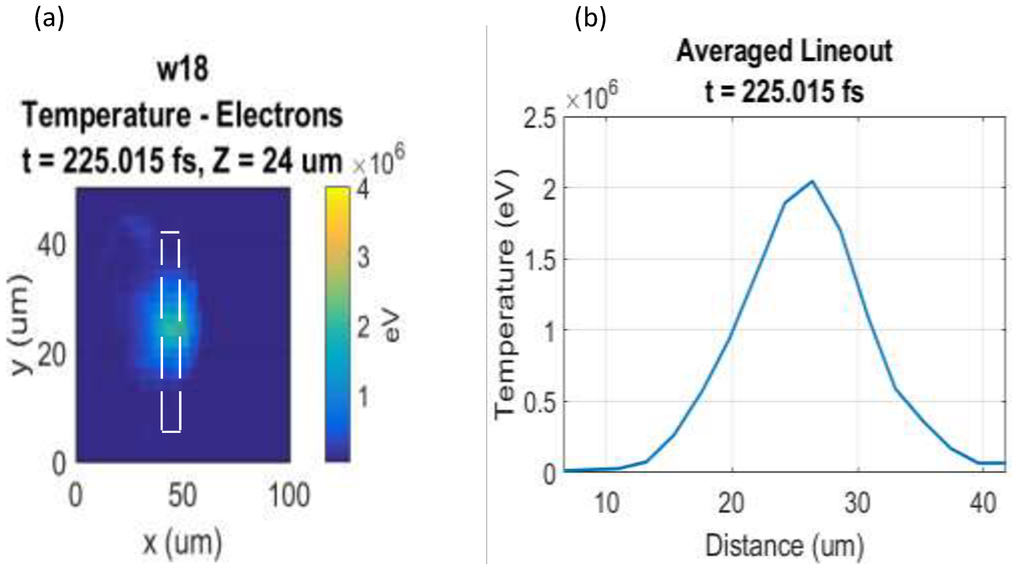

Fig 3.11: (a) Electron temperature contour plot for right circularly polarized light and (b) its average vertical line out in y directions as shown with the dashed box in the contour plot with Intensity, I=$6.3 \times 10^{18}\, Wcm^{-2}$

Fig 3.12 shows the axial magnetic fields from IFE for right circularly polarized light at time, t=175fs steps for an intensity, I=$6.3 \times 10^{17}\, Wcm^{-2}$.

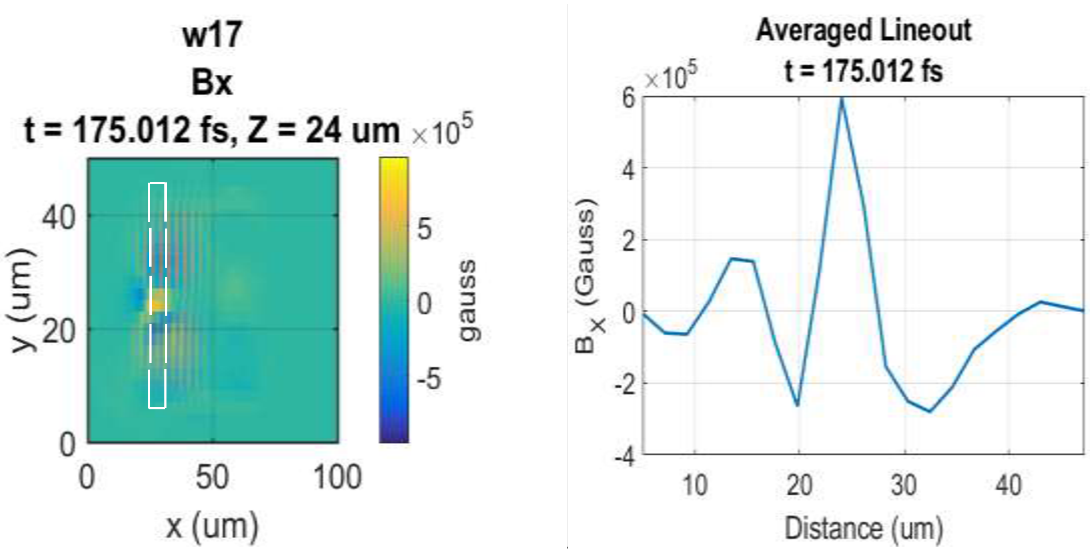

Fig 3.12: Induced axial magnetic fields for right circularly polarized light at time, (a) t=175fs, and their vertical average line out drawn in y directions from 5micron to 45micron(approx.) at time (e) t=175fs, for Intensity I=$6.3 \times 10^{17}\ Wcm^{-2}$.

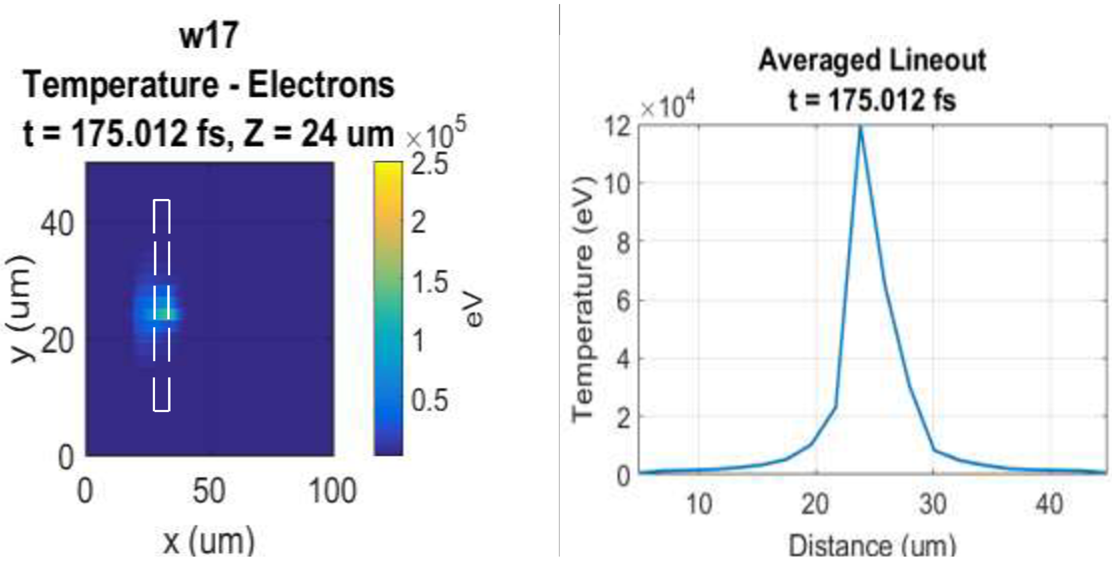

Fig 3.13: Electron temperature contour plot for right circularly polarized light (left) and its average vertical line out (right) for an Intensity I=$6.3 \times 10^{17}\ Wcm^{-2}$.

3.4.2 Axial Magnetic Field Variation with Electron Density

In order to study the scaling of expected axial magnetic fields versus density for the regime of lower intensities which can be studied in our laboratory, simulations were carried out for a wavelength of 800nm, and an intensity of $5.59 \times 10^{17}\, Wcm^{-2}$. We introduce a 50 micron slab inside the grid as shown in Fig 3.19 and run the simulations for different densities. For Linearly polarized light, there was no axial magnetic field generation, only a weak solenoidal magnetic field. But for circularly polarized light, there was an axial magnetic field that decreased with decreasing electron density.

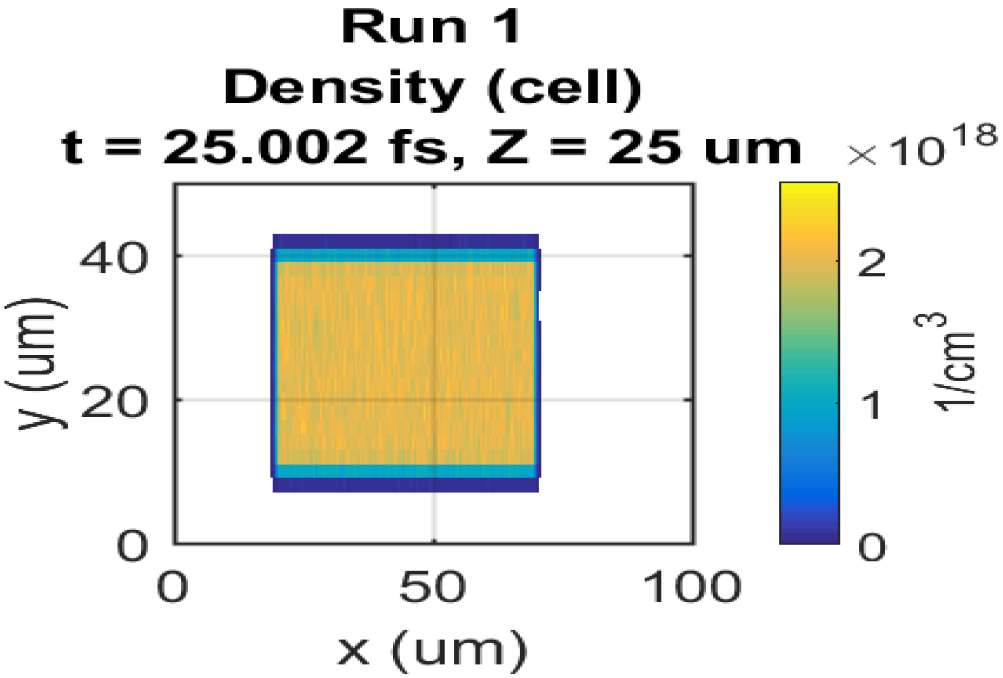

Fig 3.14: Plasma slab with electron density $2 \times 10^{18}\ cm^{-3}$ in 3D grid (image shown as a 2D slice at z=25 μm) at times t=25 fs

Table 3.3: Parameters used for different simulation runs with varying electron densities

Wavelength	800nm
Intensity	$5.59 \times 10^{17}\, Wcm^{-2}$
Spot size (FWHM)	2 µm (centered at y=25 µm and z=25 µm)
Pulse width (FWHM)	120fs
Propagation direction	X
Polarization direction (circular)	y-z
Plasma Slab Size	50 micron
No of Particles per cell	100
Cell size (x,y,z)	0.05 $\mu m, 2\ \mu m, 2\ \mu m$
Total grid size (x × y × z)	100 µm × 50 µm × 50 µm

The peak axial magnetic field was measured at t=175 fs to 225 fs and is plotted in Fig 3.20. From simulation, we have observed that, as expected, the axial Magnetic fields decrease with the electron density. The predicted magnetic fields range from 16 to 300kG.

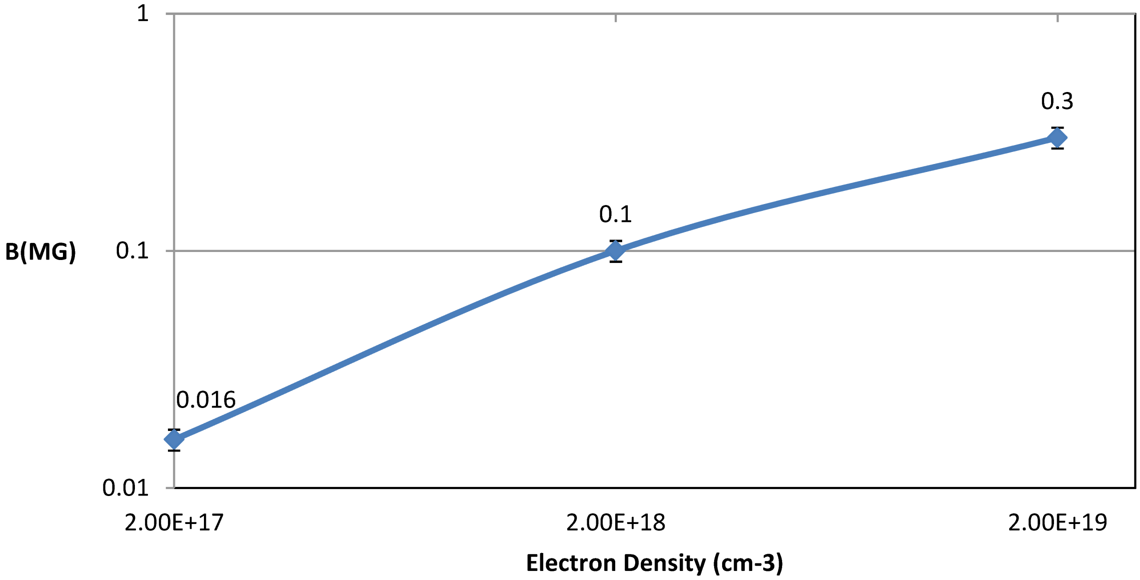

Fig 3.15: Maximum induced axial magnetic field vs electron density for circularly polarized light at a peak intensity of 5.6$\times 10^{17}\ Wcm^{-2}$

3.5 Discussion

In 1996, Z M Sheng [33] proposed a scaling law for axial magnetic field generated by IFE for a uniform plasma [33] :

$$B_{uni}=\frac{1}{2}\left(\frac{m_e w_0 c}{e}\right)\left(\frac{w_p^2}{{w_0}^2}\right)\left(\frac{3|a^2|}{2\gamma^2}-\frac{1}{2}\ln\gamma^2\right) \tag{3.1}$$

Where the Compton Magnetic field is, $B_c=\frac{mwc}{e}$ =107MG for $\lambda = 1um$ wavelength, w_p is the plasma frequency, w_0 is the laser frequency, e is the charge of an electron, c is the speed of light, a is the normalized field amplitude factor of the laser field and $\gamma=\sqrt{(1+|a^2|)}$, is the electron relativistic factor.

Najmudin [37] has proposed another scaling law based on the angular momentum generated by hot electrons spiralling in the density channel given by,

$$B_{hot}= \pi a B_C \frac{w_p^2}{w_0^2} \frac{n_h}{n_e} \tag{3.2}$$

Where n_h is the hot electron density and n_e is the plasma electron density. Considering hot electron generated by laser driven plasma, one expects scaling of the magnetic field given by $B \propto \frac{n_h}{n_e}$ and $B \propto \sqrt{I}$.

Malka [46] has proposed a scaling law for hot electron temperature for the 'self-modulated laser wakefield' regime for an underdense gas jet plasma given by:

$$T_{hot}\ (\text{MeV}) \propto {I_{18}}^{\frac{1}{2}} \approx 1.2 I_{18}^{1/2} \tag{3.3}$$

Where, T_{hot} is the hot electron temperature in MeV, I_{18} is the laser intensity in $10^{18} Wcm^{-2}$.

This prediction is compared to the results of the LSP simulation in Fig 3.16 indicating we obtain lower values than Malka's prediction. However, for the LSP result plotted the T_{hot} is calculated from all electrons in any given region in the slab. At lower intensities, the simulations show a significant decrease in temperature indicative of the fact that only a small fraction of electrons are actually hot electrons leading to a fairly low average value. At higher intensities, there is only a modest discrepancy between the LSP temperatures and Malka's scaling, but the values are smaller than the predicted value as they are the average temperature of the slab electrons. Also shown on the plots are T_{hot} value from Santala [47] and Najmudin[37] which are above these scaling laws.

Santala [47] has carried out some experimental measurements for high intensity short pulse laser interaction with a gas jet under dense plasma. The gas jet had a very homogenous density profile and a sharp edge. They mentioned that, the hot electron temperature depends on density too. Fig 3.16 shows some of their experimentally measured values for plasma density =3.5× $10^{19}\ cm^{-3}$. Gahn [48] also has carried out some experiments using a table top laser system. They used the process of relativistic self-channelling in high density plasma. Fig 3.16 shows some of their experimentally measured values for plasma density =2× $10^{20}\ cm^{-3}$.

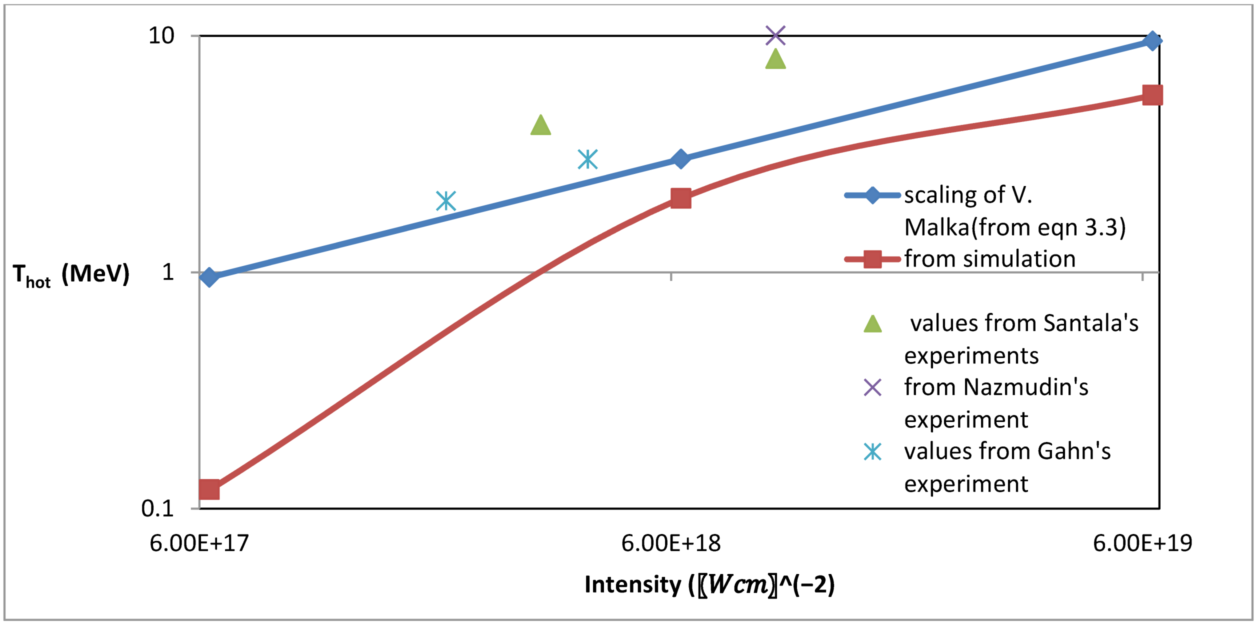

Fig 3.16: Scaling of Hot Electron Temperature with laser Intensity using eqn (3.3) (diamond) and from 3D LSP PIC simulation (squares). Values from experiments of Santala [47] and Najmudin [37] are also shown.

To predict the total number of hot electrons, Gahn [48] proposed a scaling law given by:

$$N_h \propto I^{3/2} \sim a^3 \qquad (3.4)$$

Where N_h is the total number of hot electron, I is the laser intensity and a is the normalized field amplitude factor of the laser field. In this case a 1TW laser interacted with a gas jet with an interaction volume of approximately 5micron diameter over approximately 200 micron self-focused interaction length corresponding to a total number of electrons of $N_{tot} = 8\times 10^{11}$. From Fig 3.17, one can observe at high intensities of $6 \times 10^{19}\ Wcm^{-2}$, the hot electron fraction is approximately 40%.

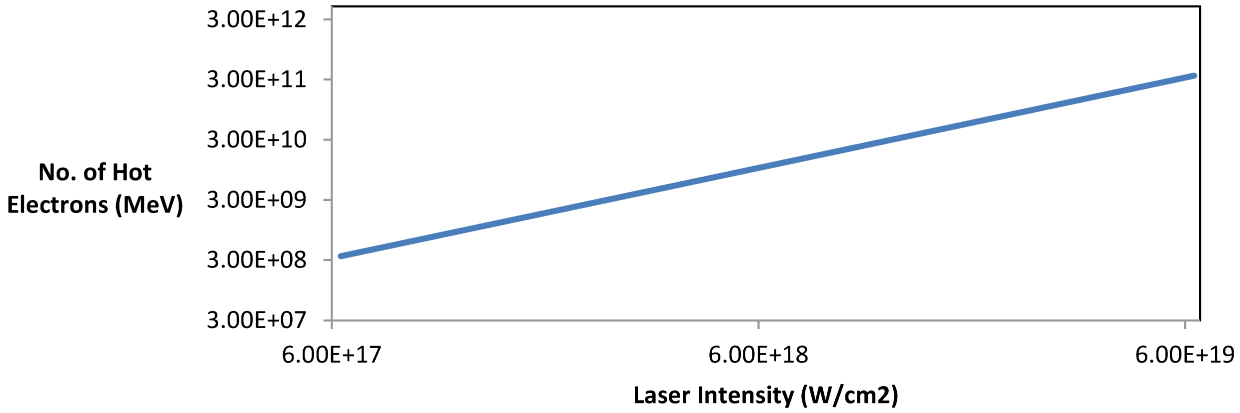

Fig 3.17: scaling law for total number of hot electron generation with laser intensity (Wcm^{-2})

Santala [47] measured the energy conversion efficiency which predicts 1% energy conversion efficiency. Even a small percentage of energy absorption can generate a large number of hot electrons for these underdense systems. Najmudin [37] also claim that they have more than 10% of the electrons as hot electrons to induce 5MG axial magnetic fields for a laser Intensity 1× $10^{19}\ W/cm^2$. They define hot electrons as those which have an energy of 10MeV or more. We will use the same assumption here to define hot and cold electrons.

From LSP 3D simulation, at a fixed time step, one can see that the hot electrons are driven forward by the laser pulse and the induced magnetic fields lag slightly behind the hottest electrons. Fig 3.18 shows that the spatial position of the hottest electrons and highest B fields are not exactly same. Hot electrons are driven ahead for the case of I=$6.3 \times 10^{19}\ W/cm^2$ and electron density, $n_e = 3.5 \times 10^{19} cm^{-3}$.

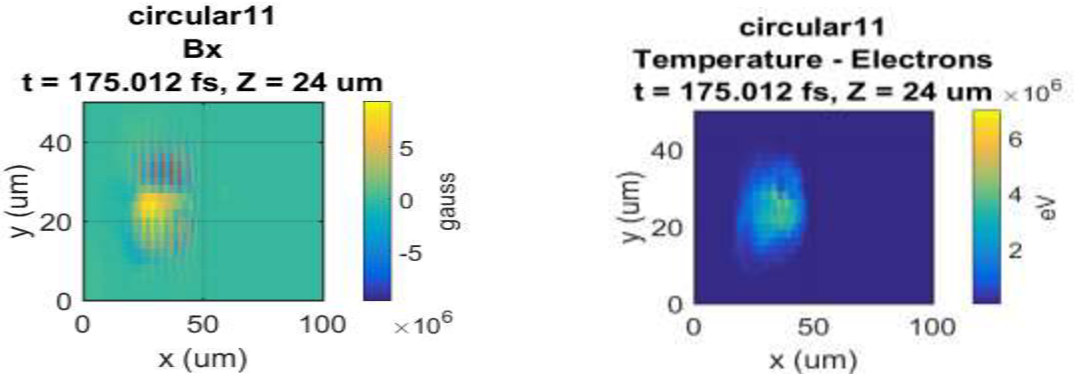
circular11
Bx
t = 175.012 fs, Z = 24 um

circular11
Temperature - Electrons
t = 175.012 fs, Z = 24 um

Fig 3.18: Contour plot of axial B field and plasma slab temperature for t=175fs for I=$6.3 \times 10^{19}\ W/cm^2$ and electron density, $n_e = 6.3 \times 10^{19} cm^{-3}$. Hot electrons are driven ahead and the induced B fields lag slightly behind.

3.19 shows the energy distribution of electrons curve for a $2\,um \times 2\,um \times 2\,um$ cube at the position where (a) the maximum B field is located and (b) where the hottest electrons are located at time t=175 fs.

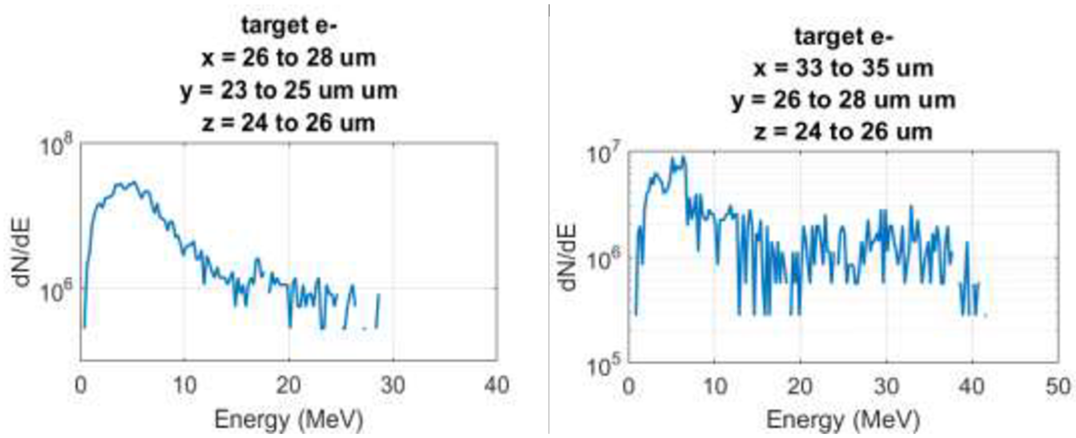

Fig 3.19: Energy distribution curve for a region of 2 μm $\times$ 2 μm $\times$ 2 μm cube at the position where (a) the maximum B fields are and (b) the hottest electrons are. The time step is t=175 fs and Laser Intensity is I=6.3 $\times$ 10^{19} W/cm^2 and electron density is $n_e = 3.5 \times 10^{19}\ cm^{-3}$.

From Fig 3.19, it is clear that we have a large number of hot electrons which can be responsible for generating the large magnetic fields (8MG) observed. From fig 3.19 (a), in the region where B field is highest, the ratio of hot electron density (>10MeV) over the total electron density is $\frac{n_h}{n_e} = 0.136$ and from 3.19(b) in the region of maximum electron temperature, $\frac{n_h}{n_e} = 0.502$.

Fig 3.20 is showing the same plots but at a later time, t=225 fs.

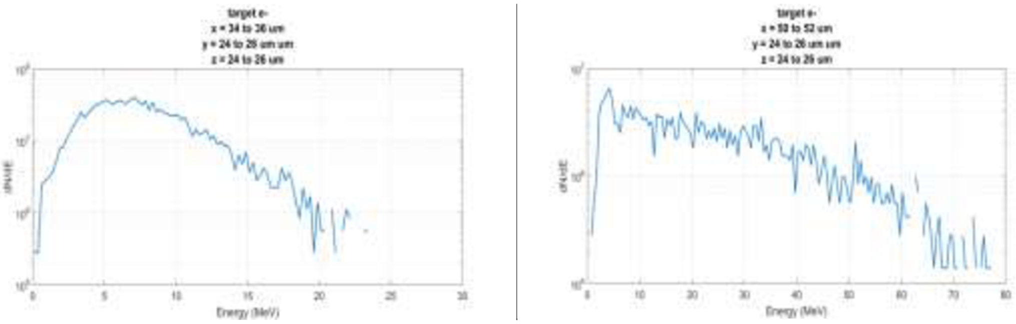

Fig 3.20: Energy distribution curve for a region of $2\mu m$ $\times$ $2\mu m$ $\times$ $2\mu m$ cube at the position where (a) the maximum B fields are and (b) the hottest electrons are. The time step is t=225 fs and Laser Intensity is I=6.3 $\times$ 10^{19} W/cm^2 and electron density is $n_e = 3.5 \times 10^{19}\ cm^{-3}$.

From fig 3.20 (a), where the B field is highest, ratio of hot electron over total electron densities is, $\frac{n_h}{n_e} = 0.239$ and for 3.19(b), $\frac{n_h}{n_e} = 0.742$.

Fig 3.21 shows the energy distribution of the electrons which escaped from the plasma slab. An extraction plane was defined 10 µm after the plasma slab at the position x=80um.

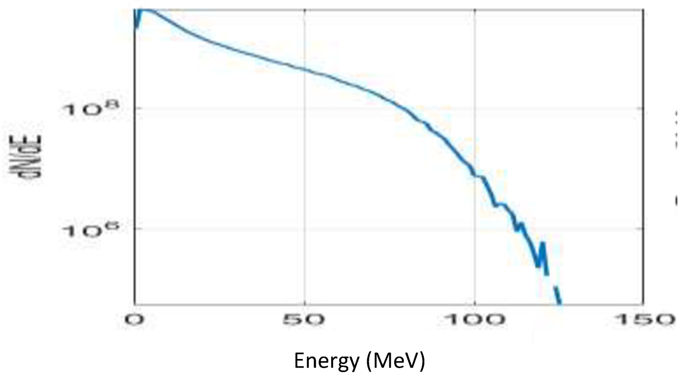

Fig 3.21: Energy distribution of the electrons for an extraction plane at x=80 µm.

The ratio of hot electrons over the total number of electrons for the extraction plane, $\frac{n_h}{n_e} = 0.594$.

From above figures and the references, it is evident that a large number of hot electrons are generated in the laser plasma interaction region.

The Magnetic fields observed from the LSP simulations and those predictions by various scaling laws are shown in Fig 3.22. Najmudin [37] mentioned that more than 10% of total fraction of hot electrons was required to generate the large induced magnetic fields. This number of hot electrons is consistent with Santala's [47] experiments. From the

LSP simulations the fraction of electrons above 10MeV in energy ranges from 0.136 to 0.239 in the region of the magnetic field generation. Thus a scaling curve for Najmudin's scaling theory is plotted assuming a hot electron fraction of 0.2 shown in Fig 3.22.

Considering spin and orbital momentum, Mendonca [12] proposed another scaling law associated with Laguerre Gaussian beams, as LG modes have OAM. Using $l = 0, p = 0$, i. e. circular polarized beams, the predicted axial magnetic field is:

$$B_z = -\frac{f_{abs}}{en_e wc}\frac{2\sigma_z}{r_0^2} I_0 \left(1 - \frac{r^2}{r_0^2}\right) \exp(-\frac{r^2}{r_0^2}) \tag{3.5}$$

Where f_{abs} is the absorption co-efficient, $\sigma_z = \pm 1$ for left handed and right handed circularly polarized light, r$_0$ is the radius of the laser beam, and I_0 is the laser intensity.

To estimate the order of magnitude of axial Magnetic fields, let assume r=r$_0$, the input laser beam radius, $\frac{\partial}{\partial r} \sim \frac{1}{r_0}$ and $f_{abs} = 1$, and for right handed circularly polarized light $\sigma_z = -1$.

The scaling laws for Sheng's and Mendonca's theories are shown in Fig 3.22 for an electron density of $n_e = 3.5 \times 10^{19} cm^{-3}$.

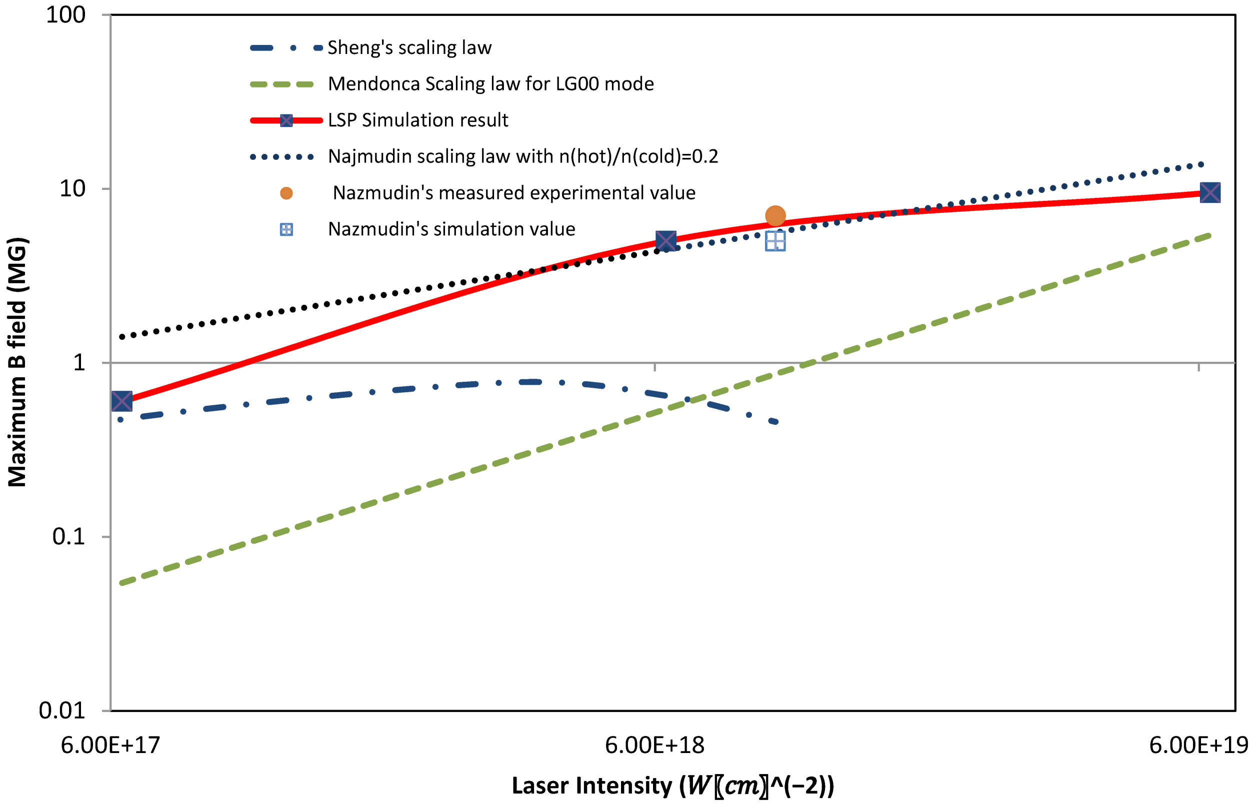

Fig 3.22: Scaling laws for the induced axial magnetic fields versus intensity for Sheng's (diamonds), Najmudin's (square & cross) and his experimental (circle) and simulation values (box), Mendonca's (triangle) theories and from LSP 3D simulations (cross).

As can be seen from Fig 3.22 both the scaling laws of Sheng and Mendonca underestimate the axial field generated compared to the LSP simulations. Najmudin also observed that the fields he measured and those he obtained from PIC simulations were much higher than those predicted by Sheng's theory. These theories do not take into account hot electron generation and the resultant currents driven by such hot electrons. Najmudin's scaling taking the spiralling hot electron current into account predicts an axial magnetic field which is of the same magnitude as we predict in our LSP simulations. Further study of the detailed dynamics of the hot electron generation and propagation will be required in order to fully understand this mechanism.

3.6 Conclusion

In this chapter, a number of simulation models predicting the scaling of the axial Magnetic fields were compared to 3D PIC simulations. The preliminary runs discussed here were used to predict the magnetic field generation and to show that indeed Megagauss level fields can be generated in interactions with underdense plasma. The scaling results obtained approximately agree with the axial magnetic field strength reported by Najmudin which are based on the generation of a large population of fast electrons leading to the generation of an axial magnetic field as they spiral around density channel created by the relativistic laser pulse. They also indicate that the fields generated can be significantly larger than those predicted simply taking into account the angular momentum coupling from the laser beam into the plasma without hot electron generation.

The results obtained here will aid in the design of experiments to measure these large fields using Zeeman splitting of emission lines. However it was observed that the numerical noise grew rapidly in these simulations on a time scales of several hundred femtoseconds for times later than the times analyzed here. Higher resolution runs would be required to study the residual magnetic fields and decay times after the laser pulse has left which would be important for the measurement of Zeeman splitting in the emission lines of the recombining plasma.

Chapter 4

Magnetic Field Measurement using Zeeman Effect

4.1 Introduction

It has been shown that magnetic fields are generated when a laser interacts with a plasma. These fields can be result from thermoelectric and pressure effects that are present in the laser produced plasma or due the Inverse Faraday Effect. To measure the magnetic field, many techniques have been already used by scientists such as Faraday rotation [17], small probe coils [49], Zeeman Splitting [50] and so on. In this thesis work, we are proposing Zeeman Splitting to measure the magnetic field produced by the laser-plasma interaction.

4.2 Zeeman Effect

The Zeeman Effect is the effect of splitting a spectral line into several components in the presence of a static magnetic field. It is a passive diagnostic allowing time resolved measurements to be made, and gives the measurement of average magnetic field along the line of sight, but not the density of the plasma and this technique does not need any probe beam. Zeeman splitting has one complication if the plasma is hot and dense since other broadening mechanism such as thermal Doppler and Stark broadening will also be observed. For high density plasma, above critical density, the selection of transition should be made in x-ray range [51].

Zeeman splitting is complex. Some lines split into three lines, some into five lines and so on and the distance that split lines are separated is proportional to a strength factor. Even without an external magnetic field, very precise measurements show that spectral lines are doublets, triplets etc due to the magnetic fields within the atom itself.

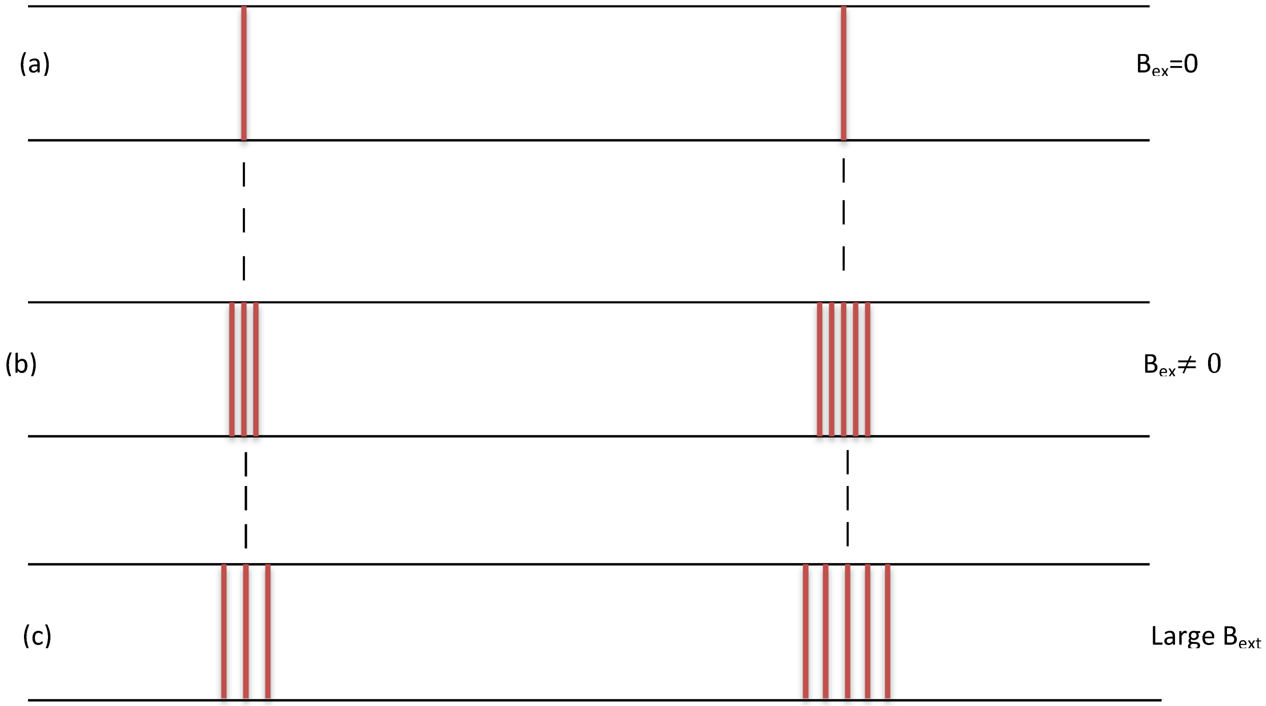

Fig 4.1: The Zeeman Effect is the splitting of spectral lines when a magnetic field is applied. The number of lines formed varies, but the spread is proportional to the strength of the magnetic field. (a) two spectral lines with no magnetic field, (b) the lines split when the field is applied and (c) a greater split is observed when the magnetic field is larger

4.2.1 Normal Zeeman Effect

The Normal Zeeman Effect occurs for spectral lines resulting from a transition between singlet states. For singlet states, the spin is zero and the total angular momentum J is equal to the orbital angular momentum L. When placed in an external magnetic field, the energy of a given orbital of an atom changes because of the additional energy of its magnetic moment in the field, which is given by:

$$\Delta W = -\mu B = \mu_z B \tag{4.1}$$

here z is the direction of external magnetic field B applied.

Now $\mu_z = -m_l \mu_B$ and Bohr magnetron,

$$\mu_B = \frac{e\hbar}{2m_e} \tag{4.2}$$

where, $\hbar = 1.054571 \times 10^{-34}\ Js$, is the reduced Planck's constant. The value of μ_B is 2.9$\times 10^{-9}$ eV/G.

From (4.1) and (4.2)

$$\Delta W = +m_l \frac{e\hbar}{2m_e} B = m_l \mu_B B \tag{4.3}$$

where m_l is the electron orbital angular momentum number. Since there are 2l + 1 values of m_l, for an orbital angular momentum l , each energy level splits into 2l + 1 levels.

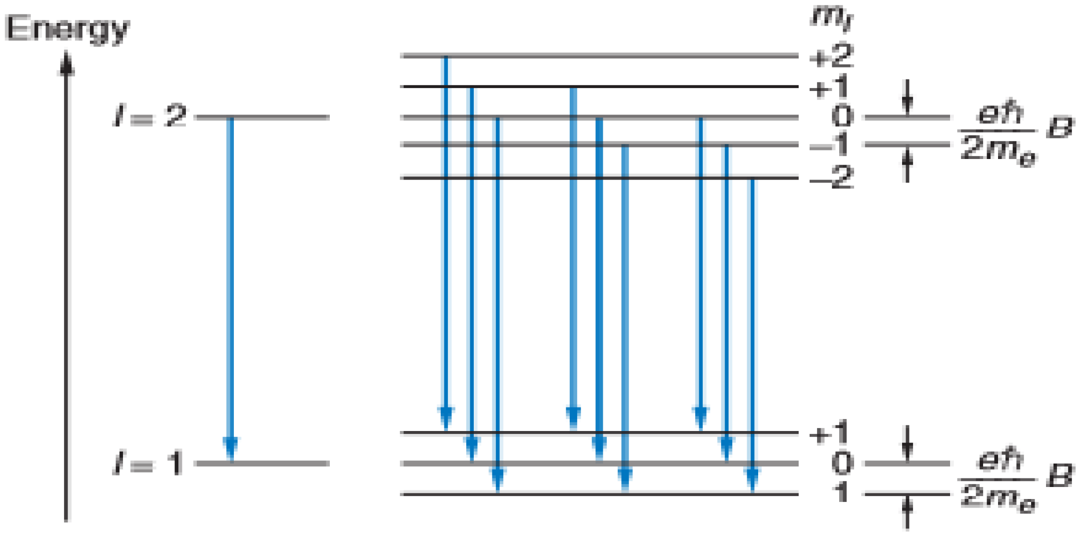

Fig 4.2: Energy level splitting in the normal Zeeman effect for singlet levels l=2 and l=1. Each level is split into 2l+1 terms. The nine transitions consistent with the selection rules $\Delta m = 0, \ \pm 1$.

Fig 4.2 shows the splitting of the levels for the case of a transition between a state with l=2 and one with l =1. The selection rule $\Delta m_l = \pm 1$ restricts the number of possible lines to the nine shown. Because of the uniform splitting of the levels, There are only three different transition energies possible: $W_0 + e\hbar B/2m_e$, W_0 and $W_0 - e\hbar B/2m_e$, corresponding to the transitions with Δm_l= +1, Δm_l = 0, and Δm_l = -1.

4.2.2 Anomalous Zeeman Effect

When the spin of either the initial or the final states, or both, is nonzero, then the Anomalous Zeeman Effect occurs. The calculation of the energy-level splitting is complicated because the magnetic moment due to spin is 1 rather than ½ Bohr magneton, and for that reason, the total magnetic moment is not parallel to the total angular momentum. Consider an atom with orbital angular momentum L and spin S. Its total angular momentum is given by [52]:

$$J = L + S \tag{4.4}$$

The total magnetic moment is:

$$\mu = \mu_L + \mu_S = g_l \mu_B \frac{L}{\hbar} + g_s \mu_B \frac{S}{\hbar} \tag{4.5}$$

Since the electron spin g-factor is $g_s = 2$ and the orbital g-factor is $g_l = 1$ we obtain

$$\mu = -\frac{\mu_B}{\hbar}(L + 2S) \tag{4.6}$$

Each energy level is split into 2j + 1 levels, corresponding to the possible values of m_j.

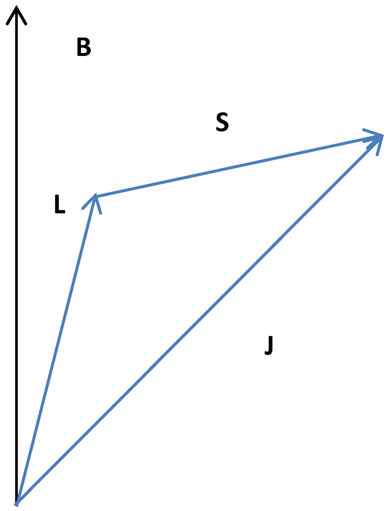

Fig 4.3: vector diagram for the total magnetic moment when S is not zero. The moment is not parallel to the total angular momentum J.

For weak magnetic fields with the internal magnetic field associated with the spin-orbit effect, the level splitting is small compared with the fine-structure splitting.

Unlike the case of the singlet levels in the normal Zeeman effect, the Zeeman splitting of these levels depends on j, l, and s, and in general there are more than three different transition energies due to the fact that the upper and lower states are split by different amounts. The energy shift relative to the position of the no-field energy level, can be written:

$$\Delta E = g m_j \left(\frac{e\hbar B}{2m_e}\right) = g m_j \mu_B B \tag{4.7}$$

where g, called the Landé g factor, is given by:

$$g = \frac{J(J+1)+S(S+1)-L(L+1)}{2J(J+1)} \tag{4.8}$$

If the external magnetic field is sufficiently large, the Zeeman splitting is greater than the fine-structure splitting. If B is large enough so that we can neglect the fine structure splitting, the Zeeman splitting is given by:

$$\Delta E = (m_l + 2m_s)\mu_B\, B \tag{4.9}$$

The splitting is then similar to the normal Zeeman Effect.

For short wavelength, The Zeeman Effect is very weak compared to Stark effect, the splitting of a spectral line into several components in the presence of an electric field. A better choice is the UV and visible domain to work with which is comparatively easy technically. However, as the plasma is very hot, the transitions that we could use for diagnosis have less probability of appearing since the plasma will be ionized to higher ionization states.

For small to moderate magnetic fields, the line broadening due to Zeeman Effect is fairly small compared to the typical line breadth. For example, 50KG of magnetic field could give a Zeeman splitting separation of $0.2A^0$ for the most intense Zeeman component of Cv line of 227.1nm where the half width of this line is $3.4\ A^0$ at a density of $5\times 10^{16}\ cm^{-3}$ for Scylla I [53]. To overcome this problem, one can take advantage of the opposite circular polarizations of the symmetrically displaced Zeeman components in a longitudinal field. If the two opposite polarizational components can be detected separately from the line center position, then their relative separation is a function of the magnetic field.

The expected Zeeman shifts can be given by [54]:

$$\Delta\lambda_z = gK\lambda^2 B \tag{4.10}$$

where g is the Lande splitting factor, $K=4.7\times 10^{-5} cm^{-1} G^{-1}$ and wavelength λ is in cm.

N. J Peacock [54] found that, for magnetic fields B of the order of 10^6 G, the Zeeman splitting can amount to several angstroms. They claimed, above $8\times 10^5 G$, Zeeman splitting exceeds Thermal-Stark Broadening.

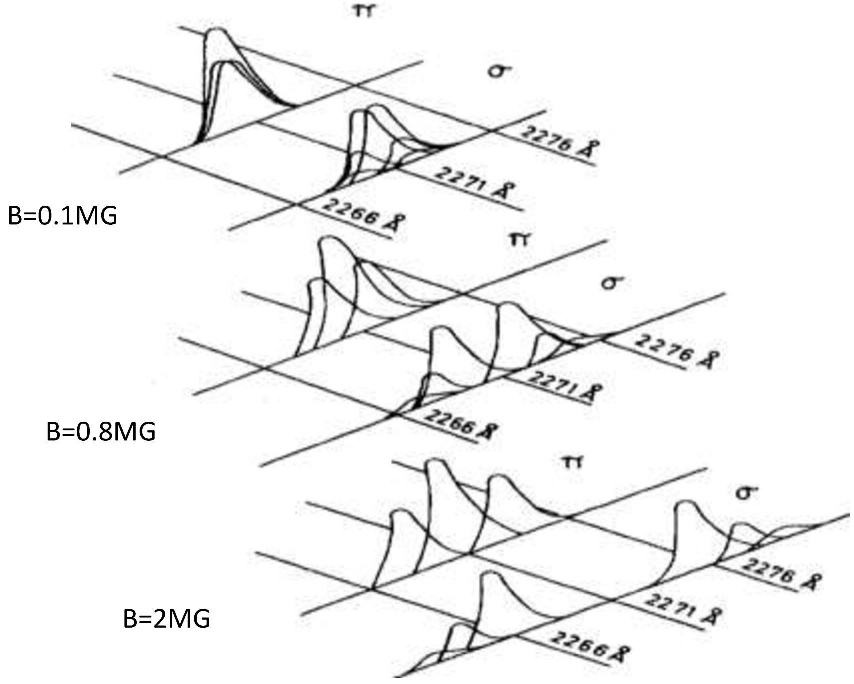

Fig 4.4: calculated emission profiles for carbon plasma viewed orthogonal to a magnetic field. 3 sets of profiles are given for increasing magnetic field strength: 0.1 MG, 0.8 MG and 2 MG with polarization parallel (π) or perpendicular (σ) to the B-field [54].

Carolan and Peacock [55] also used CII 657.8nm & CII 658.3nm doublet lines for measuring Zeeman splitting and measured a splitting of 0.072nm splitting for CII doublet at 658.3nm with a magnetic field strength of 2.66T and 0.053nm splitting for the CII doublet at 657.8nm with 2.63T. J. Gafert [56] used CIII (464.8nm) and K. Krieger [57] used CII 589.1nm lines for Zeeman splitting in their experiments. In this thesis, we assess the use of CII doublets at 658.3nm and at 657.8nm lines to measure magnetic field using Zeeman Splitting.

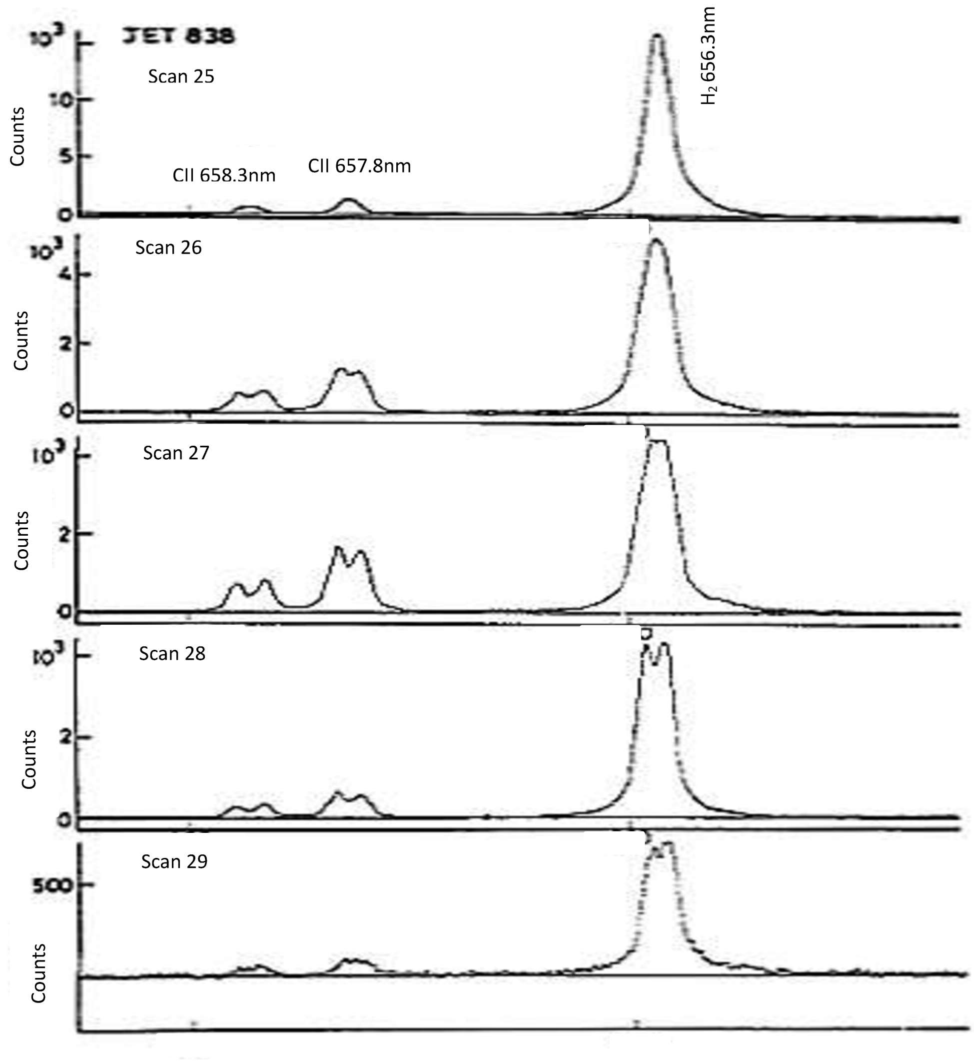

Fig 4.5: Zeeman Splitting due to the presence of magnetic field for CII doublet at 657.8nm and 658.3nm and the H_2 line at 656.3nm. 1st scan shown here is the reference one taken during the midway of a pulsed Tokamak (JET) discharge. The remaining scans are taken at 50ms intervals. [55]

4.3 Expected Ionization and Ionization Defocussing

The initial proposed experiment is to focus a 100fs laser pulse into a low density gas target in order to observe the emission lines of various elements such as nitrogen, oxygen and carbon and look for Zeeman splitting of these emission lines due to the self-generated axial magnetic fields. Based on the theoretical assessment of ionization defocusing given in chapter 2 and assessment of defocusing effects, maximum ionization states and volume of each ionization state based on tunnel ionization is given here for conditions of our experiment.

In order to assess whether ionization defocusing will limit the peak intensities that can be achieved the maximum intensity is calculated for different starting atomic densities of Nitrogen for an input cone half angle of C = 0.2 radians and input power of P = 1GW (corresponding to 100 uJ in 100fs) is calculated using eqn 2.36 and plotted in Fig. 4.6 (a). It can be seen that the ionization refraction effect only plays a role in limiting the peak intensity for atomic densities above 3×10^{18} cm^{-3} which is equivalent to 1/20 atmosphere of nitrogen. A similar calculation for P = 1TW and C=0.1 rad, is shown in Fig 4.6 (b). From the figure, it can be seen that ionization defocusing would play a role at atomic densities down to 3×10^{17} cm^{-3} or 1/200 of an atmosphere. However, at these higher power levels where the power exceeds the critical power for self-focussing the additional effect of relativistic self-focussing must be taken into account as investigated by Fedosejevs et al. in ref [31].

The plot for oxygen is fairly similar. Thus at pressures of 50 Torr or less for our current experimental case of P=1GW, ionization defocusing can be ignored and one can assume an ideal Gaussian beam focus for the laser pulses. In this case the volume which is ionized above each ionization threshold can be calculated which would give an indication of the signal strength for each ionization stage at the focus of the pulse.

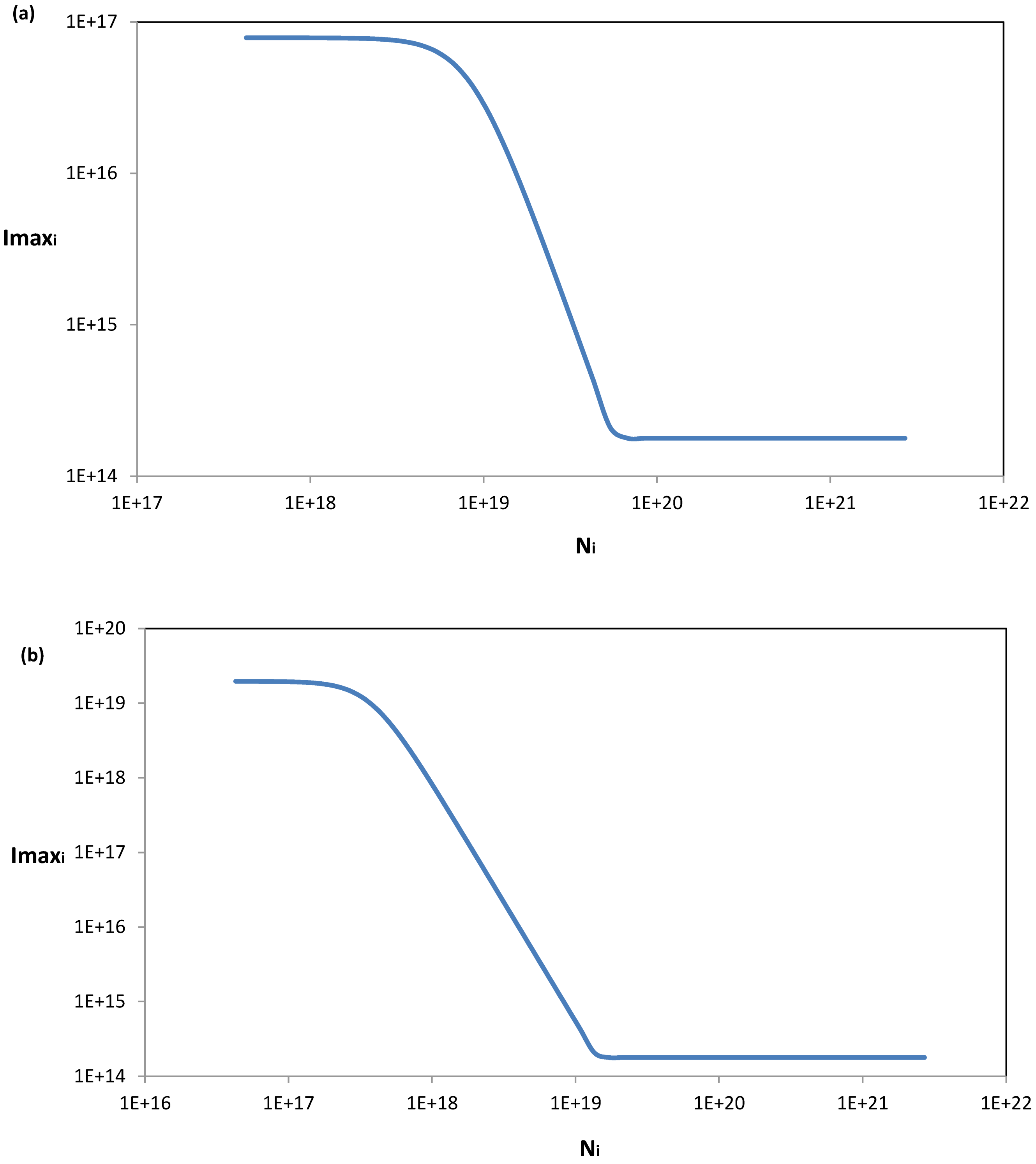

Fig 4.6 (a) Maximum intensity for p = 1GW, λ_0 = 800nm, C =0.2 rad focused beam in nitrogen as a function of atomic density of nitrogen and (b) the same for P = 1 TW and C =0.1 rad.

For an ideal Gaussian beam the beam radius is given as a function of axial position, z from the minimum beam radius position by:

$$r(z) = r_{0,min} (1 + z^2/z_0^2)^{1/2} \tag{4.11}$$

where the Rayleigh range, z_0, is given by:

$$z_0 = \lambda_0/(2\pi C^2) \tag{4.12}$$

The volume enclosed by the beam radius up to the point z can be found by integrating the Gaussian beam profile given by eqn.8 and is then given by:

$$V = \int_0^z 2\pi\, r_{0,min}^2 (z + z^3/3z_0^2) \tag{4.13}$$

Using the ionization threshold energy given by eqn. (2.30) and the power law relation for ionization potential and ionization state given by eqn. (2.31) the equivalent beam radius for each threshold intensity can be calculated and the axial position where it occurs can be determined from eqn. (4.11). The resulting beam radii, axial positions and estimated volume of emission for each ionization state, taken as the volume within the beam radius from the beam waist up to this axial position, is then plotted in Fig. 4.7 for the case of nitrogen when ionization defocussing is not important.

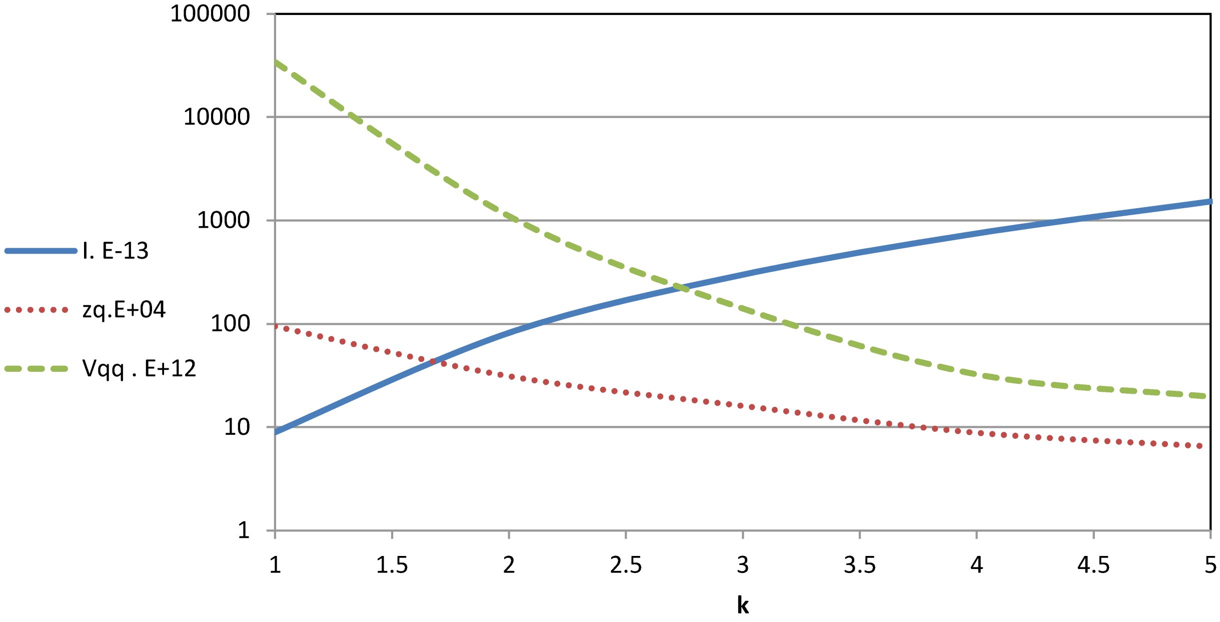

Fig. 4.7: Plot of ionization intensity, axial position and Volume for each ionization state in nitrogen gas for C=0.2. The units are $10^{13} W cm^{-2}, 10^{-4}\ cm\ and\ 10^{-12}\ cm^{3}$ for intensity, axial position and volume respectively.

It can be seen that the estimated ionization volume for ionization states of +1 and +2 are much larger than the volume of ionization states of +4 and +5 by a factor of 30 to 1000 times. Thus depending on the imaging system and slit resolution employed for measuring the spectra the dominant emission will come from the lower ionization states. A more exact calculation of emission volumes should take into account the radial distribution of the Gaussian beam profile and integrate in 2D cylindrical geometry.

4.4 Experimental Setup

We wish to study the magnetic fields produced by high intensity laser pulse propagation in underdense plasma. To conduct an initial experiment, we use 800nm linearly polarized Ti:Sapphire laser pulses with energy of 340 µJ to create the plasma. The pulse duration was 150fs at a 1 kHz repetition rate and it was focused using a 10x microscopic object with numerical aperture of NA=0.1 inside a gas chamber. Carbon dioxide was used as the gas target. An aspheric f/1 lens was used as the collection optics and an f/4 parabolic mirror was used to focus the plasma light onto the spectrometer slit. Carbon Dioxide (CO_2) has been used as the main interaction gas inside the gas chamber.

4.4.1 Spectrometer and Detector

We use a Czerny-Turner spectrograph and ICCD (Intensified CCD) to measure the spectra.

A Czerny-Turner spectrograph has an entrance slit, two focusing mirrors and a diffraction grating as shows in Fig-4.8.

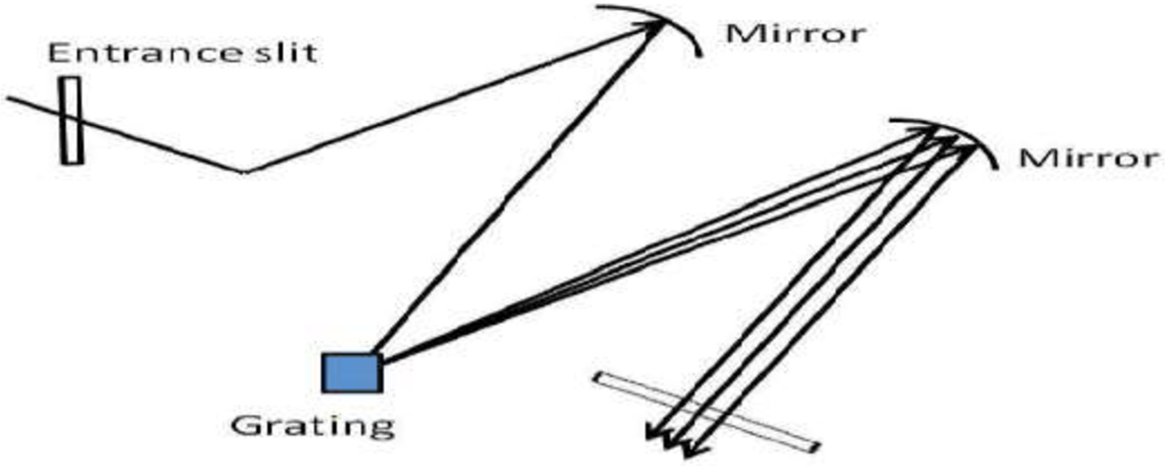

Fig 4.8: schematic diagram of a Czerny-Turner spectrograph

Light is focused onto the entrance slit using a parabolic mirror and then diverges reaching the first mirror. This mirror collimates the light as a parallel beam onto the diffraction grating. Diffracted beams then are imaged onto the detector (ICCD) by a second concave mirror. There is a trade-off between the total bandwidth of acquisition and the resolution of a Czerny-Turner spectrometer which can be controlled by choosing the ruling of the grating. For higher resolution, a very fine grating ruling is used and the total wavelength range is narrow while a wide wavelength region can be obtained by using a suitable grating with very low spectral resolution. Here, we use an Oriel MS260i spectrograph, with a 1200lines/mm grating.

We use an ICCD (Intensified Charge Coupled Device) in this experiment as a detector. An ICCD improves the signal to noise ratio (SNR) and is better for time-resolved detection using time windows of a few nanoseconds. The intensifier unit in an ICCD is composed of a photo cathode, a micro channel plate (MCP) and a phosphor screen. The photocathode converts incident photons into electrons. These electrons are accelerated towards the MCP by an applied control voltage and then multiplied by a large factor inside the MCP. These electrons are further accelerated and strike the phosphor screen that converts the multiplied electrons back to photons. Finally, the Photons are brought to the CCD with a fibre optic coupler. The gate window functionality in an ICCD is normally obtained by pulsing the control voltage applied between the photocathode and the MCP during the desired time interval. Photoelectrons cannot reach the MCP during the period when the voltage is revered and no output from the phosphor screen will be generated.

4.4.2 Grating Wavelength Calibration

The spectrometer we have used in our experiment has 3 gratings: 150lines/mm, 1200lines/mm and 2400lines/mm. To carry out a spectrometer wavelength calibration, we used an Hg-pencil type discharge lamp (Oriel6035) and 1200 lines/mm grating. A central wavelength can be chosen by a hand controller. The dispersed light from the grating is analyzed by the ICCD. Sansonetti [58] has calibrated the Hg lamps in detail and we have taken those calibration lines as references. We then use a linear fit for spectral calibration as shown in Fig 4.9. Given that each pixel on the ICCD is 25 µm, the resultant dispersion obtained is 3.3nm/mm.

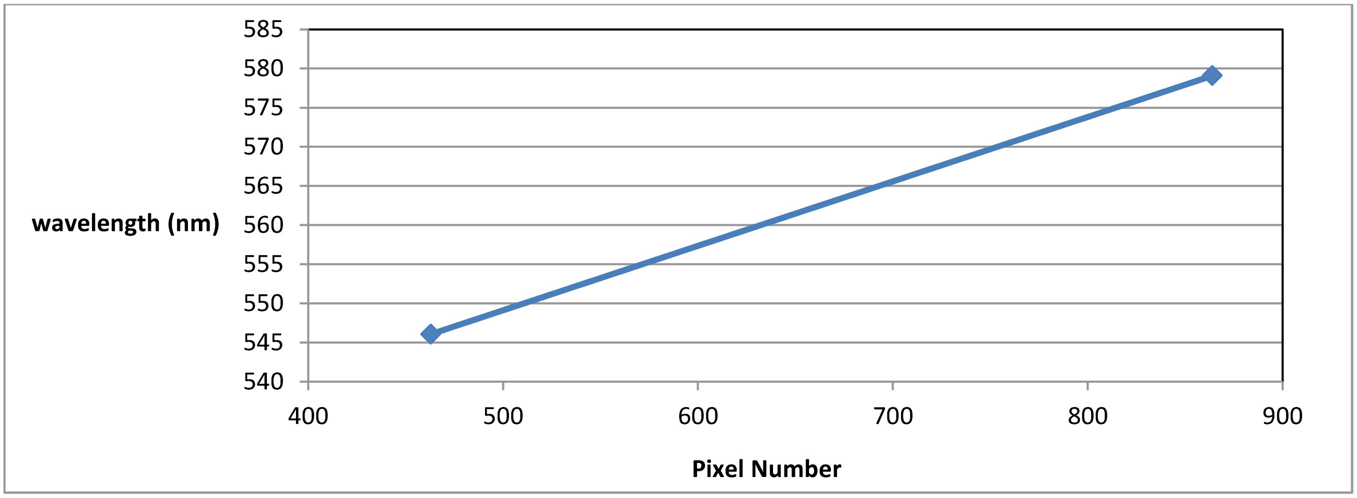

Fig 4.9: Wavelength calibration for the 1200lines/mm grating with central wavelength 550nm

4.4.3 Plasma Imaging

To measure the emission spectrum, focusing the plasma light onto the slit is required. The size of the plasma depends on laser pulse energy and background conditions. We have used an aspheric f/1 lens and two mirrors to guide the light and an f/4, 10 cm effective focal length parabolic mirror to focus the beam onto the spectrometer slit as shown in Fig 4.10.

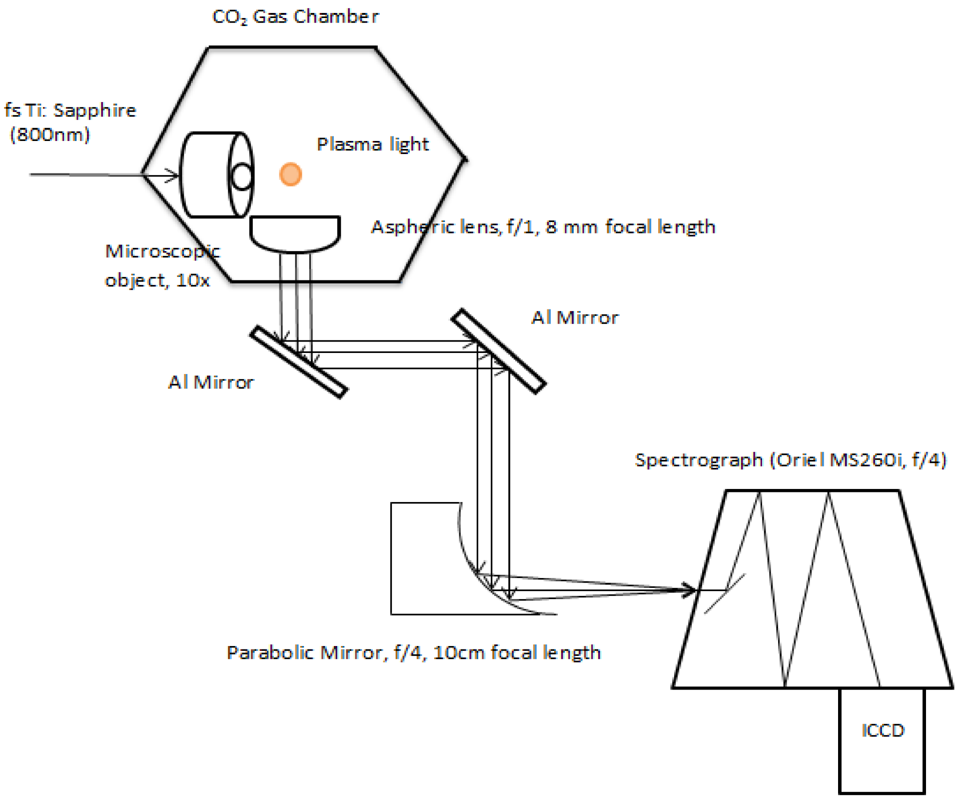

Fig 4.10: schematic diagram of the experimental setup for Plasma imaging

4.4.4 Gate Width and Gate Delay of ICCD Camera

The time of arrival of the laser pulse at the target position is important. Here, the ICCD has a gated time window that we can use to acquire the signal when the emission is optimum and to block the initial continuum emission if required. We can add a delay with a delay generator to control the gating of the ICCD and set a suitable delay time to get an optimum spectrum. The ICCD can accumulate as many shots as we want and also can add gain using the MCP and the phosphor screen to improve the signal to noise ratio. To set the gate delay, we take shots using fixed gate width (200ns) and variable gate delay (shown in Fig 4.11).

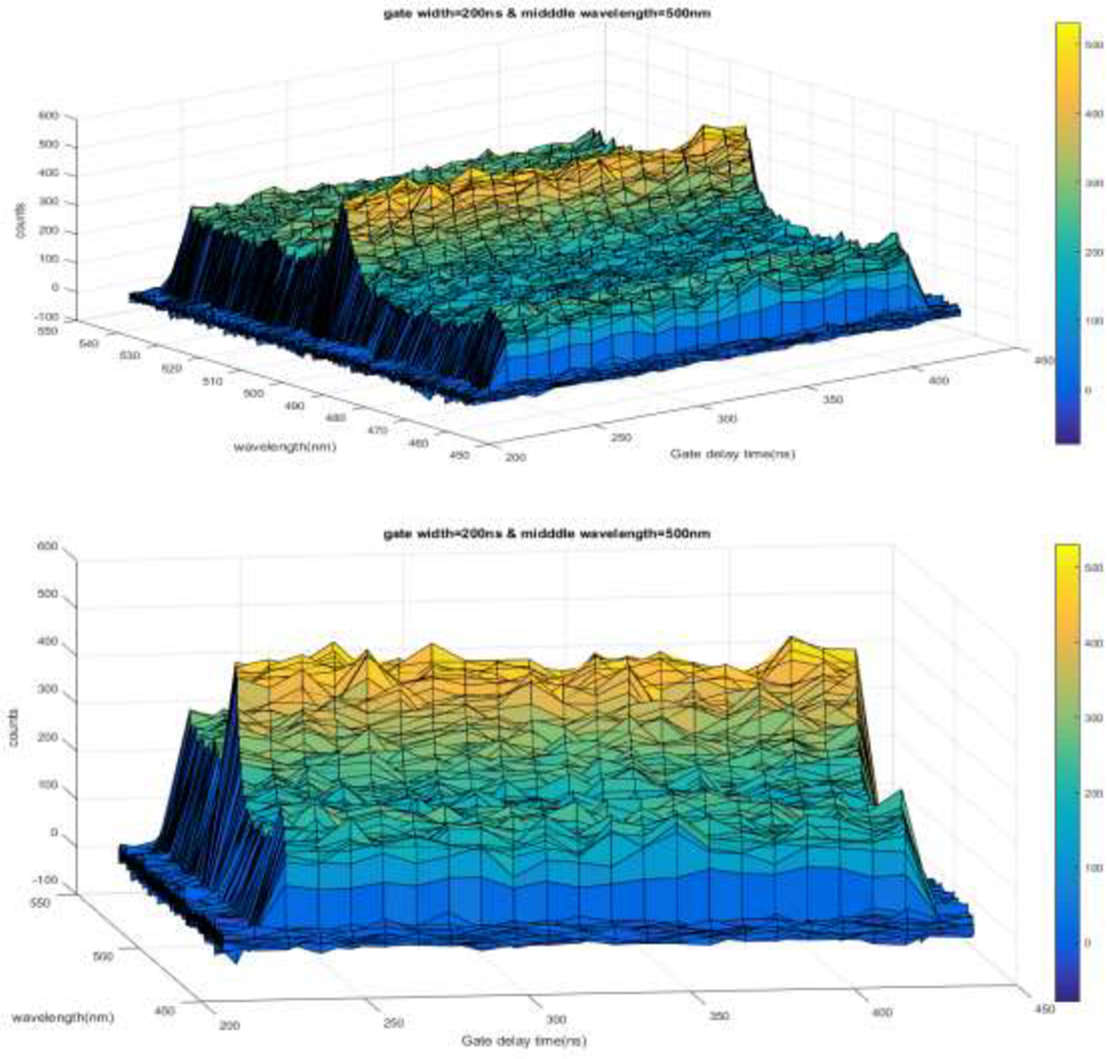

Fig 4.11: Temporal scans with a fixed gate width (200ns) and variable gate delay using single scan and 500nm middle wavelength for the spectrograph. The gate delay is relative to an electronic trigger output from the Ti:Sapphire laser. Data shown for air spectrum at one atmospheric pressure.

From above figure, we choose the gate delay 330ns with a fixed gate width of 200ns for our emission measurements to get optimal data as plasma starts forming from 250ns and dies around 445ns.

4.4.5 Spectral Resolution

The spectral resolution was measured using a 150 micron entrance slit and it was around 0.49 nm. We used the 546.0750 nm emission line of an Hg-pencil type discharge lamp (Oriel6035) and 1200lines/mm grating with the central wavelength set at 550nm to make the measurement.

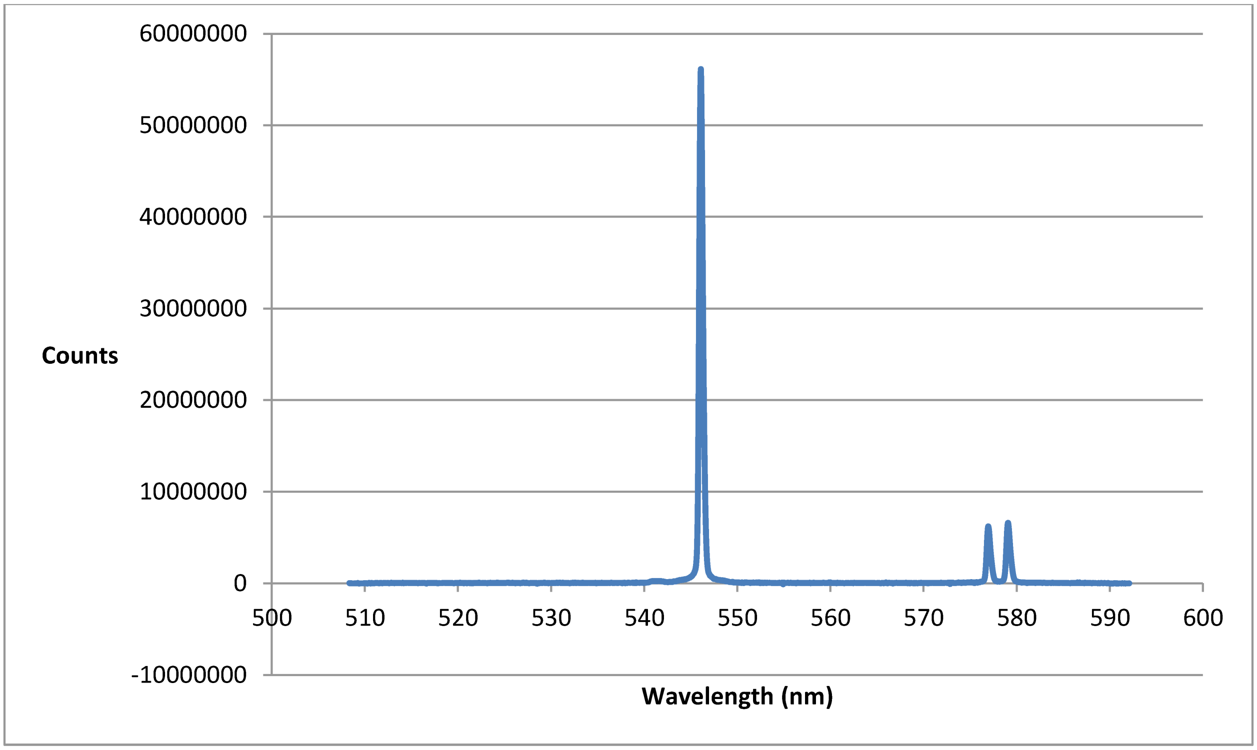

Fig 4.12: Spectral resolution measurement using Mercury lamp and Oriel MS260i spectrograph with a central wavelength setting of 550 nm and a 150 um entrance slit.

4.5 Experimental Data Analysis

Initial Experimental data has taken to characterize the conditions for measuring Zeeman splitting. Line width and intensity ratio was measured for various pressures for separate lines. As mentioned before (sec 4.4.4), the ICCD has a gated window and we can set the time when the camera gate window will open by sending an external trigger. The data has been taken using a 200ns gate width. The gate pulse delay was 330ns and MCP gain was set to 150. We accumulated 1000 measurements together with the camera exposure time set to 0.1s for each accumulation. A Ti:Sapphire laser with 1kHz repetition rate was used. The laser energy was 100 μJ. The energy was measured by making an average power measurement past the interaction point using a power meter in air. Fig 4.13 and Fig 4.14 shows (a) the line width variation (FWHM) and (b) the intensity variation with pressure for CII (657.8nm & 658.3nm) and CIII (464.8nm) lines.

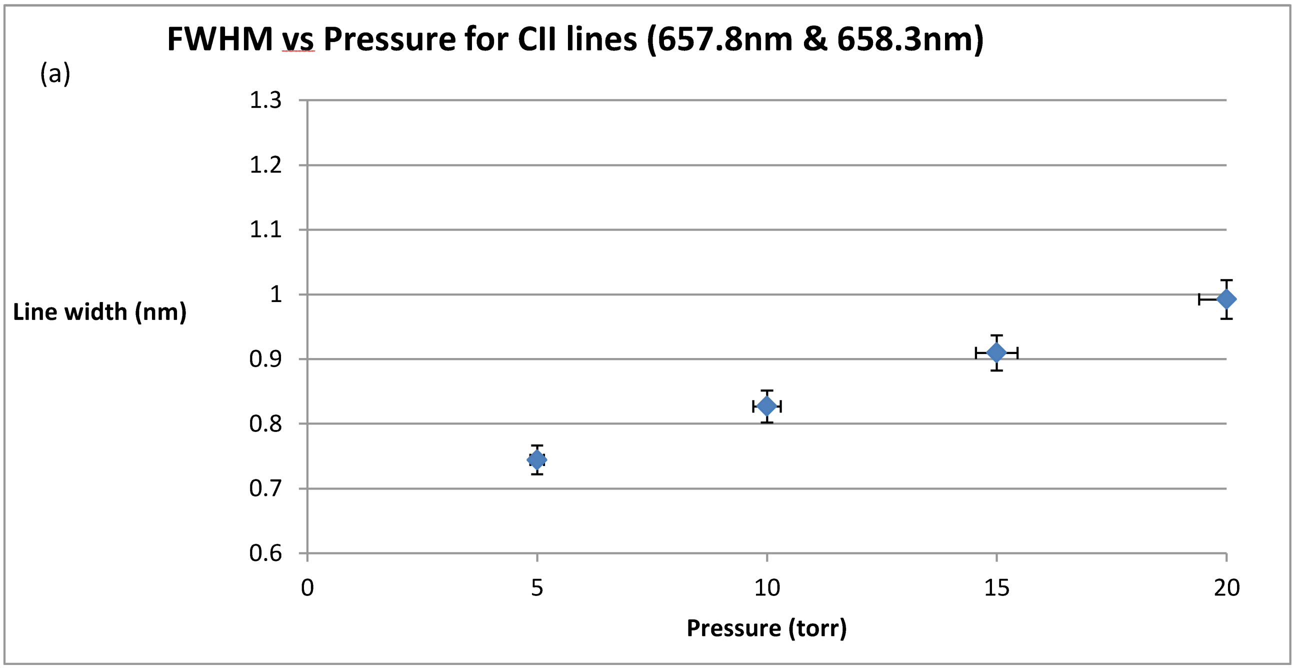

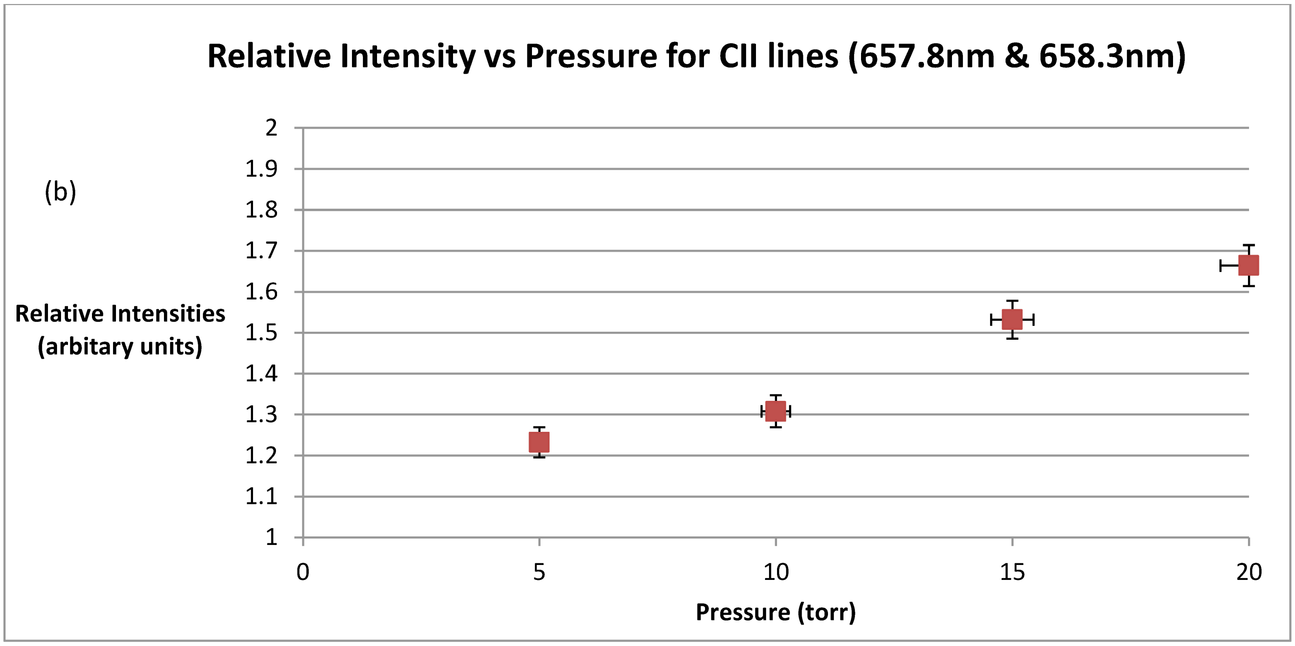

Fig 4.13: (a) Line width (FWHM) vs Pressure and (b) relative Intensity vs Pressure plot for CII doublet lines

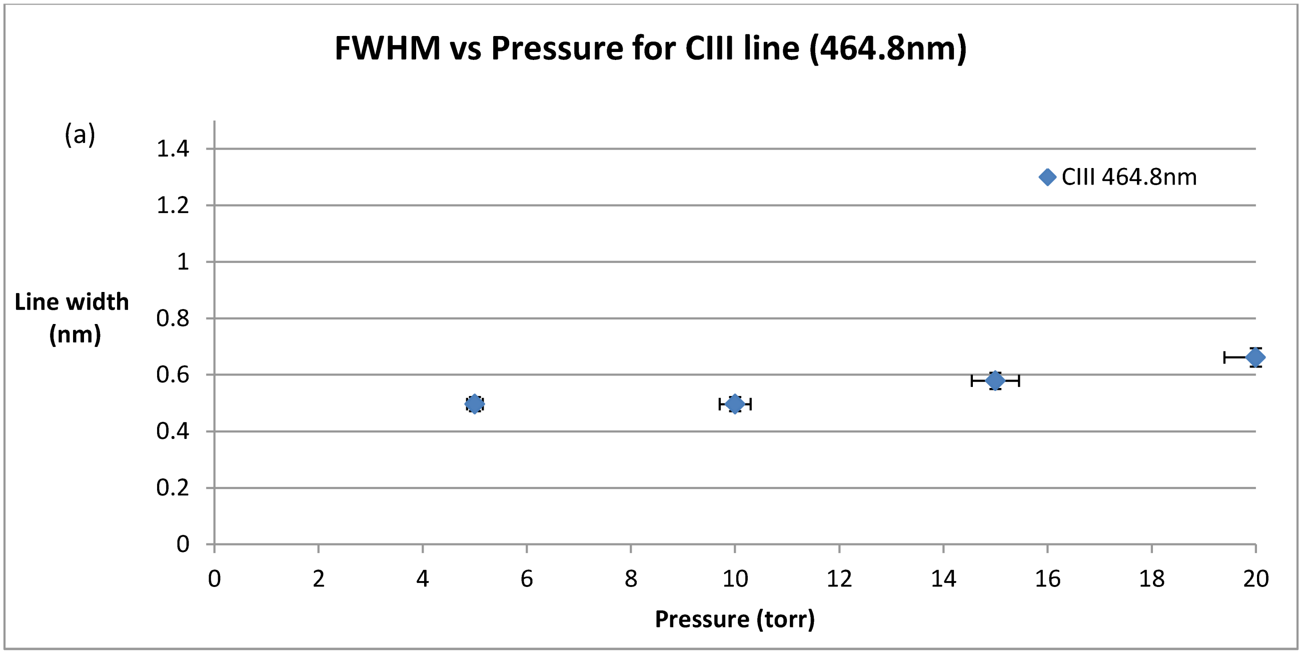

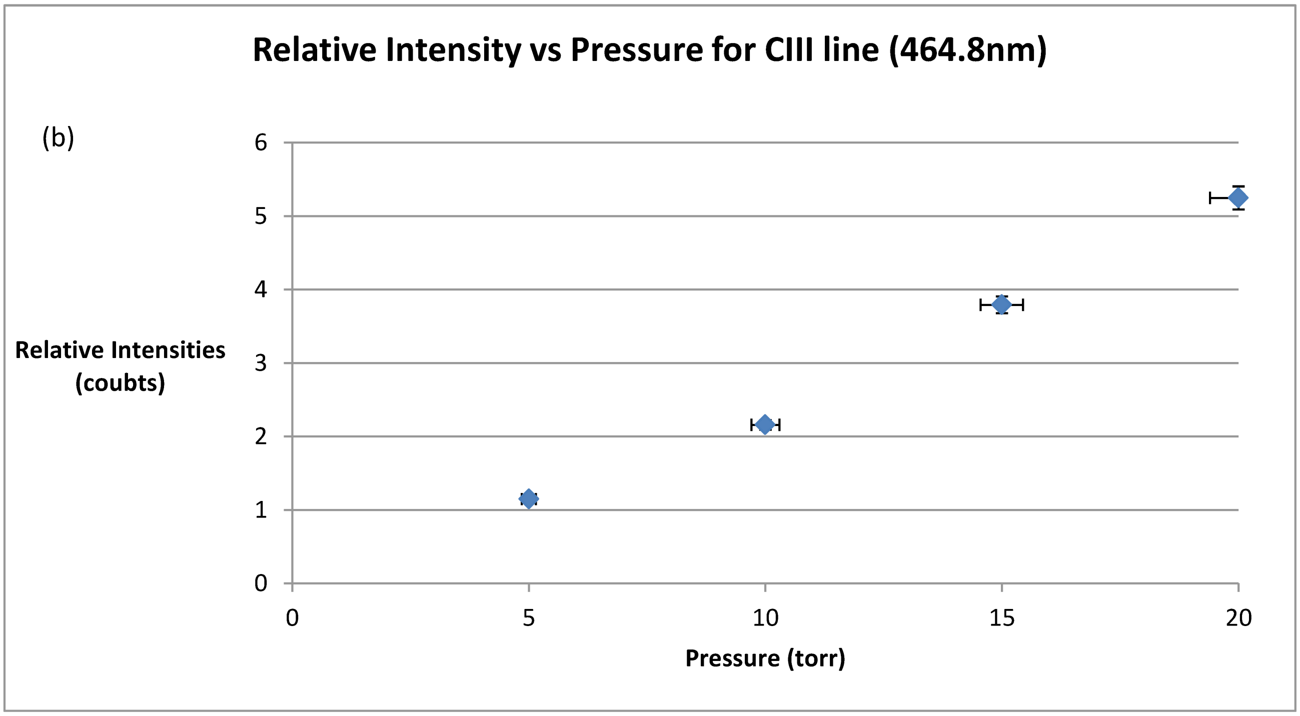

Fig 4.14: (a) Line width (FWHM) vs Pressure and (b) relative Intensity vs Pressure plot for CIII line

An example of the CII doublet line (657.8 nm and 658.3 nm) observed at 5 torr is shown in Fig 4.15.

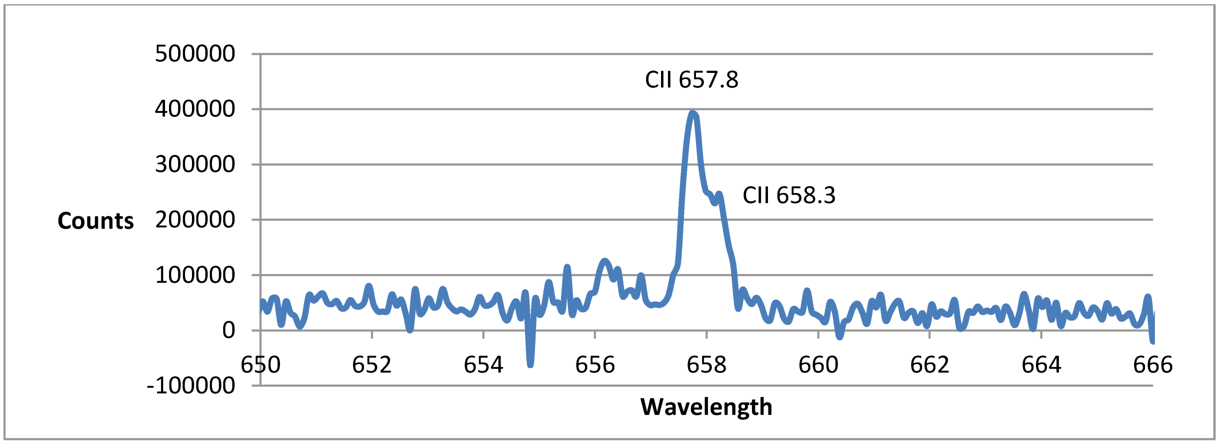

Fig 4.15: CII doublet at 657.8nm and at 658.3nm (accumulating 1000 acquisitions and pressure= 5 Torr)

An example of part of the spectrum taken at pressure of 5 torr for CO_2 gas is shown in Fig 4.16.

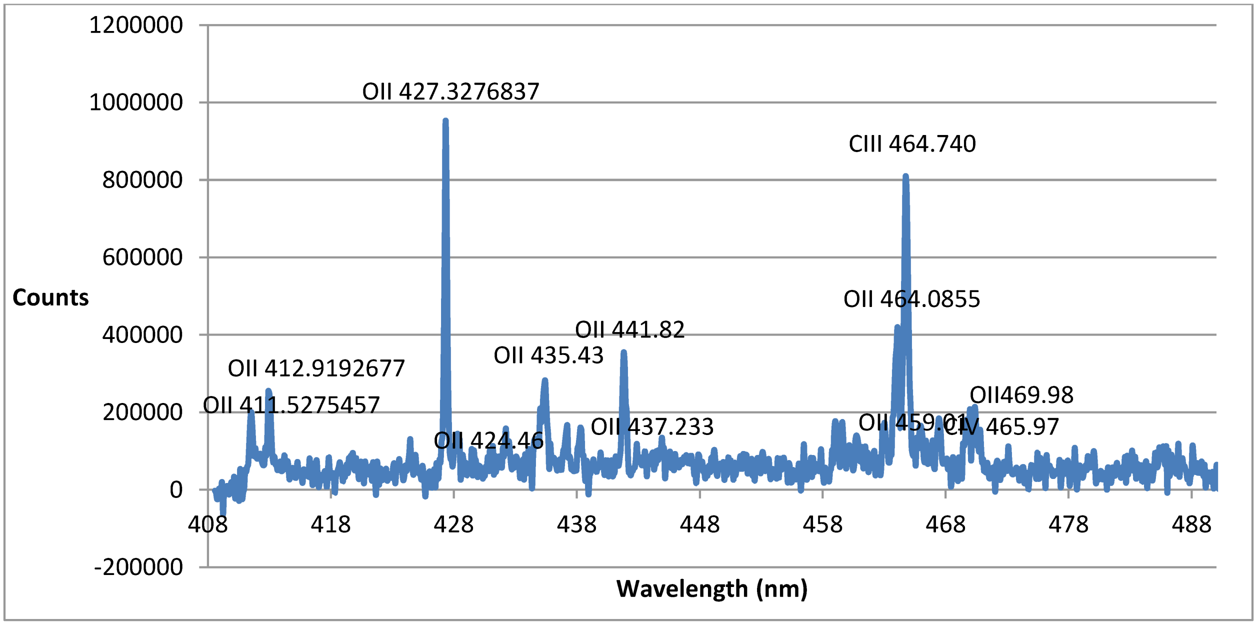

Fig 4.16: A section of the full spectrum at pressure, P=5torr

Table 4.1 shows a list of wavelengths observed by using the experimental plasma imaging setup (Fig 4.10). The same parameters were used as mentioned Fig 4.13 and Fig 4.14 at a pressure of 5 torr in order to observe these lines.

Table 4.1: List of wavelengths have been observed using the spectrometer

Ionic state	**Wavelength (nm)**
CIII	407.026

CII	407.585
CIII	464.742
CIII	465.025
CIV	465.830
CII	566.247
CII	588.977
CII	589.159
CII	657.805
CII	658.288
OII	409.652
OII	411.9215
OII	412.9321
OII	424.5519
OII	427.3104
OII	428.3249
OII	435.3594
OII	437.1618
OII	437.8427
OII	441.6974
OII	459.0972
OII	461.3681

OII	464.18104
OII	469.9220
OII	470.3163
OIII	559.237
OI	615.818

Data has been taken for Linear and circularly polarized light to see if any spectral broadening could be observed due to Zeeman Splitting from axial magnetic field generation. To generate circularly polarized light, a quarter waveplate was introduced in the beam path in front of the gas chamber. Fig 4.17 shows the experimental setup that has used to take the data for the circularly polarized beam. The laser energy was the same as for the linearly polarized beam (100 µJ) and the repetition rate was 1kHz.

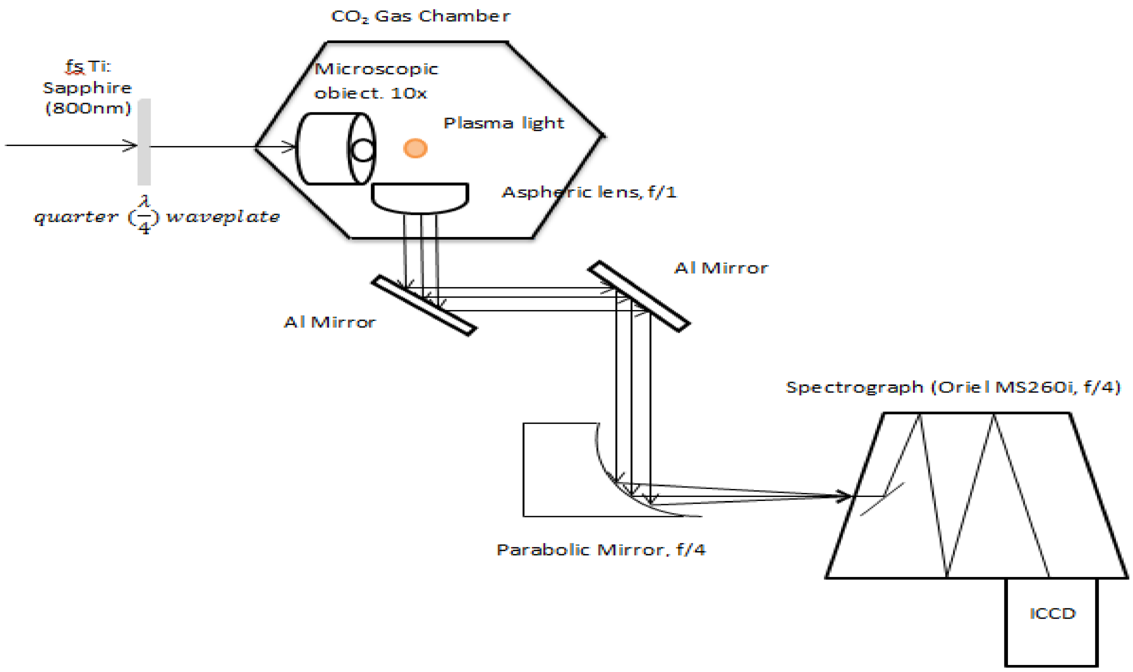

Fig 4.17: Schematic diagram of the experimental setup for measuring Zeeman splitting from propagation of femtosecond pulses in underdense plasma.

Fig 4.18 and Fig 4.19 showing data taken experimentally for 5 torr and 10torr pressure inside the gas chamber**.** The gate width was 200ns, gate pulse delay was 330ns and MCP gain was set to 150. 1000 accumulations were averaged together and camera exposure time was set to 0.1s for each accumulation.

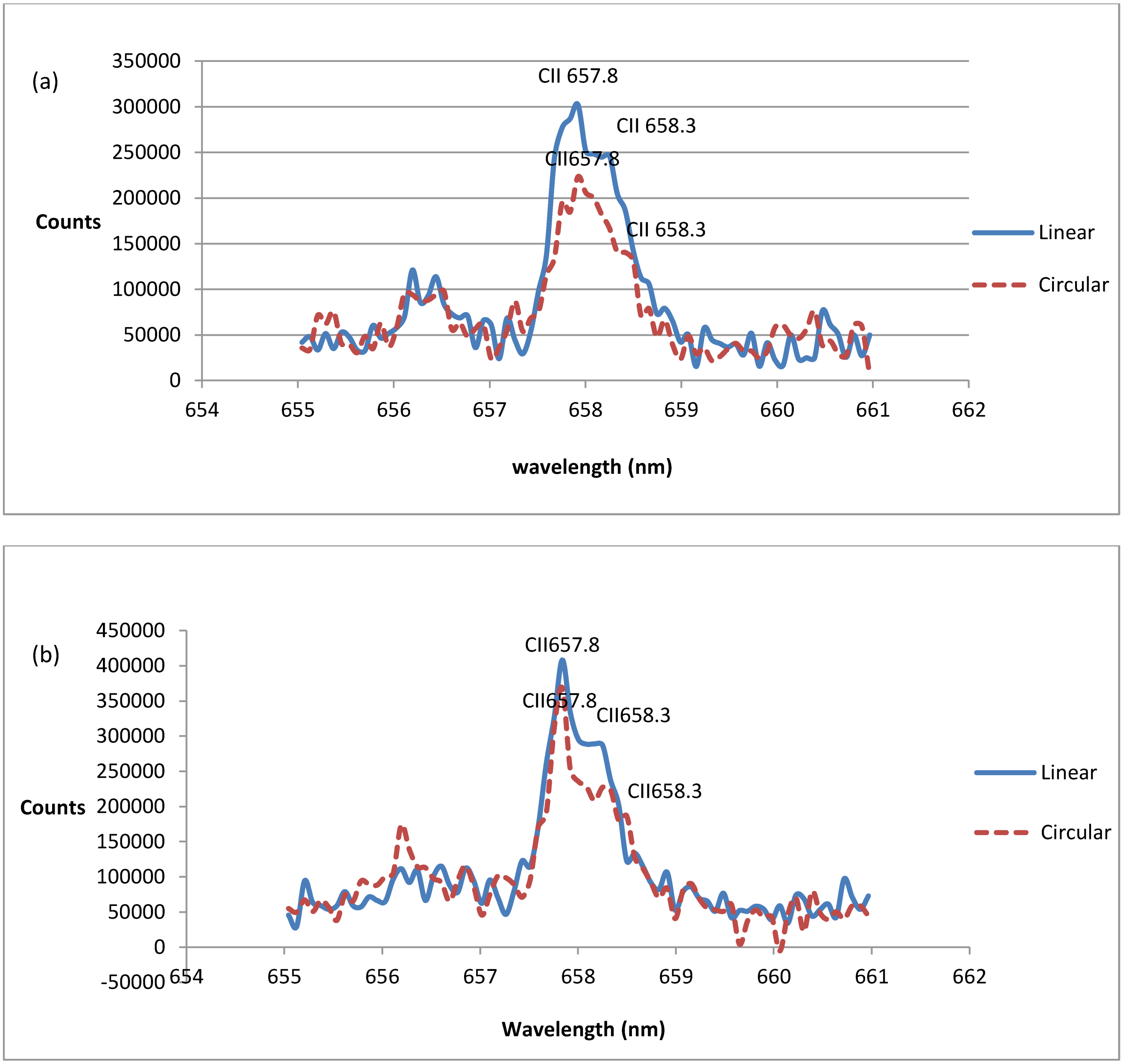

Fig 4.18: CII doublet lines at 657.8nm and 658.3nm for linearly polarized light (blue) and for circularly polarized light (red dashed) (a) at pressure of 5torr and (b) pressure of 10 torr

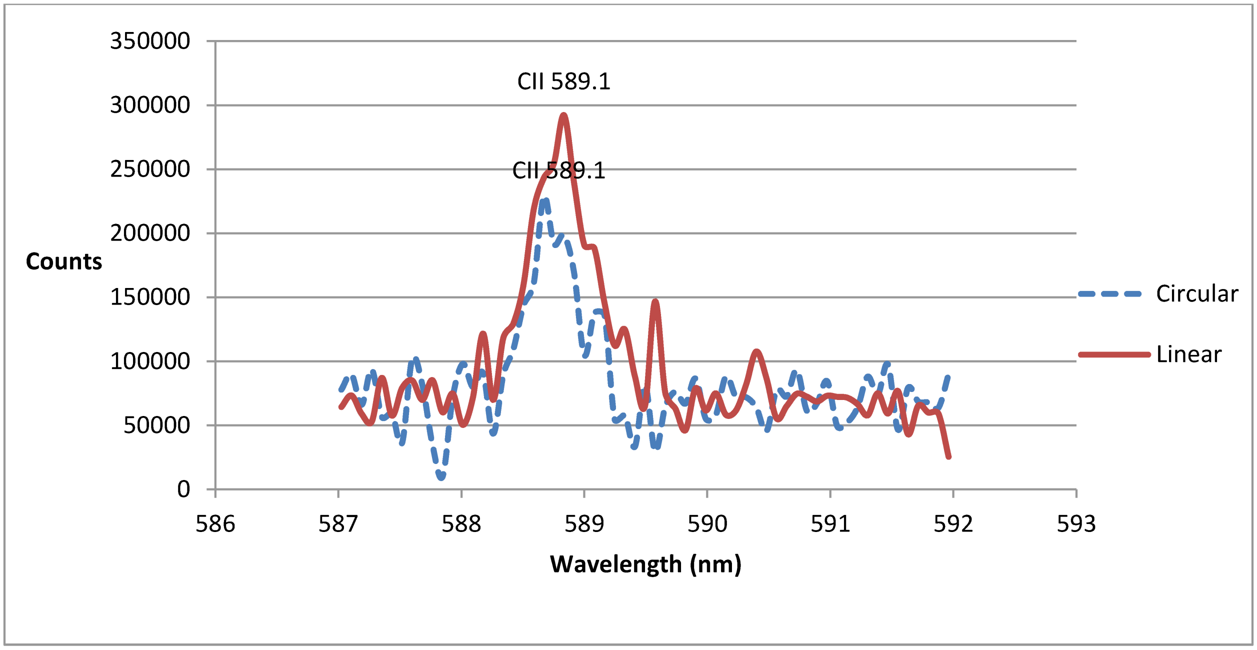

Fig 4.19: CII doublet lines at 589.1nm for linearly polarized light (red) and for circularly polarized light (blue dashed) at pressure of 10 torr

4.6 Discussion

As discussed before, from section 4.3, it can be seen that ionization volumes for ionization states of +1 and +2 are much larger than the volume of ionization stages of +4 and +5. From table 4.1, we can see that we observe the lower ionization states of +1 and +2 and do not observe higher ionization states at present. This is due to two reasons. Firstly, the signal to noise ratio for the observed lines is low and thus the much weaker emission from the smaller emission volumes of the higher ionization states will put these lines below the noise level. Also for the present measurements, to get clear spectra, the ICCD was gated on at a time of 40ns after plasma creation and thus the higher ionization states have probably started to recombine over this period.

The present measurements indicate that it is possible to observe the lines of interest from carbon to measure Zeeman splitting. The resolution of the spectrometer was set to 0.49nm in order to collect a large amount of emission light from the plasma due to the weak emission at low background pressures. Such low background pressures are required in order to reduce the Stark Broadening of the lines which can be estimated from the formula given by Griem [59] :

$$n_e = \frac{\Delta\lambda_{FWHM}}{2W} \times 10^{16}\ cm^{-3} \tag{4.14}$$

where, $\Delta\lambda$ is the line broadening shift due to stark Broadening, W is the electron-impact (half) half width and n_e is the plasma electron density.

We can re-arrange eqn (4.14) to give:

$$\Delta\lambda_{FWHM} = 2W\ \times \frac{n_e\,(cm^{-3})}{10^{16}} \tag{4.15}$$

Using a starting pressure of 5 torr, at room temperature, the plasma density for singly ionized CO_2 is $0.5 \times 10^{18}\ cm^{-3}$ and for a Pressure of 10 torr, the plasma electron density would be $1 \times 10^{18}\ cm^{-3}$.

For CII 6578 A^0 and 6582 A^0, W=2.41$\times 10^{-2}$ at a temperature of T_e= 7eV (largest temperature given) [59]. Thus for a pressure of 5 torr, one would expect $\Delta\lambda_{FWHM} = 2.4\ A^0$ and for a pressure of 10 Torr, $\Delta\lambda_{FWHM} = 4.82\ A^0$. These linewidths can be compared to the observed linewidths of $\sim 3A^0\ and\ \sim 5A^0$ from the results shown in Fig 4.13 (a) for these lines at pressures of 5 torr and 10 torr respectively. Note that to calculate these linewidths the doublet separation of $2.4A^0$ is convolved with the instrumental resolution of $4.9A^0$ to give an effective instrumental width of $7.3A^0$ which is deconvolved from the measurement values. Thus it is seen that there is good agreement between the expected and observed linewidths at these pressures.

The Zeeman splitting can be calculated using the equation used by Carolan [55]:

$$\Delta\lambda = 4.67 \times 10^{-9}\, \Delta(Mg) B\, \lambda^2\ (A^0, T) \tag{4.16}$$

where $\Delta(Mg)$ is the difference in the product of M and g between the lower and upper states of the transitions, where wavelength λ is in $A^0$and magnetic fields are in Tesla.

We can re-arrange 4.12 to give,

$$B(T) = \frac{\Delta\lambda}{4.67\times10^{-9}\, \Delta(Mg)\, \lambda^2}$$

For CII 658.2 nm line, the highest $\Delta(Mg)$ value possible is $\pm\frac{5}{3}$ [53] for the two lines in the doublet giving a total split peak to peak of $\frac{10}{3}$.

So, in order to observe Zeeman splitting of the order of 0.4nm, a magnetic field of B= 6 T would be required.

From the PIC simulation calculations shown in Fig 3.15, to generate an axial magnetic field of B=0.06MG requires an electron density of

$1 \times 10^{18} cm^{-3}$ for a laser pulse with a peak power of P=4.7 GW (in 1 μm^2 focal spot). Thus if we assume that Zeeman splitting 0.4nm would be a lower limit that could be measured then it appears we are below the power threshold to make such a measurement in the focal region where peak fields are produced. However at the peak of the laser the temperature of the plasma would be too hot to emit much line radiation and carry out effective line width and line shift measurements. Thus acutal measurements would have to be taken several nanoseconds after the plasma heating and magnetic fields will have spread out and decayed significantly by this time. Thus much stronger fields would be required initially to ensure that residual fields of 0.06MG or higher exist at the time of the measurement. To induce higher magnetic fields we need higher Intensity laser pulses.

Actual measurements can be done during the plasma heating too with a high intensity laser. To measure the CII lines, one can measure the line emissions away from the central axis of the main laser beam as lower ionization sates will be at the edge of the plasma. One can set the spectrograph to view the radial edges of the plasma and vary the gate delay to see the lower ionization lines during the plasma heating time. In this case the edge field of the magnetic field will be observed which will be lower than the field on axis but it can be calculated with the PIC simulation.

The other possibility is to improve the spectral resolution of the measurement allowing measurement of much smaller Zeeman splitting. However, a low pressure below $\sim 1\ torr$ would be required to reduce the emission line width to the order of 0.1 nm and then the magnetic filed generation would also be reduced at the same time leading to little advantage in using higher resolution spectrometer systems.

4.7 Conclusion

The main focus of this chapter was to explore the conditions required in order to use the Zeeman splitting effectively as a method to measure the induced magnetic fields due to the Inverse Faraday Effect. From 3D PIC simulations, it is seen that when using the low density plasma and low Intensity, the induced magnetic fields are fairly small on the order of 0.016MG to 0.7MG. Higher Magnetic fields can be obtained using higher laser Intensity and plasma density. The use of higher resolution spectrometer would not be very effective since the measurement of smaller Zeeman splitting shifts would also require the reduction in emission line width. Such narrow emission line widths would in turn require operation at pressures of 1 torr or less leading to much weaker emission signals and a concomitant reduction in the magnetic field generation for a given laser power.

From the results obtained it appears that the current laser power available is not adequate to observe the axial magnetic field generation and higher laser power is required. We are currently building a new TW laser system in our laboratory. When that is operational, hopefully we will be able to measure the Zeeman splitting due to Megagauss axial field generation in our laboratory. However, the issue of viewing the correct ionization state to see the desired line emission needs to be resolved in order for such a measurement to be carried out. one should examine the possibility of observing higher ionization state lines, perhaps in the UV part of the spectrum.

Chapter 5

Summary and Future Work

5.1 Introduction

The generation of self-induced magnetic fields in high intensity laser produced plasma is currently of theoretical and experimental interest because of its importance in the generation and application of high energy electrons and protons. The main objective of this thesis is to assess the generation of the self-induced magnetic fields due to the Inverse Faraday Effect and estimate the amount of magnetic field that can be generated using this process. In addition this thesis explores the possible application of the Zeeman Effect to measure these induced magnetic fields.

5.2 Summary of work

The generation of Self-induced axial magnetic fields due to the Inverse Faraday Effect has been examined. Analytic theories for the field generation were assessed and scaling laws versus intensity and plasma density were presented. We then carried out some 3D PIC numerical simulations to study the Inverse Faraday Effect for high intensity laser plasma interactions. The induced axial magnetic fields are generated as the laser interacts with plasma and generate hot electrons. We have found the induced magnetic fields strength is related to the Laser intensity and the hot electron density. We have carried out simulations at 3 different Intensities ($6.3 \times 10^{17}\, Wcm^{-2}\ to\ 6.3 \times 10^{19}\, Wcm^{-2}$) in a 3D grid using LSP modeling. The Induced magnetic fields were in the MG range. For an Intensity of $6.3 \times 10^{19}\, Wcm^{-2}$, induced magnetic fields up to 9MG were observed. The hot electron temperature follows a scaling law approximately proportional to square root of laser Intensity (T_{hot} (MeV)$\propto {I_{18}}^{\frac{1}{2}}$). The number of hot electrons produced from the laser plasma interactions is also depending on laser intensity. The current analysis only looked at the early stages of the magnetic field generation. From the results, it appears feasible to achieve MG fields with intensities of 10^{18} to$10^{19}\, Wcm^{-2}$. However with our current peak intensity of$\sim 10^{17}\ Wcm^{-2}$, it may only be possible to generate fields below 0.1MG.

Zeeman splitting has been examined as a prospective method to measure the induced magnetic fields. The assessment indicated that it should be possible to measure fields of the order of 0.1MG or higher with higher intensity laser beams using Zeeman splitting.

A Preliminary set of measurements have carried of emission lines from focusing into static gas targets. A Ti:Sapphire laser operating at an output of 1GW with 1kHz repetition rate was used for this study. CO_2 gas was used as the main interaction gas and data has been taken at various pressures to measure the line width. Most of the emission lines are the lower ionization lines. The emission lines of CII at 657.8nm and CII at 658.3nm were measured for the linearly and circularly polarized laser pulses. As IFE is associated with circularly polarized light, an axial magnetic field should be induced for circularly polarized light. However the magnetic fields induced were too weak at the available laser power, so that an increase in linewidth due to Zeeman splitting wasn’t observed with the existing setup. It appears that there is little advantage going to lower pressures to reduce the Stark broadening of the lines since the induced magnetic fields and resultant Zeeman splitting will decrease also.

5.4 Future Works

The work presented here is the beginning of the story. All the data taken and simulations done are preliminary investigations towards measuring Megagauss fields at higher laser powers. Further work is required to measure and understand the real generation of such magnetic fields.

In order to reduce the growth of numerical instabilities with time in the simulations, much finer grids should be used. This would require more processors and run time.

Another possible interesting future development would be to introduce orbital angular momentum (OAM) modes and see the dependency of axial magnetic fields on them. One can use Laguerre Gaussian (LG) beams and induce higher Magnetic fields with higher order of LG modes [11]. Recently it has been predicted that linearly polarized light can also be used to induce axial magnetic fields using LG beams as they have helical wave fronts and orbital angular momentum, which can drive the electrons to produce magnetic fields. This is an interesting area to explore in the future.

Experimentally, more work can be done to optimize the collection of emission signals and vary the timing of observation of emission over the first few nanoseconds. The high repetition rate available of 1 kHz would allow for integration of millions of shots to improve the signal to noise ratio.

In the future the current studies will be extended to a higher energy laser. It is expected that with intensities of $10^{18}\ to\ 10^{19}\ Wcm^{-2}$, it should be possible to generate Megagauss fields which could readily be measured via Zeeman splitting. Another possible future investigation would be to generate an external magnetic field of several Tesla that can be place inside the interaction chamber. The external B fields can be used for calibration purposes and to add to the induced magnetic fields causing larger Zeeman splitting that could then be measured using a higher resolution spectrometer.

References:

[1] T. H. Maiman, Stimulated Optical Radiation in Ruby. Nature, 187:493, 1960

[2] Paul Gibbon, Short Pulse Laser Interactions with Matter, Imperial College Press, London, (2005), pg-2.

[3] M. Tabak, et al., Physics of Plasmas, 1:1626, 1994

[4] T. Tajima and J. M. Dawson. Laser Electron Accelerator. Phy. Rev. Lett, 4:267, (1979).

[5] P. V. Nickles, et al., Phys. Rev. Lett, 78:2748, (1997).

[6] Z. M. Sheng and J. Meyer-ter-Vehn, Phys. Rev. E 54, 1833 (1996)

[7] J. A. Stamper *et al.*, Phys. Rev. Lett. 26, 1012 (1971)

[8] S. C. Wilks, W. L. Kruer, M. Tabak and A. B. Langdon, , Phys. Rev. Lett. 69, 1383 (1992)

[9] M. G. Haines, Phys. Rev. Lett. 87, 135005 (2001)

[10] R. J. Mason and M. Tabak, Phys. Rev. Lett. 80, 524 (1997)

[11] S. Ali, J. R. Davies and J. T. Mendonca, Phys. Rev. Lett. 105, 035001 (2010)

[12] Claire Ellen Max, *et al.* Phys. Fluids 21(1), 128 (1977)

[13] R. J. Mason and M. Tabak, Phys. Rev. Lett. 80, 524 (1997)

[14] *Faraday's Diary. Volume IV, Nov. 12, 1839 - June 26, 1847 (Thomas Martin Ed.)*

[15] Shalom Eliezer, The interaction of high power lasers with plasmas, IOP Publishing Ltd. 2002, Bristol and Phildelphia,(pg-14, 17, 24, 44, 88).

[16] *A Raven and O Willi,* Phys. Rev. Lett. 41, 554 (1978).

[17] D. E. Spence et al. Optics Lett. 16, 42 (1991)

[18] Donna Strickland, and Gerard Mourou, Optics Comm. 56, 219 (1985).

[19] W.L. Kruer, *The physics of laser plasma interactions*, Allan M. Wylde, California (1988)

[20] L. Schlessinger and J. Wright, *Phys. Rev. A*, 20:1934–1945, 1979

[21] M Chaker, et al. Phys. Fluids B 3, 167 (1991)

[22] J. C. Kieffer, et al. Phys. Rev. Lett, 62:760, 1989

[23] D. W. Forslund, et al. Phys. Rev. Lett 39, 284 (1977)

[24] K. G. Estrabrook, et al. Phys. Fluids 18, 1151 (1975)

[25] J P Freidberg et al Phys Rev Lett. 28:795, (1972)

[26] S. C Wilks and W. L. Kruer, *IEEE Journal of Quantum Electronics* 33:11, 1997, 14, 19

[27] F. Brunel, Phys. Rev. Lett, 59:52, 1987. 21

[28] P. Gibbon and A. R. Bell. Collisionless absorption in sharp-edged plasmas. Phys. Rev. Lett., 68:1535, 1992.

[29] Mourou, Tajima and Bulanov, Rev. Mod Phys., vol 78, No. 2, (2006)

[30] Ernst E. Fill, Optical Society of America B, vol 11, 2241 (1994)

[31] R. Fedosejevs et al, Physical Review E. vol 56, 4615 (1997)

[32] F N Beg et al., Phys. Plasmas 4 (2), (1997)

[33] S. C. Wilks et al , Phys. Rev. Lett. 69 (9) (1992)

[34] M. G. Haines et al., Phys Rev. Lett 102,045008 (2009)

[35] T Lehner, Physica Scripta, Vol 49, 704-711 (1994)

[36] Y. Horovitz, *et al.,* Phys. Rev. Lett.78, 1707 (1997)

[37] Z. Najmudin *et al.,* Phys. Rev. Lett. 87,215004 (2001)

[38] N. Nesari et al,. Phys. Of Plasmas 17, 083109 (2010)

[39] Richard A. Beth, *et al.,* Phys. Rev. Lett. 50, 115 (1936)

[40] L. Allen, *et al,* Phys. Rev. A 45, 8185 (1992)

[41] M. G. Haines, Phys. Rev. Lett. 87, 135005 (2001)

[42] *S. Ali, et al., 37th EPS Conference on Plasma Physics, P5.211 (2010)*

[43] David W. Walker, Concurrency: Practice and Experience, Vol 2(4), 257 (1990)

[44] John M. Dawson, Reviews of modern Phys. 55, 403 (1983)

[45] R. E. Clark and T. P. Hughes, LSP user's manual and references for LSP version 8.7 (2005)

[46] V. Malka et al, Physics of Plasma 8, 2605 (2001)

[47] M. I. K. Santala, et al., Phys. Rev. Lett. Vol 86, 1227 (2001)

[48] Gahn et al, phys of Plsmas vol 9, 987 (2002)

[49] R.S Bird, et al, Phys. Rev. A 7, 1328 (1973)

[50] E.A McLean, et al, Phys. Fluids 27(5), 1327 (1984)

[51] J Braind, et al, Phys. Fluids 30 (9), 2893 (1987)

[52] P. Ewart, Atomic Physics, University of Oxford 2008, Ch4

[53] F. C. Jahoda, et al, Phys Rev. Lett. 131, 24(1963)

[54] N. J. Peacock et al. Physical Review A 11 (6), 2142, (1974)

[55] P. G. Carolan, N. J. Peacock et al. Plasma Phys. and controlled fusion, vol 27, 1101(1985)

[56] J. Gafert et al., 28th EPS con. On Contr. Fusion and Plasma Phys Funchal (2001)

[57] K. Krieger et al., 34th EPS con on Plasma Phys (2007)

[58] Craig J. Sansonetti et al. Applied optics, vol 35 (1),74 (1996)

[59] Hans R. Griem, Plasma Spectroscopy, 1964, 454, 460, 465